GEO -3900

Master's thesis in Geology

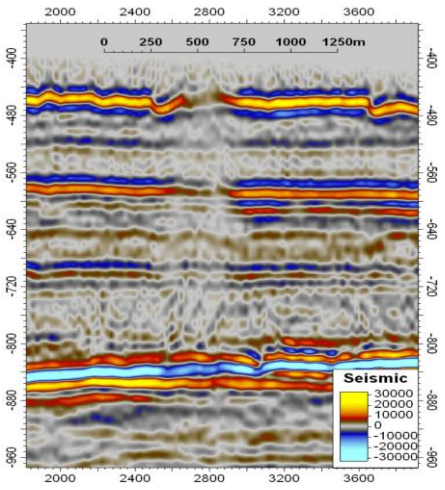

Morphological expressions of recent and past fluid flow expulsions of the SW Barents Sea

Daria Namyatova

May, 2011

Faculty of Science

Department of Geology

University of Tromsø

GEO -3900

Master's thesis in Geology

Morphological expressions of recent and past fluid flow expulsions of the SW Barents Sea

Daria Namyatova

May, 2011

Morphological expressions of recent and past fluid flow expulsions of the SW Barents Sea

Daria Namyatova

The Faculty of Science-Department of Geology-University of Tromsø, Dramsveien 201, 9037 Tromsø

ABSTRACT

Three 3D seismic cubes (EL0001, St0309 and ST05M09) from different parts of the SW Barents Sea basin were studied to decipher processes causing depressions in the seabed and subseabed. Since the investigated areas were under the influence of various depositional and erosional conditions during ice ages special attention was given to the potential of ice driven morphologies. Depressions identified at the seafloor and at the upper regional unconformity (URU) sub surface vary in shape, size and depth. Their distribution is governed by large scale glacial morphology and deeper fluid accumulation and migration pathways as inferred from seismic anomalies. The formation of fluid flow related depressions could be a result or a combination of both external (glacial erosion and accumulation) and internal factors (gas expansion). Evidence for fluid flow exists in deeper layers and thus fluids could migrate upward along faults and porous sediment strata and spread laterally in upper sediment layers. A second class of depressions exists that is mainly related to glacier driven surface processes in for example subglacial melt-water channels without any obvious relation to deeper fluid sources. Generally, glacial morphological elements influence sediment facies distributions, the thickness of the deposits and therefore the location and frequency of pockmarks and/or pockmark fields. The pockmarks tend to occur inside iceberg-plough marks, mega scale glacial liniations (MSGL), all regions with reduced sediment thickness through which fluids may penetrate more easily. The timing of pockmark creation varies depending on fluid source areas, the thickness of the glacial sediment blanket and ice sheet retreat.

TABLE OF CONTESTS

1. INTRODUCTION

1.1. Objectives

This thesis contributes to identify the origin and distribution of fluid escape features such as chimneys and/or pockmarks in the SW Barents Sea in order to improve our understanding of their development in time and space. One part of the study is based on pockmark mapping using 2D and 3D seismic data to delineate the differences between potentially active and inactive pockmarks. Another part of this study concentrates on fluid and gas migration from deeper formations and their connection to shallow gas and pockmarks locations.

1.2. Study area

1.2.1. Geographical position

The Barents Sea is located at the western part of the < 400 m deep Eurasian Arctic shelf. The 3D seismic cubes used for the master thesis are situated in the south-western part of Barents Sea, south of Bjørnrenna (Fig. 1-1) and they are officially named ST0309 (Nordkappbanken), EL0001 (Veslemøy high), and ST05M09 (Ingøydjupet and Tromsflakket).

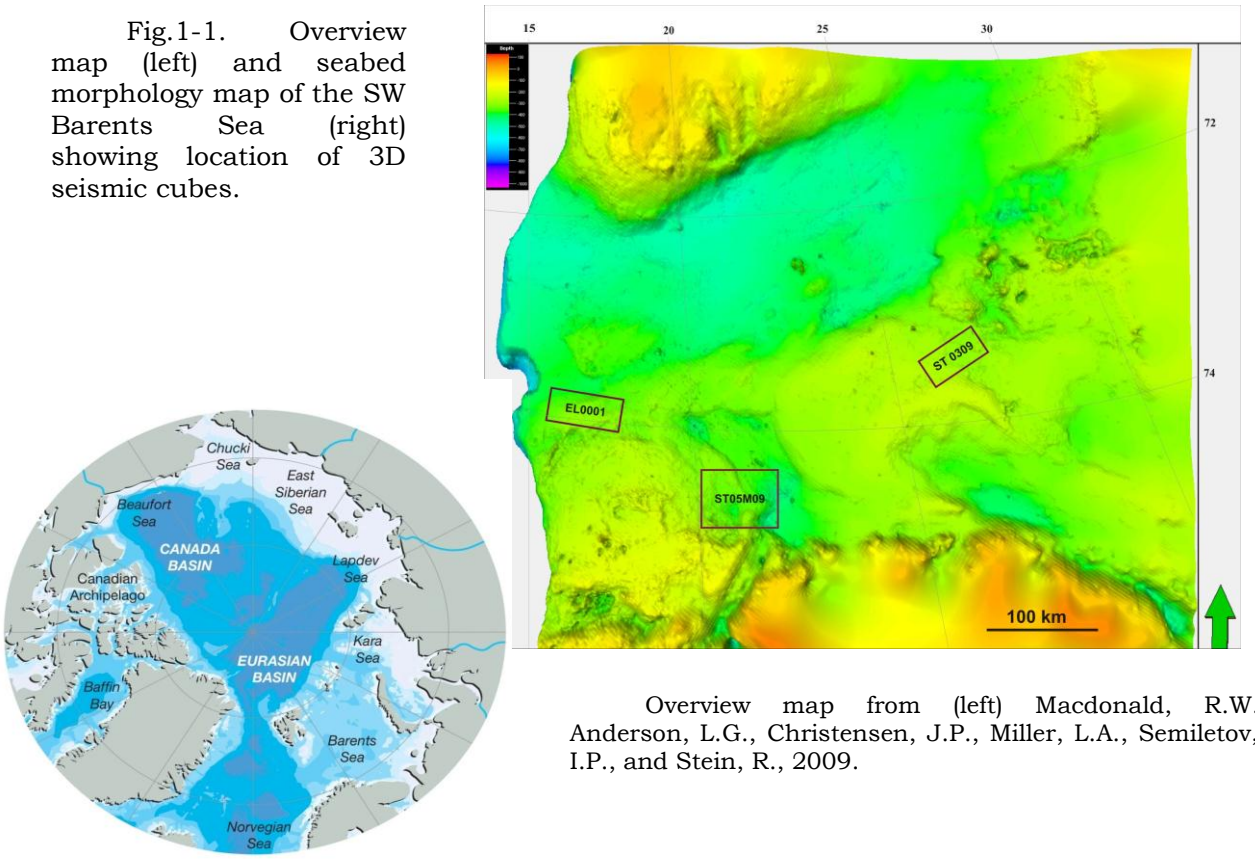

Fig.1-1. Overview map (left) and seabed morphology map of the SW Barents Sea (right) showing location of 3D seismic cubes.

Overview map from (left) Macdonald, R.W. Anderson, L.G., Christensen, J.P., Miller, L.A., Semiletov, I.P., and Stein, R., 2009.

1.2.2. Geological settings

The Barents Sea comprises a large epicontinental sea bounded by young passive continental margin in the north and west *(Faleide et al, 1984)*. The Barents Sea reveals complex geological provinces of basins and platforms *(Dore, 1995)*. The south-western part of the Barents Sea is subdivided into the three regional geological provinces:

- east-west trending basin province at the east between 74^{0}N and the coast of Norway;
- elevated platform area at the west towards the north including Svalbard;
- western continental margin area *(Faleide et al, 1984)*.

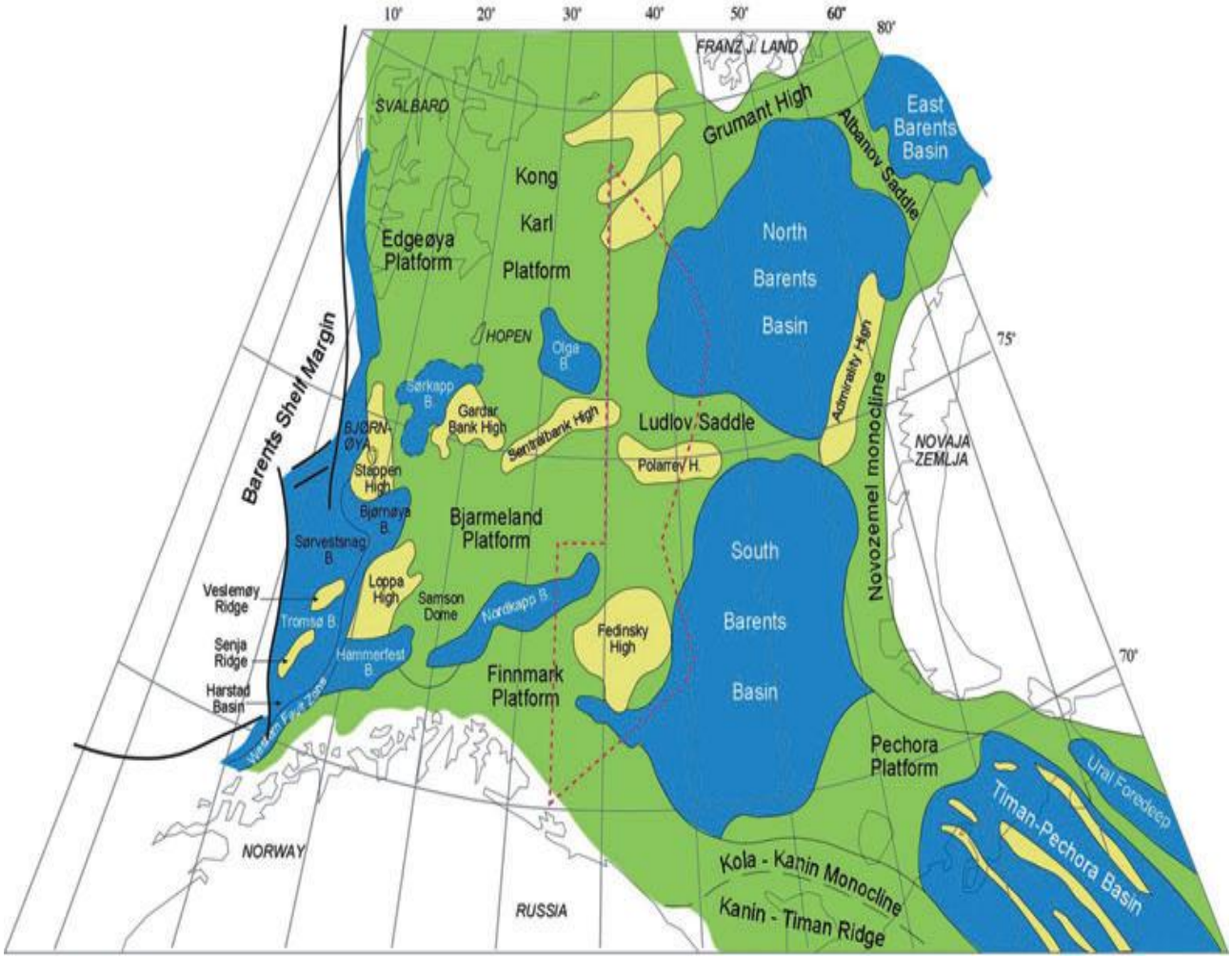

Fig. 1-2. Major structure elements of the Barents Sea *(Worsley, 2008)*.

The Norwegian sector of the Barents-Sea shelf consists of the following structural features: Nordkapp basin, Bjarmeland and Finnmark platforms, Hammerfest basin, Loppa High, Stappen High, Olga basin, Maud basin, Gardabanken High, Veslemøy high *(fig. 1-2) (Dore, 1995)*.

1.2.3. Tectonic development of the south-western part of the Barents Sea

The evolution of the western Barents Sea as a passive continental margin is closely linked to the gradual northward opening of the Norwegian Greenland Sea *(Faleide et.al., 1996)*. The area has gone through several phases of crustal extension and basin formation. Several phases of tectonic events since the Devonian, eventually developed into crustal break-up and sea floor spreading in the North Atlantic rift. At least five phases of basin development are widely recognizable throughout the area *(Ryseth et al, 2003)*:

1. Late Devonian – middle Carboniferous rifting;
2. Late Carboniferous – Permian carbonate platform development;
3. Triassic – Cretaceous siliclastic shelf development;
4. Early Cenozoic crustal break-up;
5. Late Cenozoic passive margin developments *(Nøttvedt et al., 1992)*.

Paleozoic basin evolution. From the beginning of the Late Devonian the evolution of the Svalbard-Barents Sea was dominated by regional crustal extensions *(Bukovics and Ziegler, 1984)*.

Late Carboniferous – Permian carbonate platform development. During the Late Carboniferous the clastics and carbonate sediments accumulated in the half-grabens that are bounded by presumably listric faults and basement involving normal faults *(Bukovics and Ziegler, 1984)*.

Crustal extension persisted into Late Permian times and led to the transgression of the Arctic Permian seas which advanced via the Norwegian – Greenland Sea Rift into the intra-cratonic Northern and Southern Permian basins of Northwest Europe *(Bukovics and Ziegler, 1984 and Ziegler, 1982)*.

Triassic-Cretaceous siliclastic shelf development. At the latest Permian-Early Triassic a transgression occurred along the Norwegian basin. During those times sediment accumulation was accompanied by syndepositional tensional faulting. The Late Triassic was characterized also by transgressions. Evidence exists of two major

halite layers indicating high evaporation rates in isolated basins. The area was affected by typical horst and graben structures *(Bukovics and Ziegler, 1984)*.

The Late Mesozoic rifting stage was followed by series of uplifting and dooming activities. The rifting activity concentrated in the East-Greenland – Mid- Norway basin *(Bukovics and Ziegler, 1984)*.

Paleocene-Eocene rifting. During the Paleocene-Eocene, a large regional strike – slip fault zone *(Faleide et al., 2008)* was activated; it stretched along the entire western margin of the Barents Sea from the south towards the north up to the incipient Arctic Ocean *(Golynchik, 2008)*. At that time, continental crust breakup occurred on the Norwegian margin, in the Labrador Sea, and in Baffin Bay, with occurrence of active spreading branches *(Golynchik, 2008)*.

In the Paleocene-Eocene transition the Cenozoic sea floor spreading in the Norwegian-Greenland Sea and Eurasian Basin began. It started at approximately 53 Ma (chron 24B/25). During the Eocene the initial opening started in the Lofoten basin (55-38 Ma) (west to the Senja Fracture Zone) and southern part of the Greenland Sea (52 Ma) (*Faleide et.al., 1996)*.

The passive margin development. The final breakup of the continent with formation of passive continental margins and spreading axis and Knipovich oceanic ridge occurred at the end of Eocene – beginning of Oligocene *(Golynchik, 2008)*.

The opening direction of the Norwegian-Greenland Sea spreading gave rise to further extension and the opening of the northern Greenland Sea (*Faleide et.al., 1996)*.

1.2.4. Glacial history of the Barents Sea

The Barents Sea stratigraphy shows several sediment packages that are divided by unconformities. Unconformities mark a lack of deposition and/or the existence of several erosion-dominated periods. The erosional unconformities occurred as a result of grounding ice-sheet advances *(Svendsen et al, 2004)*.

Accordingly, three major glacial events are defined within the Barents shelf (*Ryseth et al, 2003; Andreassen et al, 2007; Faleide et al, 1984)*:

- Initial: 2,7 – 1,5 Ma;
- Transitional: 1,5 - <0,7 Ma;
- Major phases *100kyr cycles: < 0,7 Ma.

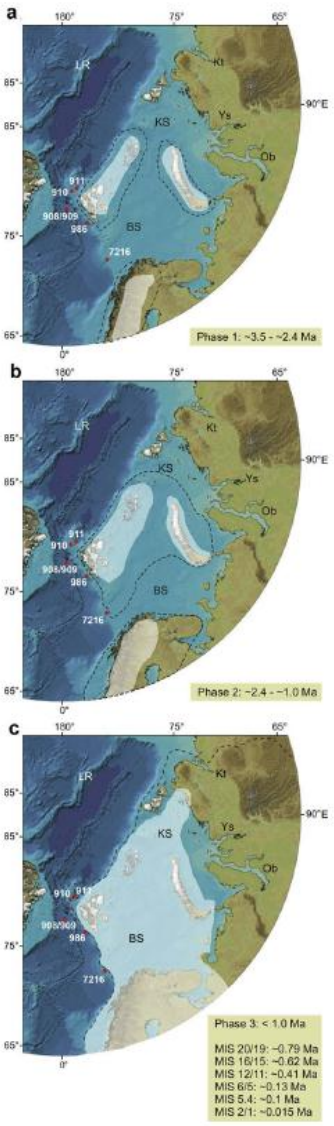

Fig. 1-3. New model of the Barents Sea glaciation *(modified from Knies et al, 2009)*

Increased glacial activity on the shelf correlates with increased amounts of IRD and major oxygen-isotope excursions in the open ocean (Spielhagen et al, 2003).

Major ice sheet expansion phases culminated in an ice-covered Barents Sea and Fennoscandia *(Laberg and Vorren, 1996)*. At the Late Weichselian maximum drainage was dominated by the Byørnøyrenna Ice Stream fed by large ice-source areas to the north-east and south. Two main southerly branches of the ice stream were operating: one in Ingløydjupet and one in the area of Nordkappbanken *(Winsborrow et al, 2010)*.

The deglaciation began with a significant retreat of the ice margin in the southern Barents Sea It marked a significant change in the dynamics of the ice sheet. The centre of maximum ice volume shifted eastwards, and much of the south-western Barents Sea became ice-free. The eastward shift were indicated by major readvance of the Djuprenna and Nordkappbanken-east ice streams, which were fed by ice flowing north across the Kola Peninsula, and north-east across Kandalaksha Gulf and the eastern tip of Kola Peninsula *(Winsborrow et al, 2010)*.

Finally, the complete loss of ice cover in the southern Barents Sea took place and the remaining ice margin was located in the outer-fjord area in northern Norway. The ice margin continued to retreat southward based on the well-mapped Tromsø–Lyngen and main substage moraines *(Andersen et al., 1995)*.

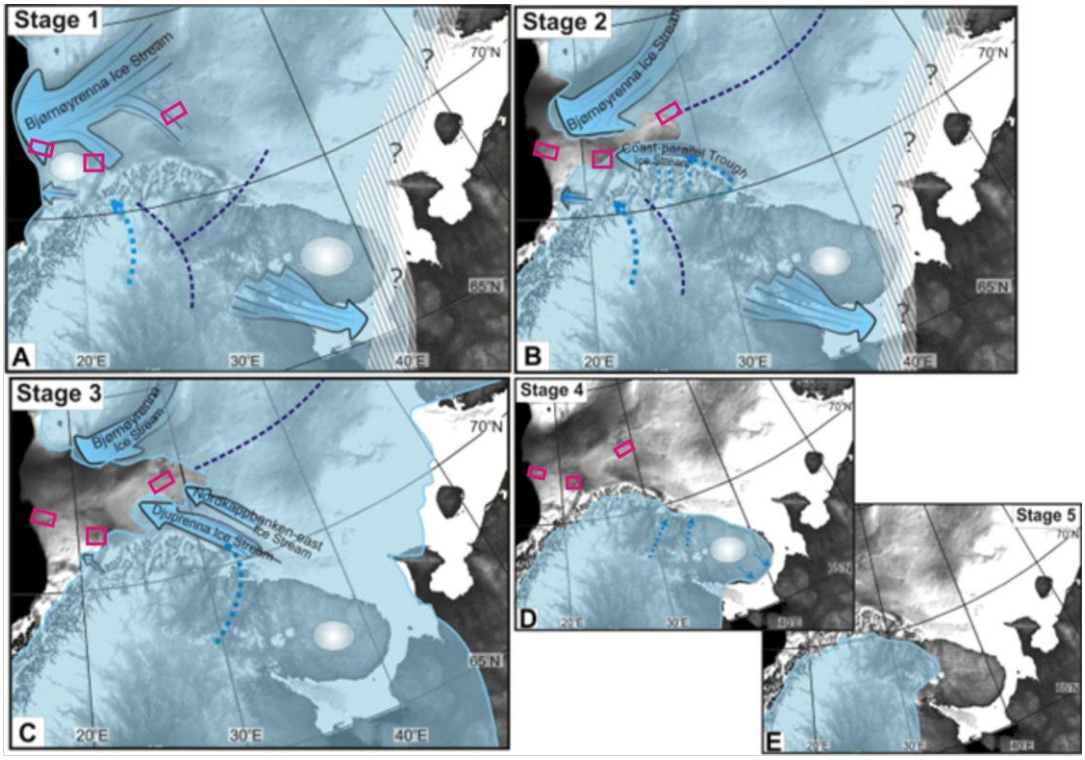

Fig. 1-4. Five stage reconstruction of the Weichselian maximum and subsequent deglaciation of the southern Barents sea *(Winsborrow et al, 2010)*; the red squares shows the location of 3D cubes.

1.3. Seismic stratigraphy

The stratigraphic units within the 3D seismic cubes are mainly subdivided into non-glacial sediments (Paleocene-Miocene and older) and glacial sediments (Plio-Pleistocene) (fig. 1-5).

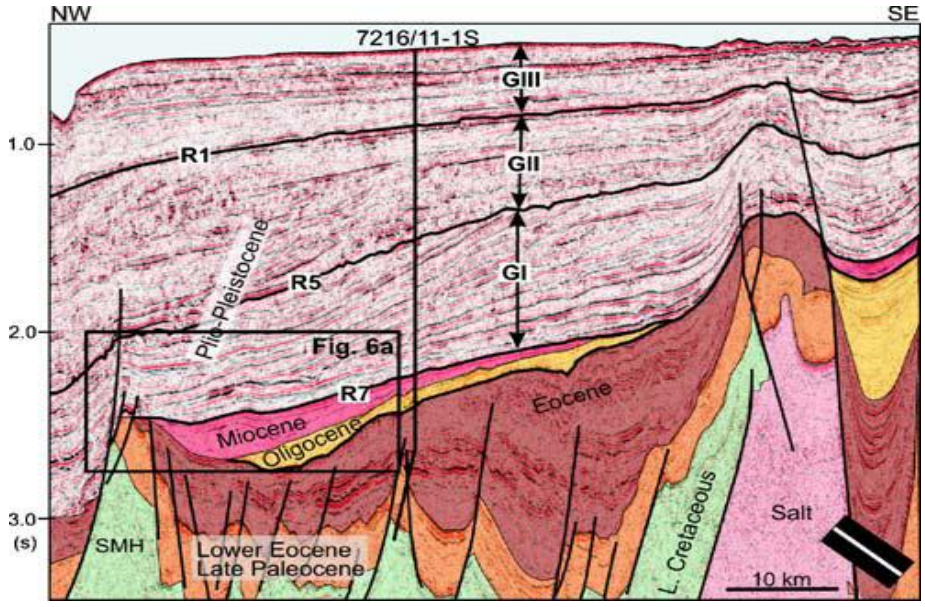

Fig. 1-5. Interpreted seismic profile from a 3D seismic cube. GI–GIII indicate main regional sedimentary sequences devided by R1, R5 and R7, i.e. main regional reflectors of the Plio-Pleistocene sedimentary successions. Pre-Pliocene stratigraphy is from Ryseth et al. (2003) *(Andreassen, et al, 2007a)*.

The non-glacial sediments, i.e. the Mesozoic rocks are the primary source for hydrocarbons *(Dore, 1995) (fig. 1-6)*.

The glacial sediments start above R7 and are clearly defined in the seismic sequences on the continental slope (e.g. Andreassen et al., 2007). Plio-Pleistocene sequences contain three main sediment packages (GI, GII and GIII) separated by the three main reflectors (R1, R5, R7) that relate to a major unconformity on the shelf (*Andreassen et al, 2007a)*. The base of glacial sediments on the shelf is the upper regional unconformity (URU) *(e.g. Rafaelsen et al., 2002, Chand et al, 2010)*.

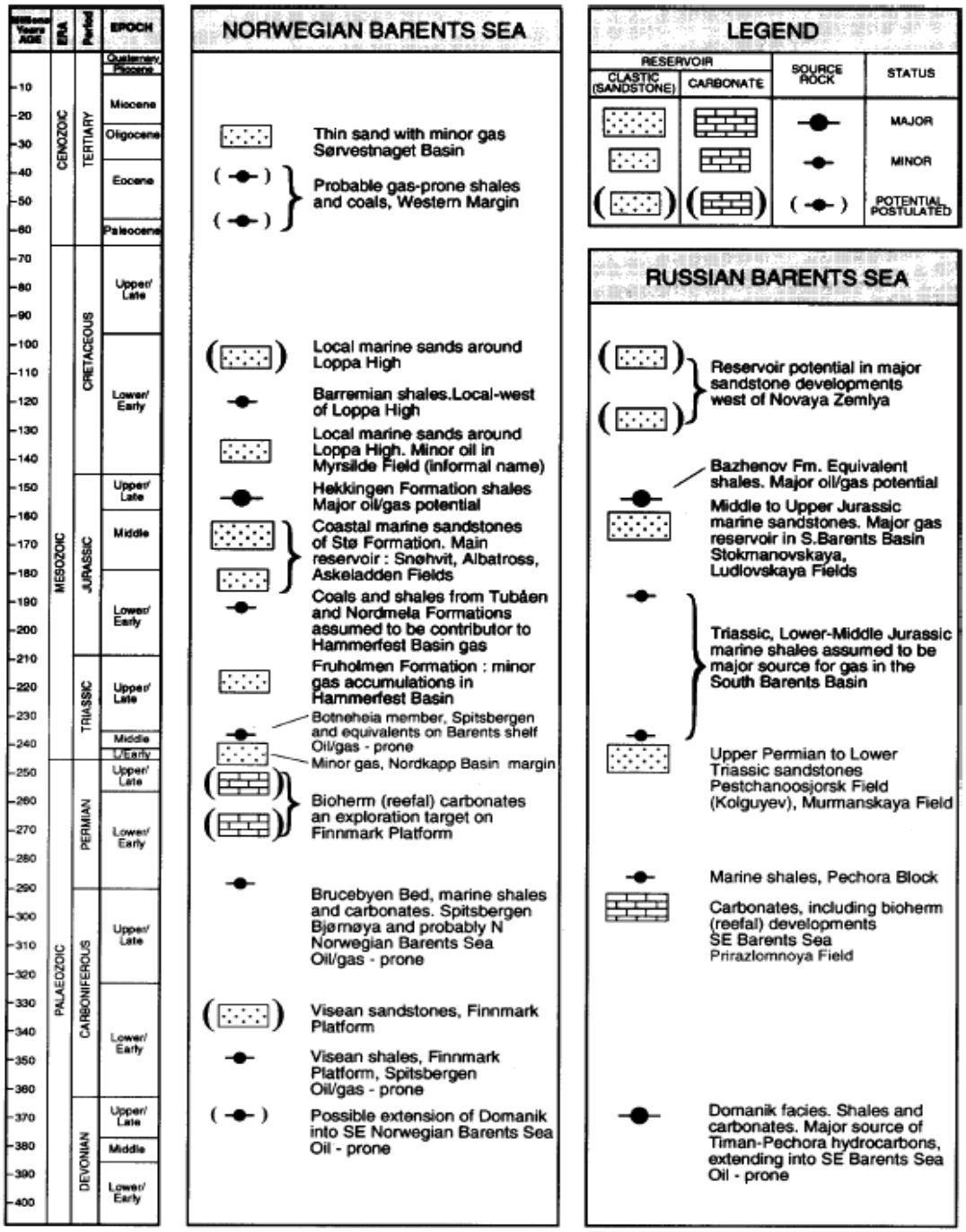

Fig. 1-6. Stratigrathic units along the Barents Sea (in relation to oil and gas potential) *(Dore, 1995)*.

The URU is a time-trangressive horizon with an estimated but still disputed age of 0,8Ma (e.g Rafaelsen et al., 2002). On the continental slope the main regional reflectors separating GI to GIII show an estimated age of approximately 2.5-2.3 Ma (R7), 1.5-1.3 Ma (R5) and 440-200 ka (R1). Recent results from 3D seismic investigations document that GII and GIII paleo-shelf units consists mainly of sediments from grounded glaciers *(Andreassen et al.2007)*.

Mega-scale glacial liniations of different orientations indicate several events of ice stream movements during the last ice age *(Winsborrow, 2009; Andreassen, 2007a, 2004; Ottesen 1995)* (fig. 1-7). The 3D seismic cubes are located in three different ice-stream influenced areas.

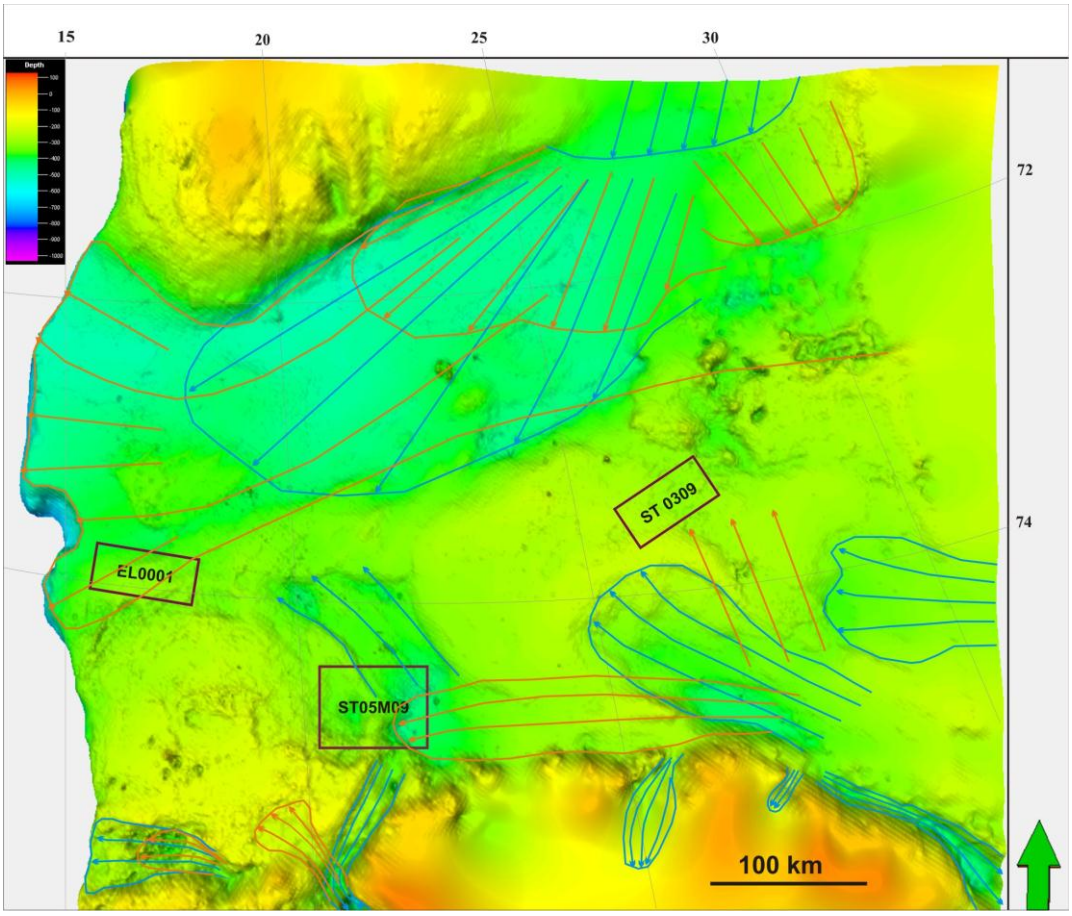

Fig. 1-7. Mega-scale glacial leniations and orientation from Winsborrow et al., 2010 and location of the three investigated 3D seismic cubes.

1.3.1. Nordkappbanken (ST0309)

The following seismic units exists within ST0309 from bottom to top: dome structures related to salt diapirs and sediments that are compressed because of salt diapirs uprising, non-glacial sediments, glacial sediments and upper regional unconformity (fig. 1-8).

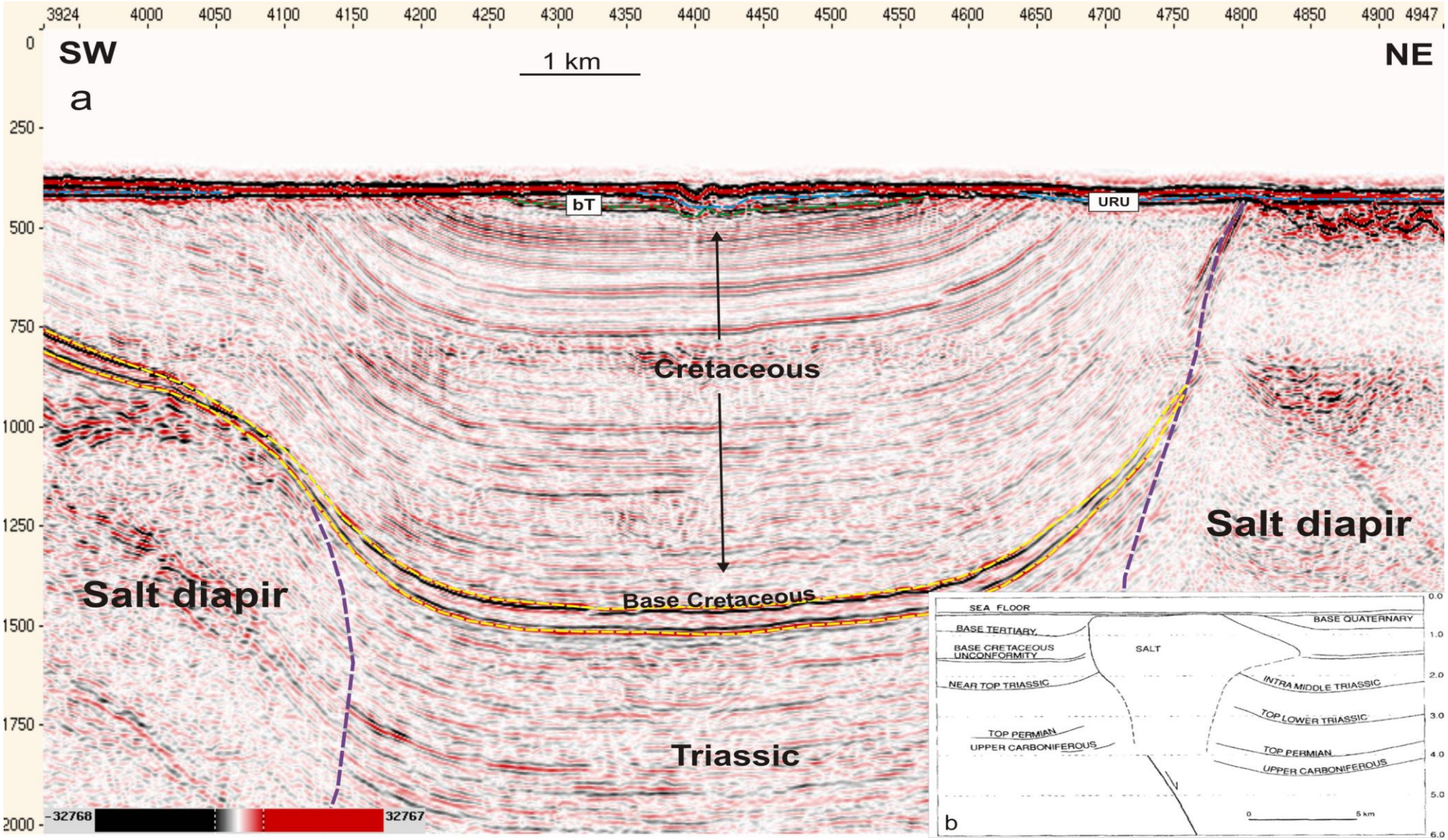

Fig. 1-8. a. Interpreted seismic profile; yellow dashed line outlines Base Cretaceous Unconformity; green line Base Tertiary unconformity; bT – base Tertiary; blue line – upper regional unconformity; URU – upper regional unconformity; velvet dashed lines shows salt diapirs (stratigraphy is based on *Koyi, 1993); b. stratigraphic units of Nordkappbanken (Koyi, 1993).*

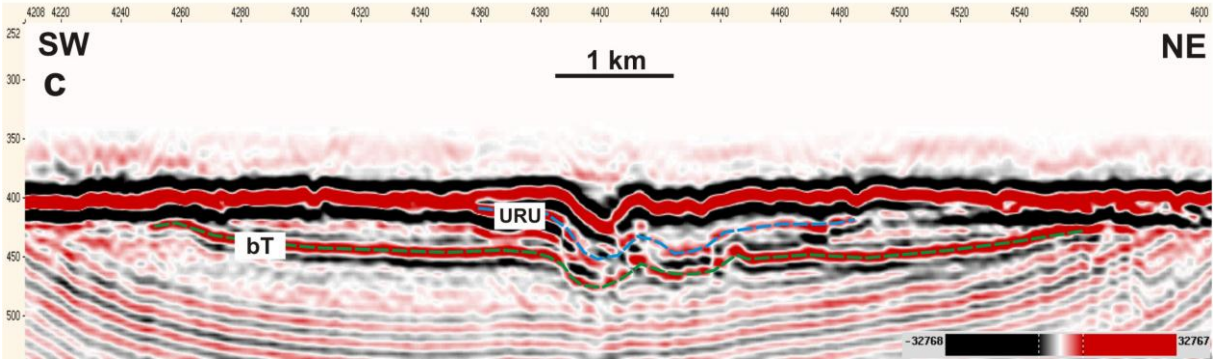

Fig. 1-8c. Zoom of seismic line (fig. 1-8a) illustrating the shallow seismic stratigraphy. A subglacial channel eroded into tertiary and Cretaceous sediments (Mattingsdal, 2008, *master thesis*)

Tertiary sediments occur directly adjacent to salt diapirs. The package bents upward but is truncated toplap by the upper regional unconformity (Figure 1-8 (a)). It means, that salt diapirs continued rising upward during that time *(Koyi et. al., 1993)*. Tertiary sediment unit contains numerous bright spots situated close to the Tertiary base (bT) (Fig. 1-8(c)). The bright spots are characterized by high seismic amplitudes and polarity changes. The bright spots and reversed polarity may suggest that underlying sedimentary units are of lower density than the units above *(Andreassen et. al., 2007a)*. According to Ryseth et al. (2003) Tertiary mudstone sediments include sand lenses that could accumulate fluids. Fluids may rise from Mesozoic units to shallower sediment units because of faulting and compression forced by salt diapirs *(Ryseth et al., 2004; Koyi et al, 1993)*. Faults are very common because the Nordkap basin evolved as a secondary rim syncline around a group of closely spaced diapirs (*Koyi et al, 1993)* (fig. 1-9).

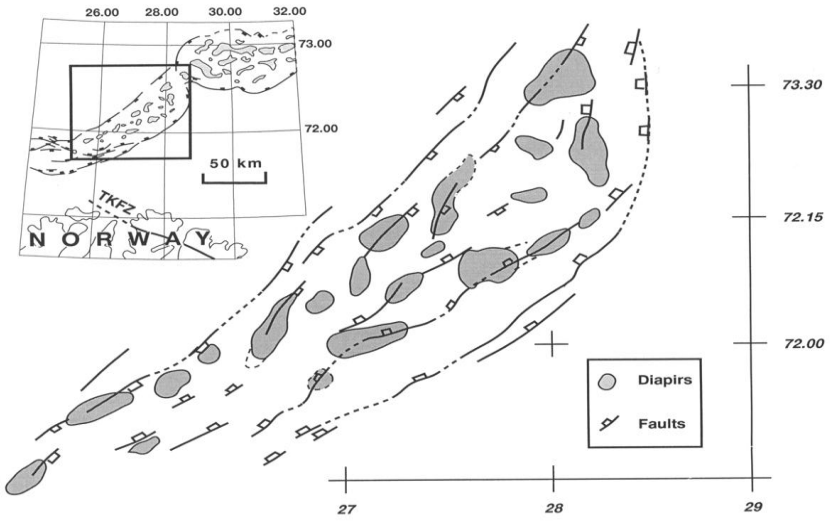

Fig. 1-9. Map of the southwest Nordkapp sub-basin (SW NKB) showing the basement faults and the salt diapirs influencing the upper sediments. TKF2 = Trollfjord-Komagelv Fault Zone (*Koyi et al, 1993)*.

Salt diapirs penetrated through Triassic and Crataceous sediments *(Chand et al, 2008)* where glacial sediments are on top, marked by the upper regional unconformity (URU). The URU reflector is located at approximately 400ms TWT (fig. 1-8c). The most prominent feature of the subsurface is a melt water channel, which is running E-W *(Mattingsdal, 2008, master thesis)*. The subglacial channel eroded into Tertiary and Cretaceous sediments (fig. 1-8c).

1.3.2. Veslemøy High (EL0001)

Veslemoy High is separated from the Loopa High by the western fault zone and is located inside the Sørvestsnaget Basin *(Breivik, Faleide, Gudlaugsson, 1998b; Ryseth, 2003; Worsley, 2008) (fig. 1-10a-b)*. Mesozoic (Jurassic) sediments indicate deep marine environments in anoxic basin conditions *(Worsley, 2008*). However, the unit is hardly defined within the Veslemøy High and it could be only traced from the Tromsø Basin towards the High. The unit is composed of black shale which is one of the best source rocks for petroleum (*Worsley, 2008) and thus a potential source for fluid migration*.

The seismic sections across the Veslemøy High (Fig. 1-10(c)) show generally the following sedimentary units: Veslemøy High (Mesozoic rocks), Tertiary sediments, glacial sediments (Quaternary), subdivided by erosional unconformities (R1, R5 and R7) *(Andreassen et al, 2007a)*. Tertiary and Quaternary sequences form the sediment wedge on the continental slope in the north-west of the 3D cube *(Ryseth et al, 2003)*.

The glacial sediments include three main sedimentary packages: GI (200ms), GII (aprx. 450 ms), GIII (600 ms). The layers are subdivided by three main reflectors (R7, R5, and R1) (fig. 1-10(a)). The interpreted horizon R7 is characterized by megascale glacial lineations (MSGL) on the paleoshelf surface. The paleo slope contains canyons and gullies. On the R5 interpreted surface the "Mega Scale Glacial Lineations" (MSGL) are preserved as well (*Sanchez, 2009, master thesis)*.

These sedimentary packages compose the sediment slope wedge and a truncated toplap to the R1 reflector (fig. 1-10c). R1 contain MSGL with two different orientations: SE-NW and N-S. Different directions of lineations identify at least two events of former ice stream activities in the area.

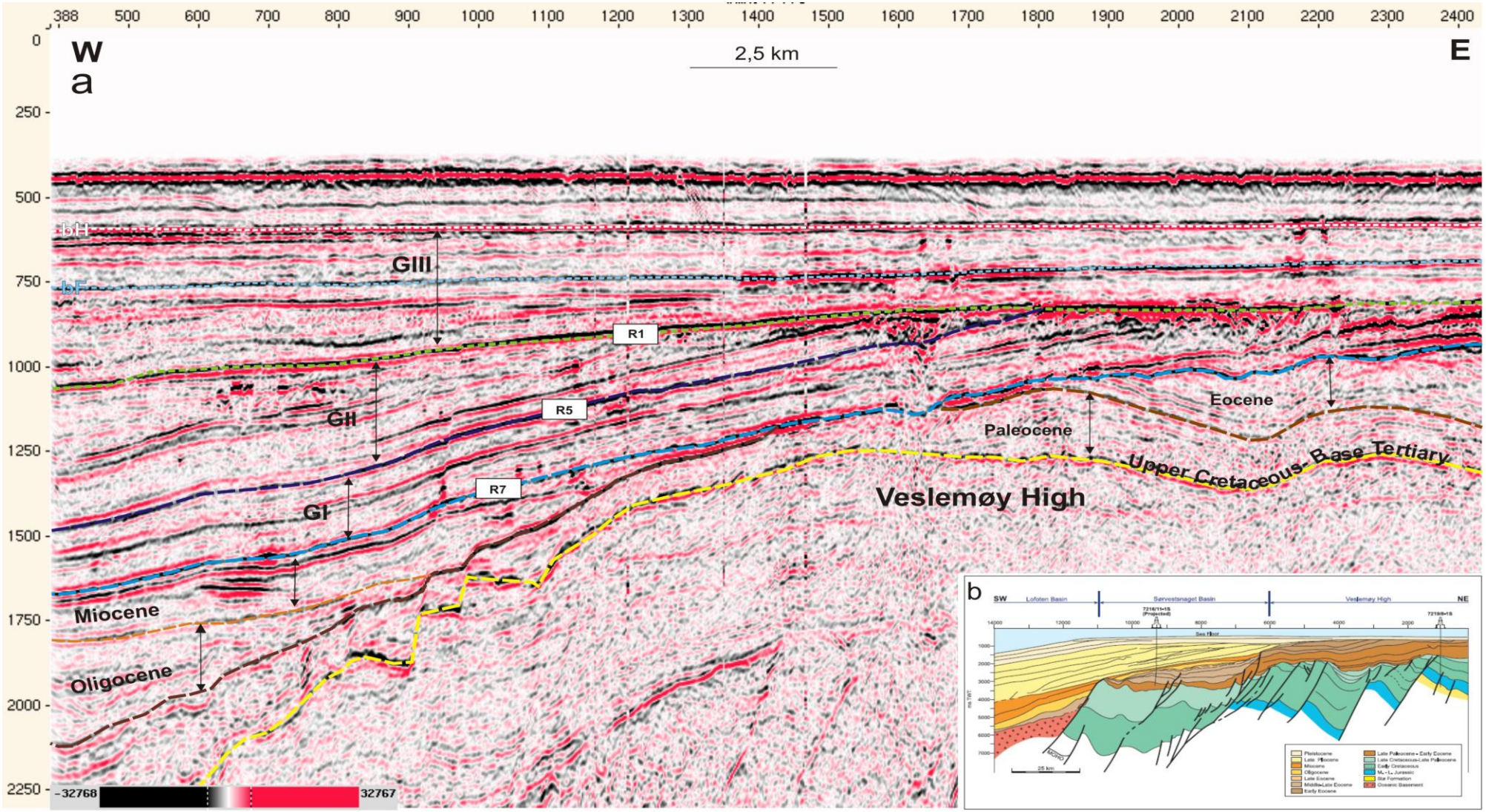

Fig. 1-10. EL0001 seismic stratigraphy; a. Interpreted seismic profile; yellow line is Upper Cretaceous unconformity/Base Tertiary (bT); brown dashed line marks the late Paleocene boundary; orange line outlines the upper limit of Oligocene unit; blue dashed line is R7/URU (base of glacial sediments/Quaternary unit); velvet line is R5 unconformity (aprx. 1,5 Ma); green line is R1 unconformity (aprx. 0.7 Ma) (the stratigraphy was based on Ryseth et al, 2003); b. Geoseismic cross-section: Veslemøy High-Sørvestnaget basin-Lofoten basin (Ryseth et al, 2003).

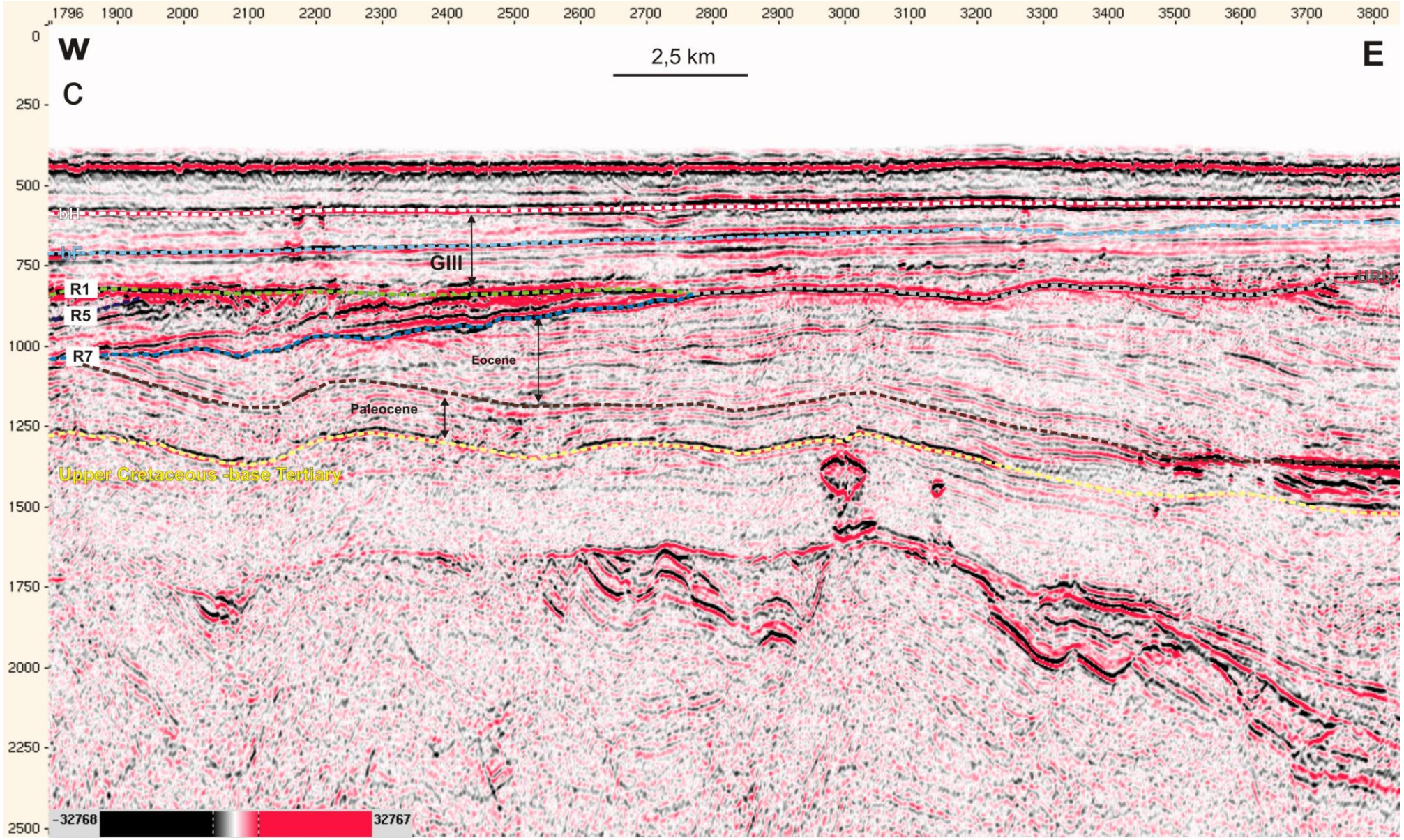

Fig. 1-10 c. The continuation of the seismic line on the fig. 10a; the grey line marks the Upper Regional Unconformity, bF stand s for.... and bH stands for Base Holocene.

1.3.3. Ingøydjupet (ST05M09)

The ST05M09 3D cube area is located partly in Ingøydjupet trough in the east, covers the paleo trough by its south-western part and the rest of the area is situated within the south-eastern slope of the Tromsøflaket. Two different morphologic conditions lead to differences in the seismic stratigraphy between the north-eastern and south-western parts of 3D survey. The differences occur previously within the Quaternary sediment package (fig. 1-11(a) and 1-11(c)).

The top of Upper Cretaceous rocks (base Tertiary) is situated at the depth 900-800 ms TWT. According to Worsley et al. (1988) the stratigraphy of the Creataceous rocks relate to Kviting formation and are of Companian – Maastrichtian age *(Worsley et al, 1988)*. The unit is composed of shale with sand inclusions. The seismic sections and interpreted base Tertiary horizon indicate that the Upper Cretaceous basement is cut by polygonal faults (fig. 1-11).

The Tertiary deposits are preserved in the seismic sections between 550-800 ms TWT. The sediments were dated to mid-late Paleocene time (*Worsley et al, 1988; Knutsen and Vorren, 1990).* The lower part of the unit shows parallel bedding of internal layers and down lapping of clinoformes dipping 1-2° (*Knutsen and Vorren, 1990)*. These layers probably are dipping due tothe three uplifts in the Cretaceous basement.

The Quaternary sediments could be identified from the depth 500-550 ms TWT. The Upper Regional Unconformity (URU) distinguish them from Tertiary deposits.. The URU is discrete along the area: it occurs under the front moraine of the Ingøydjupet paleotrough and side moraine of the modern tray basin. It inclines towards the troughs but it is not preserved in the seismic sections along the Ingøydjupet.

In the south-western part the thin Quaternary deposits are topped by the base Holocene (bH) reflector. The interpreted bH horizon shows the extension of the western branch of Ingøydjupet further to the north. The recent deposits along the SW part of 3D cube area are probably composed by stiff sediments of till and clay *(Worsley, 2008)*.

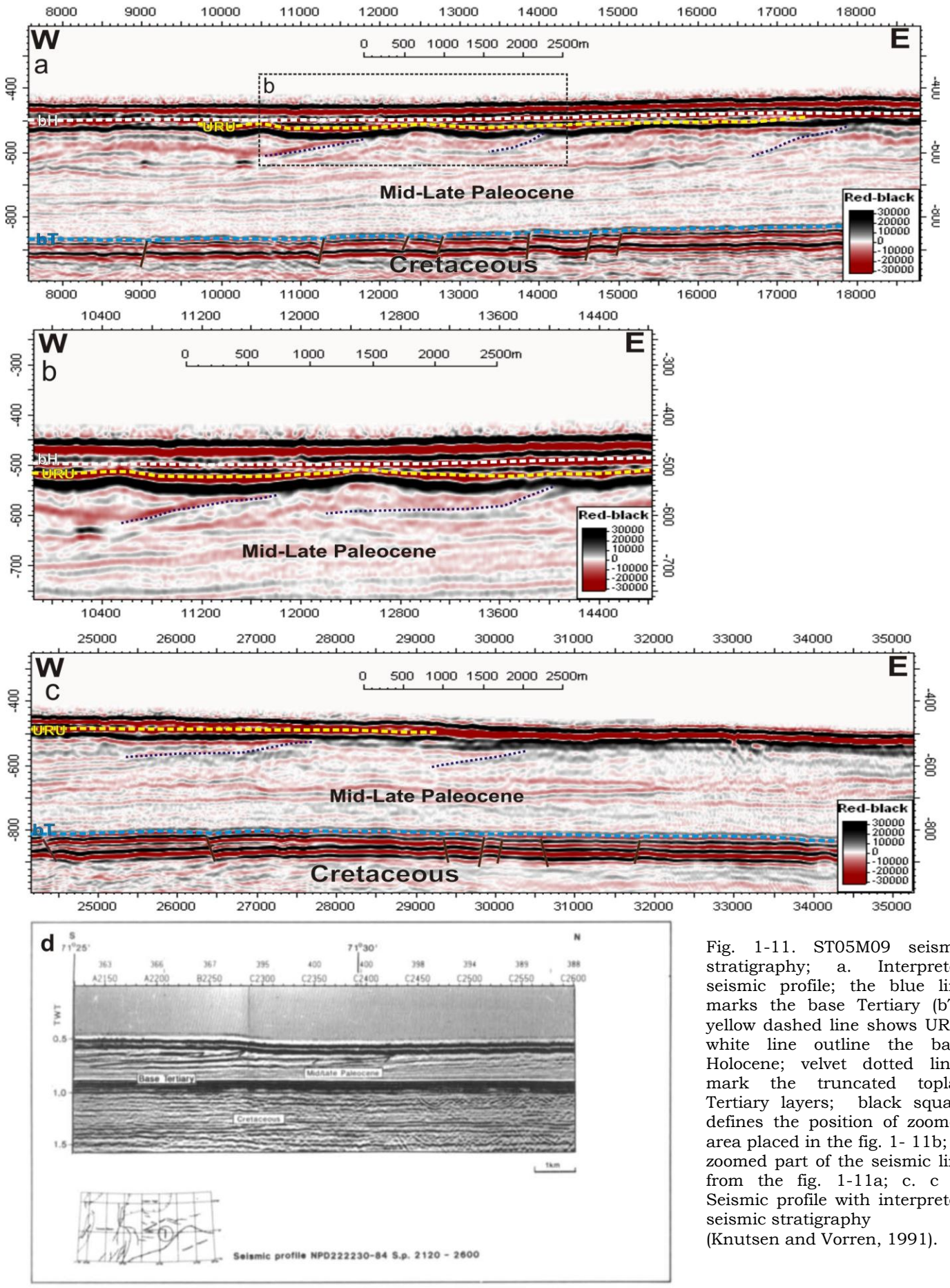

Fig. 1-11. ST05M09 seismic stratigraphy; a. Interpreted seismic profile; the blue line marks the base Tertiary (bT); yellow dashed line shows URU; white line outline the base Holocene; velvet dotted lines mark the truncated toplap Tertiary layers; black square defines the position of zoomed area placed in the fig. 1- 11b; b. zoomed part of the seismic line from the fig. 1-11a; c. c d. Seismic profile with interpreted seismic stratigraphy (Knutsen and Vorren, 1991).

1.4. Data and methods

The data consists of three separated 3D seismic cubes: ST0309, EL0001, ST05M09. The ST0309 survey is located in the Nordkappbanken at the north-Eastern wedge of Djuprenna. The EL0001 survey is situated in the northern edge of Tromsflaket and partly in the Bjørnøyrenna trough. Geologically, the area is located on the Veslemøy High in the south-east and Sørvestnaget basin in the north-west. The ST05M09 area lies in the south-western part of Ingløyduppet and westward partly in the Tromsflaket. The geological structure corresponds to the Hammerfest basin. These data were visualized and interpreted using Charisma and Petrel software.

1.4.1. Parameters of 3D seismic data

The location of 3D seismic data cubes is shown in fig. 1 and details in table 1.

Name	**Area**	**Latitude**	**Longitude**
ST0309	1871 km²	72°33'07.2" N 72°19'12.8" N 72°04'02.9" N 72°17'50.0" N	28°22'23.1"E 28°43'19.8"E 26°58'50.8"E 26°36'34.9"E
EL0001	985 km²	72°11'47.7" N 72°11'48.9' N 72°00'00.4' N 71°59'59.4' N	11°20'37.3"E 12°39'23.2"E 12°38'59.1"E 11°21'06.1"E
ST05M09	3101 km²	71°49'51.35" N 71°17'59.52" N 71°45'55.34" N 71°18'07.02" N	23°13'29.92"E 23°09'50.29"E 21°21'27.14"E 21°20'56.36"E

Table 1: Parameters of the 3D blocks

1.4.2. Seismic artifacts within 3D seismic data

— Acquisition artifacts

All data cubes contain straight parallel lines oriented parallel to inlines (fig. 3-1). They occur because of shifts in the vertical time datum between two shooting directions (which are parallel to inlines) *(Andreassen, K., 2008)*.

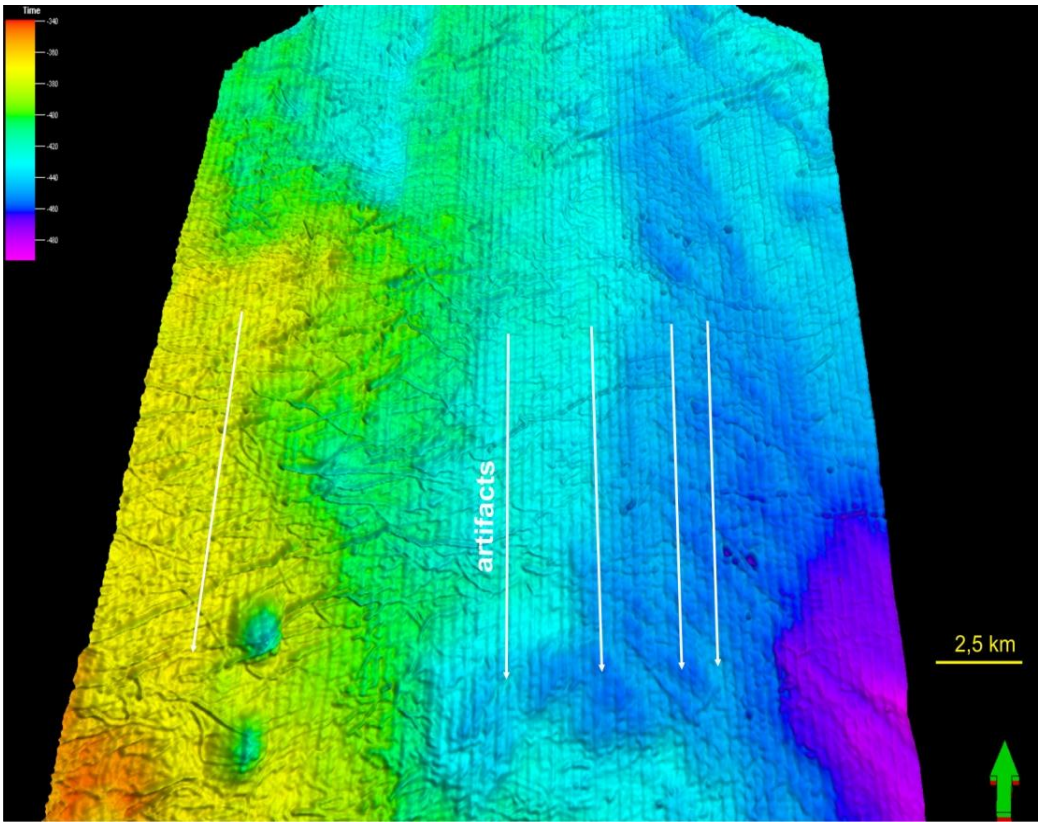

Fig. 1-12. Acquisition artifacts (ST0306 seafloor surface); white lines show direction of artifacts.

— Statistic correlation error

There are three straight lines in EL0001 stretching from SW to NE (fig. 1-13). The lines are noticeable in all interpreted horizons and attribute maps and are obviously not connected with main morphologic features in the study area. In seismic profiles they are determined as straight parallel thin columns which do not correlate with any of the adjacent reflectors (fig. 1-13). These artefacts probably appeared due to problems in the seismic acquisition or processing and have not been removed *(Gustav Pless master thesis, 2009)*.

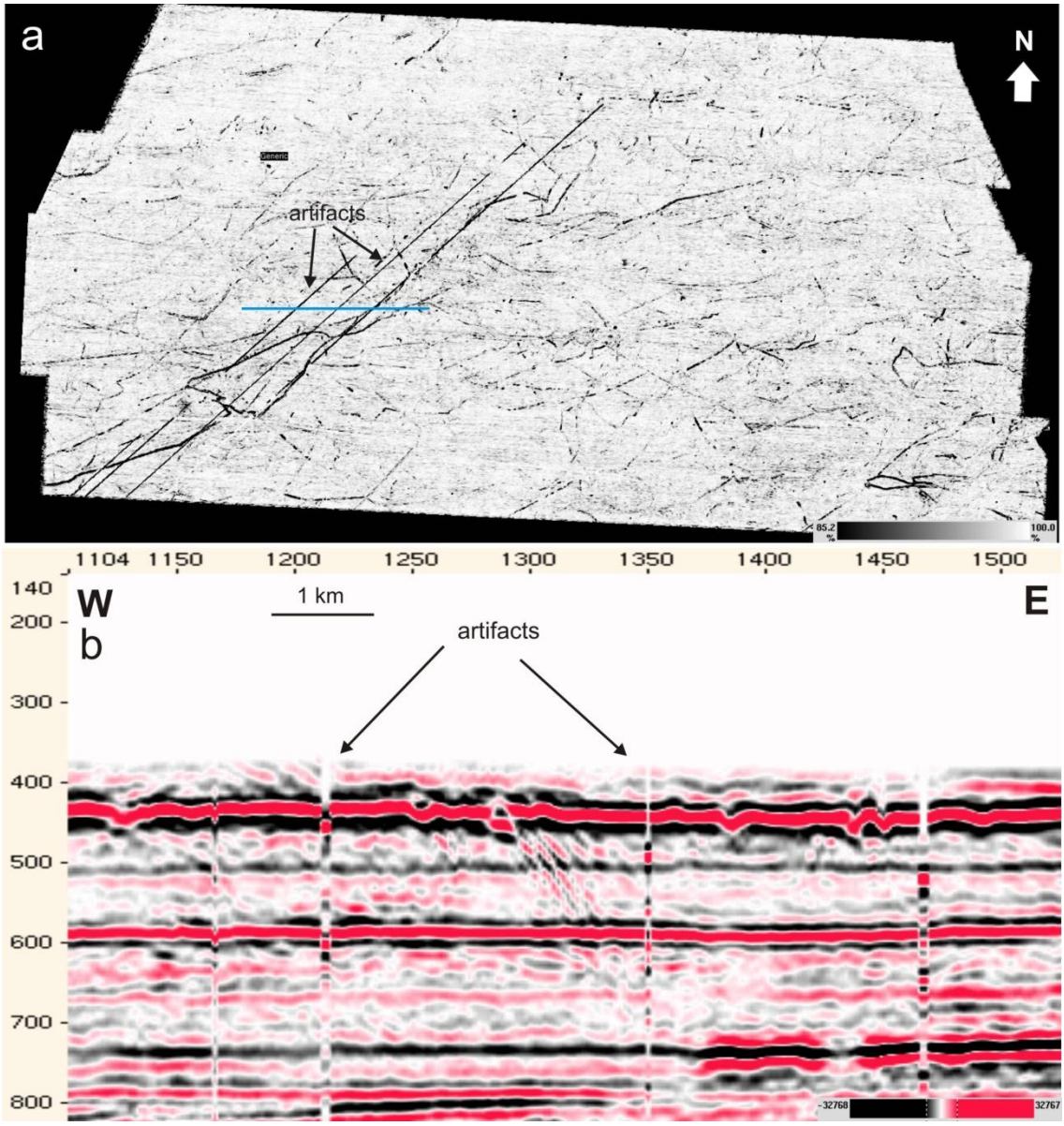

Fig. 1-13. Correlation errors; a. ELoo01 seafloor surface, correlation map; blue line is the location of seismic line shown in the fig. 1-13 b.; b. seismic section illustrating correlation errors.

- Linear noise

Linear noise occurs in the ELoo01 3D block. In seismic profiles it looks like straight columns with low amplitudes that cause the discontinuity of sediment reflections (fig. 1-14). The linear noise may be generated by other sources (boats, waves). Noise from other instruments being run simultaneously from the same survey vessel can also produce acoustic interference structures on seismic records *(Andreassen, K., compendium 2009)*.

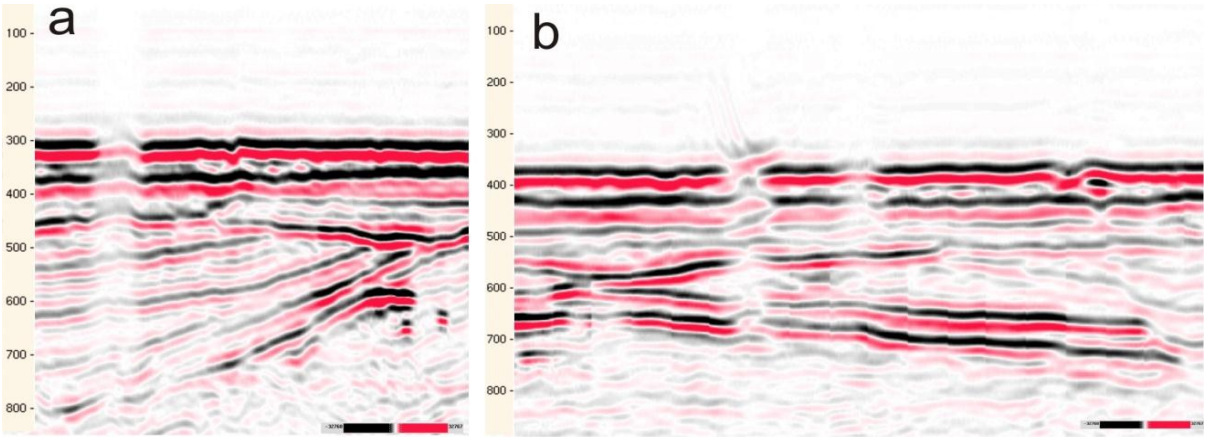

Fig. 1-14. Two examples of acoustic artifacts, that may be due to linear noise.

1.4.3. Horizon interpretation

Horizons were interpreted by selecting the strongest event of main reflections. Tracking can be done on a variety of wavelet features such as a minimum (trough) or maximum (peak) amplitude or upper or lower zero-crossings *(Chasrisma, 2010) (fig. 1-14)*.

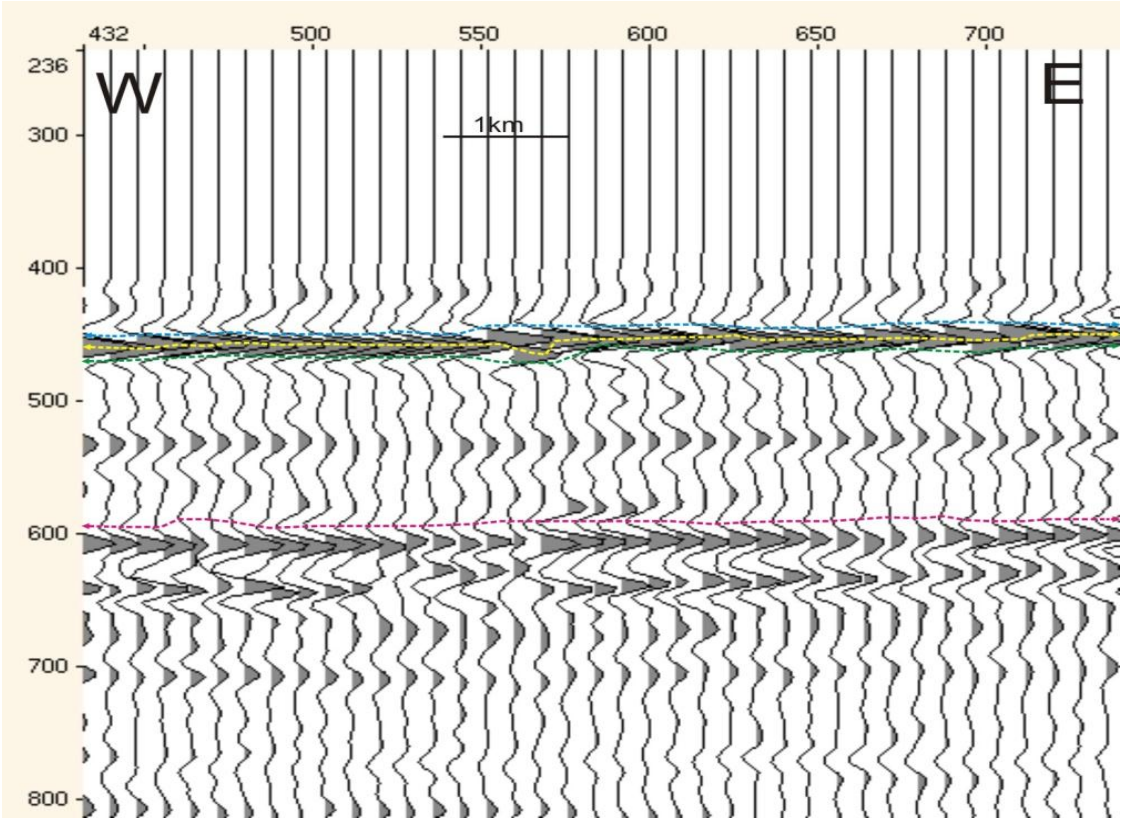

Fig. 1-14. Part of the seismic line in wiggle trace; yellow line trace the positive phase; pink line is negative; blue and green lines marks the upper and lower zero-phase.

Seismic signals are plotted according to SEG (Society of exploration Geophysicist) convention. The SEG defines **minimum phase signal** and **zero phase signal** (fig. 1-15).

Minimum phase signal starts with downward deflection (normal polarity) or upward wavelet (reversed polarity) *(Andreassen, K., compedium 2009).*

Zero-phase signal is characterized by one peak of high amplitude (that is equivalent to event) limited by two smaller lobes of opposite polarity *(Andreassen, K., compedium 2009).*

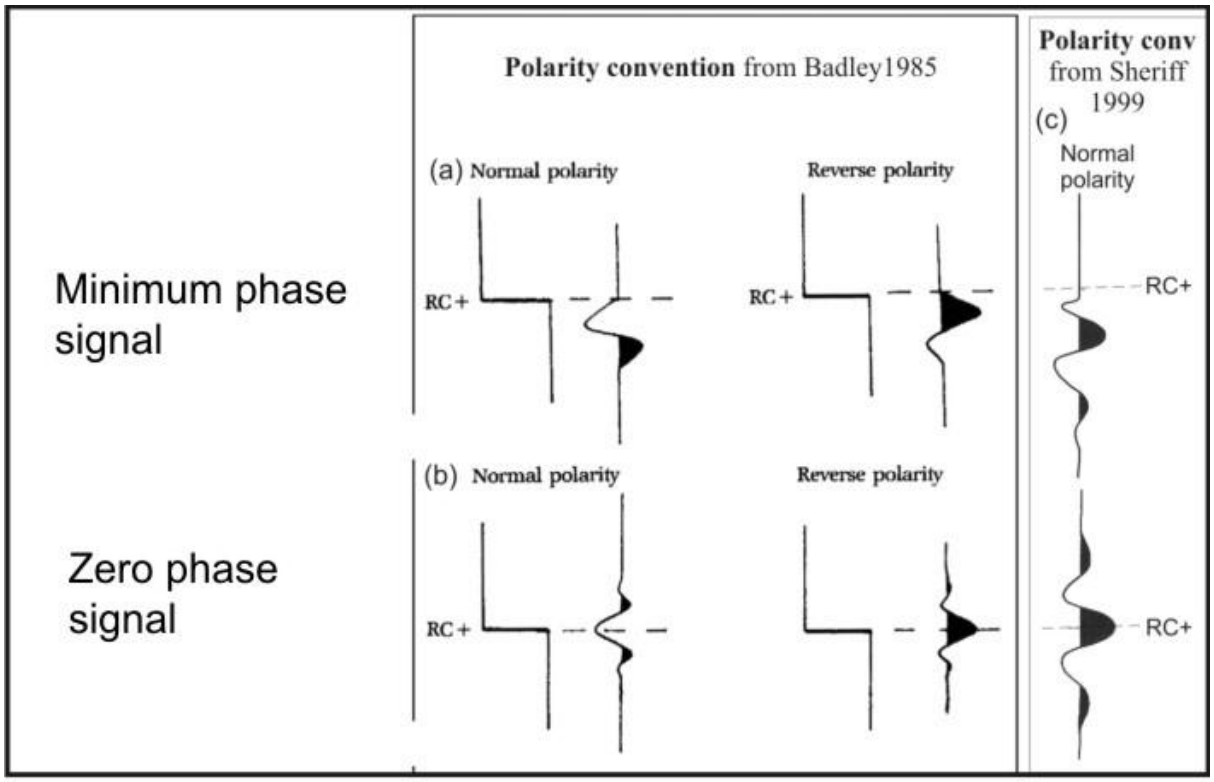

Fig. 1-15. Polarity conventions for plotting of seismic signals *(Andreassen, K., compedium 2009).*

The 3D blocks show the following polarity and phase signal (table 2):

Name	Polarity	Phase
ST0309	normal	Zero-phase signal
EL0001	normal	Zero-phase signal
ST05M09	reversed	Minimum-phase signal

Table 2: Polarity and phase signal within the 3D seismic cubes.

For each 3D cube and interpreted horizon a different wavelet phase was chosen depending on the polarity and signal phase of the seismic block. The phases which were followed during the horizons interpretations are stated in table 3:

Name of the 3D survey	Interpreted horizon	Phase
ST0309	Seafloor	Maximum phase
	URU	Maximum phase
	bT	Maximum phase
EL0001	Seafloor	Maximum phase
	bH	Maximum phase
	bF	Minimum phase
	URU (R1\R5\R7)	Maximum phase
ST05M09	Seafloor	Z-crossing phase
	URU	Minimum phase
	Top Cretaceous-base Tertiary	S-crossing phase

Table 3: 3D cube parameters showing interpreted horizons and phases.

1.4.4. Software

Charisma

Two 3D cubes (STO309, EL0001) were interpreted in Charisma (Software of Schlumberger). The software consists of three windows: 1. Main Basement, 2. Main Grid and 3. Main Seismic. 1. Main Basement is needed to visualize coordinates, inlines and crosslines, random lines. 2. Main Grid is used for horizon interpretations and also for attribute map creation. 3. Main Seismic serves the purpose of seismic profile visualization (*Schlumberger, 2000)*.

For horizons interpretation the Autotrack function was used. The **Autotrack** feature allows to quickly and accurately pick an event, as long as the signal-to-noise ratio is sufficiently high *(Schlumberger, 2000)*.

The quality of the grids depends on the chosen ASAP parameters: seeds, minimum and maximum amplitude settings, maximum dip trace and maximum amplitude change. The strict parameter use produces misspeaks in the 2D grid and it is getting harder to divide the real features and the artifacts appearing because of interpretation errors. However, in the low ASAP parameter grids only the main features are preserved and small morphological elements will disappear because of generalization of seismic interpretation.

The micro relief features could be identified by using GeoViz for grid visualization in three dimensions. The GeoViz provides an interactive suite of tools for interpretation which communicate with the other Charisma windows (*Schlumberger, 2000)*. With the GeoViz function it is possible to produce the 3D shaded surface and observe the shapes, the depth of the morphological features and their edges and extensions (*Schlumberger, 2000)*.

Petrel

The interpretations of the 3D block ST05M09 was made in the Petrel Software (Software of Schlumberger). This software has three working directories: Interpretation window for the seismic lines visualization, 2D window and 3D window.

There are three possible ways of horizon interpretation in Petrel. The first one uses 3D Track under the Setting dialog window (ASAP table) after interpreting inlines and crosslines by 2D autotracking tool in the Icon Menu (Seismic Interpretation process). The second way is the interpretation by using 3D autotracking in the Icon Bar (Seismic interpretation process). This is the quickest way, however, the interpretation causes a lot of gaps. Thirdly and in addition, horizons could be interpreted by using Paint brush tool from the Icon Menu (Seismic Interpretation process) in 2D window.

Seismic surfaces are created from interpreted horizons using **Utilities process** under the Process Pane and choosing **Surface make/edit** function. The attributes maps are made by the **Attribute maps** process under **Surface attributes** or **Volume attributes** functions (*Schlumberger, 2009)*.

1.4.5. Vertical and Horizontal resolution

The resolution influences the quality of seismic data interpretations. The vertical resolution determines the precision for separating two horizons with depth and the horizontal resolution the precisions for separating lateral distributed objects. The resolution is influenced by the wave front.

Vertical resolution

Comparison with the sonic log and the composite seismic trace shows clearly that a main problem of the seismic method is interference between the seismic responses from closely spaced acoustic-impedance boundaries. Because the seismic pulse is longer than the separation between these impedance contrasts, the reflections interfere. Interference is controlled by the length of the seismic pulse (in milliseconds) and the spacing of acoustic impedance contrasts in time, which is a function of the interval velocity *(Andreassen K., compendium 2009)*.

The vertical resolution is described as the relationship between wavelength and frequency:

Wavelength = velocity/frequency (λ=V/f) (*Andreassen K., compendium 2009)*.

The wavelength becomes larger with increasing depth and thus produces “smeared” signals from one boundary (fig. 1-16). That is one reason, why the quality of the data is reduced with depth.

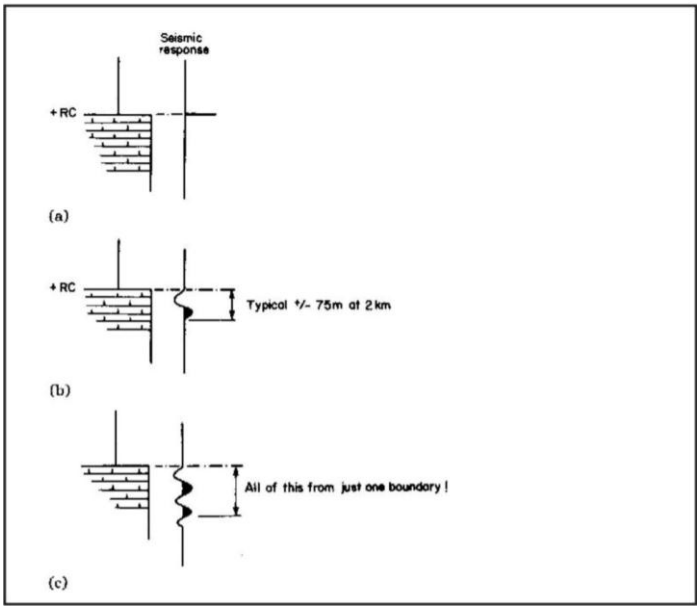

Fig. 1-16. Seismic response at a positive acoustic impedance boundary *(Andreassen K., compendium 2009)*.

Horizontal resolution

Although it is convenient to visualize seismic reflections as single rays emanating from a point, actual reflections result from the interaction of a reflecting boundary and a seismic wavefront. The wavefront affects not just a single point, but a considerable area of the reflector surface. The resulting reflection therefore is actually produced from a circular zone of a larger diameter. The extent of the zone reducing the reflection is known as the Fresnel zone *(Andreassen K., compendium 2009)*.

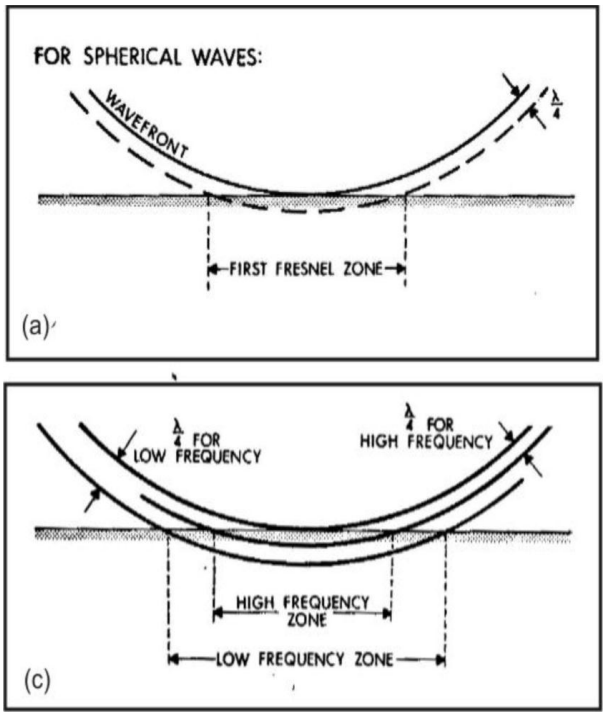

Fig. 1-17. Fresnel zone (Andreassen, K., compendium 2009).

The radius of the Fresnel zone could be estimated from the relationship:

$rf=V/2(t/f)^{1/2}$

rf – radius of the Fresnel zone;

V - average velocity;

t - two-way travel time;

f – dominant frequency in Hz.

We can see from the equation above that the Fresnel zone radius is increasing with depth, increasing velocity, and lower frequency. The horizontal resolution is hence decreasing with depth, increasing velocity and lower frequency *(Andreassen K., compendium 2009)*.

1.5. Fluid migration

1.5.1 Nature and origin of fluid migration

Fluids available to flow through the sub-seabed and seabed include various types, i.e liquids and gas that can be dissolved or occur in bubbles. Gas can derive from microbiological and thermogenic processes. Microbial processes occur in the upper seabed while thermogenic processes much deeper in the sub surface. These processes occur both in space and time *(e.g. Judd and Hovland, 2007)*. Methane is the dominant gas escaping from the seabed *(e.g. Judd and Hovland, 2007, Suess, 2010) (fig. 1-18)*.

The fluid migration is controlled by several factors:

- The sources of fluids (primary and secondary) *(e.g. Aydin, 2000; Judd and Hovland, 2007; Mazzini, 2009)*;
- Type of sediments (porous or less porous) *(e.g. Andreassen, K., 2007a)*;
- Sediment compaction *(Bjørlykke, 2006)*;
- Presence of fault system or piercement structures (intrusions, diapirs) *(e.g. Judd and Hovland, 2007; Hovland, M., 1988b)*.
- Sea level and climate change (pore pressure variations) *(e.g. Hustoft et al., 2009a, 2009b)*.

The primary source rocks of hydrocarbons are potentially from Silurian to Cretaceous and represent a deep multisource system *(Henriksen, in press)*. The secondary source are

shallow reservoirs, sedimentary trap structures that could accumulate gas that is seeping from source rocks (thermogenic gas), or biogenic methane that accumulates in gas hydrates in the upper seabed within the gas hydrate stability zone and which is very sensitive to ocean temperature changes (Chand et al., 2010; Mienert et al., 2005, *Andreassen et al., 1990)*.

Hydrocarbon migration and other fluids escaping from source rocks can be regulated by fault systems and piercement structures. Faults are permeable for fluids *(England et al, 1987; Bjørlykke et al., 2005)*. Piercement structures are diapirs and intrusions, which penetrate and deform the upper and younger sediments and often are followed by faulting processes (e.g. *Hovland, M. and Judd, A., 2007, Koyi, 1993)*.

Sediment deposits through which the fluids could migrate should be porous and permeable. Compacted sediments with low porosity and permeability such as mudstones restrict fluid flow. Examples of porous and permeable sediments are sand units or unconsolidated and unlithified deposits *(Andreassen et al, 2007a; Posamentier, 2003)*.

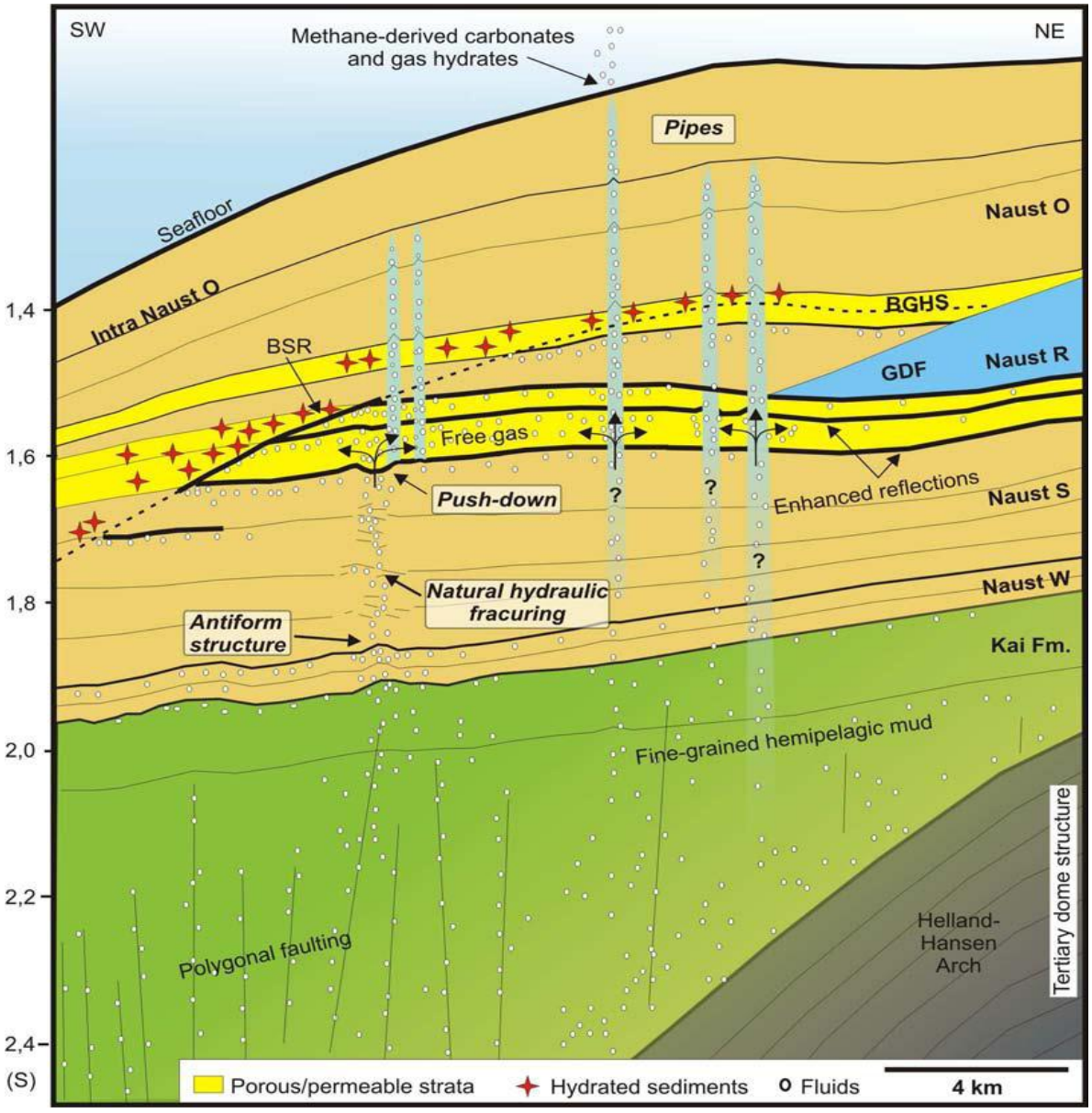

Fig. 1-18. Conceptual model of the gas hydrate and fluid flow system showing interrelations between deeper geological structures and shallower fluid migration pathways (*Hustoft et al.2007)*.

1.5.2. Types of fluid migration

There are two main types of fluid migration: lateral and vertical. Lateral fluid migration is migration along continuous permeable layers which are capped by low permeable sediment strata *(Hindle, 2007; Linn Kristensen master thesis, 2010)*. The vertical fluid movement occurs as cross-strata fluid migration, may reach the seafloor *(Cartwright et al, 2007)*. Such fluid flow systems will be an *objective of this study*.

The vertical motion is described by Darcys Law. According to it, the amount of fluids coming through the sediment column depends on rocks abilities to conduct fluids (rock physical properties) and the pore-pressure difference between two ends of the flow *(Berndt,*

2005). Generally, the sediments on continental margins compact as they get buried deeper. The increasing load causes overburden and the response is pore pressure rising and fluid migration upwards *(Berndt, 2005)*.

When fluids flow vertically, they act as seal bypass system (SBS). The seal bypass system is the large-scaled (seismically resolvable) geological feature embedded within the sealing sequences that promote cross-stratal fluid migration and allow fluids to bypass the pore network *(Cartwright, J. et al, 2007)*. Cartwright et al (2007) recognize three main seal bypass systems:

- Faults;
- Intrusions;
- Pipes.

Faults. Faults are the main conduits for fluids in many basins worldwide, especially in deeper surfaces where more consolidated to completely lithified rocks are present *(Ligtenberg, 2005) (fig.1-19)*. Fault zones could contain numerous interconnected fractures that represent preferable fluid pathways. Other fault zones may be filled with ductile clay or cement and could be either leaking or sealing when the fluid pressure increases above the threshold value *(Loseth H., 2009)*. The fault/fracture zones are subdivided into three groups (classification from Aydin A., 2000): 1. Dilatant-mode fractures/joints, veins, dykes; 2. Contraction/compaction-mode fractures/pressure solution seams and compaction beds; 3. Shear-mode fractures/faults (*Aydin, A., 2000)*.

Cartwright et al (2007) defines the two groups of fault seal bypass systems: trap-defining system and supratrap system. In the case of trap-defining faults, the vertical permeability of the fault plane and adjacent damage zones is dependent on the larger scale context of the fault and its history of motion, in combination with the local hydrodynamic boundary conditions. In the case of supratrap faults, the behavior of the faults as fluid valves from the trap is more closely coupled with the hydrodynamic conditions in the reservoir and in the sealing sequence *(Cartwright et al, 2007)*.

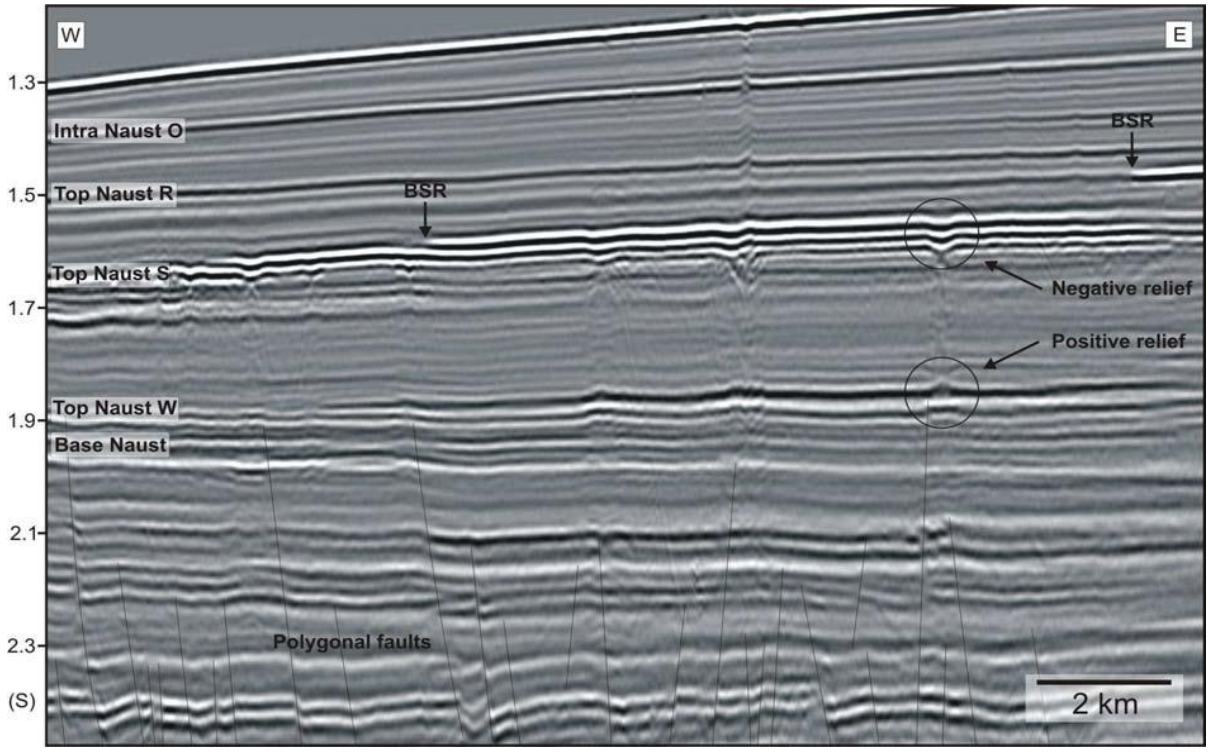

Fig. 1-19. Seismic section shows fluid migration pathways associated with polygonal faults (*Hustoft et al. 2007).*

Intrusions. Intrusive bypass is connected with piercement structures of different origin *(Cartwright et al, 2007; Hovland M. and Judd A., 2007)*. First, the intrusive event itself involves the puncturing of the seal, and the transmission of fluids through the seal along with the intrusive material. A good example of this behavior is when mud volcanoes first form. Second, when the intruded material possesses a markedly higher permeability compared to the sealing sequence, fluid flow will be focused upward through the intrusion. Examples of this case are sandstone intrusions or highly fractured igneous intrusions. Third, when the intrusion process results in intense fracturing and deformation of the sealing sequence, fluid flow can exploit the increased permeability of the sealing sequence in the contact zone. Good examples of this can be found in the shear zone around salt diapirs, or in metamorphic aureoles around igneous intrusions (*Cartwright et al, 2007)*.

The sandstone intrusions could be reservoirs for fluids affecting hydrocarbon maturation and migration pathways. The sandstone is characterized by high porosity and that is why it may be very permeable for fluids rising upward *(Polteau et al, 2007)*.

Igneous intrusions have much lower permeability for fluids in comparison with sandstone intrusions *(Cartwright et al, 2007).* In addition to fracturing associated with forceful intrusion, fracture sets also form during prograded metamorphism in the contact

aureole, during hydrothermally driven fluid loss from surrounding sediments *(Einsele et al., 1980)* and also in the thermal contraction fracturing during longer term cooling of the intrusive body itself. These different fracture sets thus provide a fracture permeability network at various scales surrounding the intrusion and occasionally within the body of the intrusion itself (*Cartwright et al, 2007)*.

Mud diapirs and diatremes are connected with mud volcanoes *(e.g. Kopf, 2002; Judd and Hovland, 2007)*. Mud diapirs are "bodies of muddy sediments driven upwards by buoyancy forces arising from the bulk density contrast between an overpressured muddy material and an overburden of greater density" *(Brown, 1990)*. Diatremes are "structures formed by the fluidization and entrainment of unlithified sediments by flowing liquids or gases" *(Brown, 1990)*. These structures deform the younger sediments and may cause the fault formation around the structures. The fluids also could be driven along the feeder pipe and conduit channels of mud volcanoes *(Judd and Hovland, 2007; Mazzini, 2007)*.

Many oil and gas provinces are associated with salt diapirs. Salt penetrate to the younger sediments and follow to radial concentric faults formation and folding *(e.g. Koyi et al, 1993, Cartwright et al, 2007)*. The fluids usually accumulate at the side of the diapir structure or directly on the top of the diapir (*Cartwright et al, 2007)*.

Pipes bypass can be identified in seismic sections as columnar zone of disturbed reflection which may or may not be associated with amplitude anomalies *(Cartwright et al., 2007)*. The gas chimneys appear mostly in fractured cap rocks *(Løseth et al, 2009)*. The pipes are usually circular or sub-circular in 3D seismic volumes (time slices, RMS maps, attribute maps) *(Cartwright et al., 2007)*. The fluids migrate from source rocks towards the seafloor through permeable or fractured sediments *(Rensbergen et al, 2007; Andreassen et al, 2007a)*. They could accumulate and cause a bright spot in the top layers or leak at the seafloor into the water column. Pipes and chimneys could be associated with fluid escape features at the seafloor such as pockmarks, mud volcanoes and/or carbonate mounds (e.g. *Hovland and Judd, 2007; Mazzini, 2007; Greinert et al., 2009)*.

1.5.3. Seismic identification of fluid migration in the sub seabed

Fluid migration could be identified in seismic profiles by several ways. First, the presence of small concentrations of gas produces a distinct decrease in compressional (P-) wave velocity and marked increase in acoustic attenuation *(Judd and Hovland, 2007)*. In

seismic profiles a bright spot usually marks the top of the reservoir and a flat spot identifies its base (*Andreassen et al, 2007a, Judd and Hovland, 2007, Løseth et al, 2009)*. Changing wave velocities and acoustic impedance could be reflected in the seismic profiles by the following features (fig. 1-20):

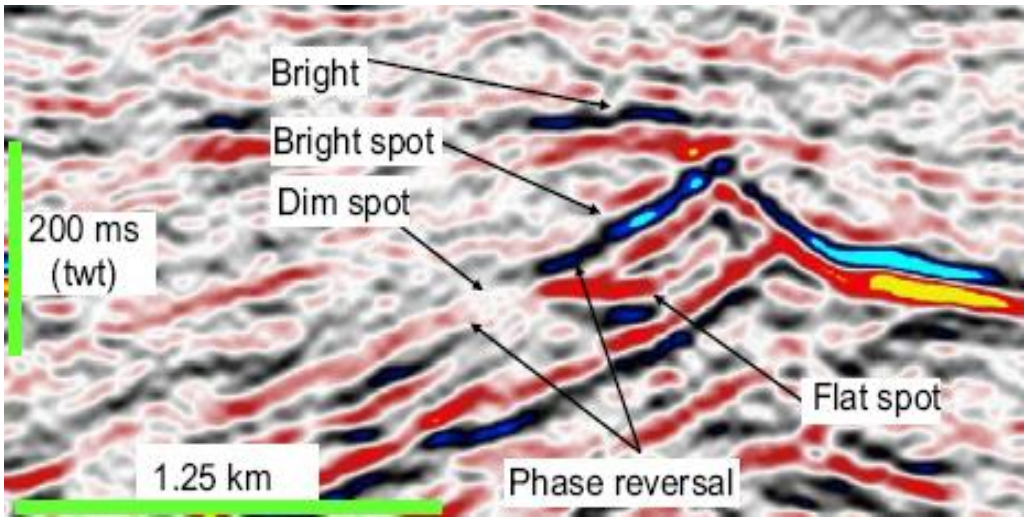

Fig.1-20. Bright spot, flat spot and dim spot (Løseth et al, 2009).

Bright spots: the presence of free gas in unlithified or porous sediments cause a reduction of P-wave velocity and will give rise to a reflection with anomalously high amplitude from the top of the gas layer *(Andreassen et al, 2007a, Judd and Hovland, 2007)*.

Flat spot: the reflection at the bottom of reservoir may occur due to the contrast between rocks and water or oil. The flat spot could be not exactly flat but it might be pulled-down.

Dim spot: the reflection from the top of the reservoir, however, in this case the acoustic impedance of underlying porous rocks is much higher than the impedance of the overlying sediment layer.

Acoustic masking: refers to an area of the seismic profile with low seismic reflectivity or where seismic reflections are highly distorted and disturbed. The features could be interpreted as scattering acoustic energy caused by occurrence of gas bubbles in the sediments *(Andreassen et al, 2007a)*.

Acoustic pipes: sub-vertical, circular, narrow zones of acoustic masking where the continuity of reflections is disrupted over a long vertical extent (*Andreassen et al, 2007a, Løseth et al, 2009)*.

Pull-down effect: the effect occurs in gas seepage zones, inside the sediment layers and gives the impression that the sediments are sagging, but in fact they are not , it is just an acoustic artifact *(Judd and Hovland, 2007)*.

Polarity reversal: phase shift of 180° along a continuous seismic reflection, so that a peak becomes a trough and vice versa *(Løseth et al, 2009)*.

1.5.4. Seafloor expressions of fluid migration

When fluids move through sediments and escape at the seabed the primary sedimentary structures may be altered and new sediments and fluid expulsion structures such as pockmarks may form *(Løseth et al, 2009)*. Pockmarks are observed worldwide along continental margins and are inferred to be indicators of fluid migration *(Judd and Hovland, 2007)*. Pockmarks are shallow seabed depressions from few meters to tens of meters deep and from tens of meters to more than 100 m in diameter. Pockmarks are generally formed in soft, fine-grained sediments by escaping fluids such as water and/or gas *(Løseth et al, Judd and Hovland, 2007)*. Pockmarks may appear as single features, as groups or as longer chains *(Chand, et al., 2009; Hovland, 1981)*. Pockmarks could be circular (elliptical) or elongated features. Elongated pockmarks tend to have the orientations of their long axis prevailing to the main bottom currents *(Chand et al., 2009, Judd and Hovland, 2007)*. There are two versions of pockmark origins. The first one explains the pockmarks creation because of gas explosion; these pockmarks must have a clear rim in 3D interpreted seismic surfaces and might be quite deep and V-shaped *(Hovland, 1981)*. However, the most common origin are formations because of more continuous fluid venting, i.e. seep processes *(Løset et al, 2009; Chand et al, 2009)*.

1.5.5. Acoustic identification of pockmarks

3D visualization tools are helpful to identify and determine pockmarks as surface expressions of fluid migrations (GeoViz in Charisma Software and 3D window in Petrel). In the 3D surface maps pockmarks, which are relatively deep features (3-5 m deep), may be characterized by a clear rim and low sediment infill so that they become clearly noticeable.

However, some of the pockmarks are small and can be hardly separated from misspicks due to very strict ASAP (Automatic Seismic Area Picker) parameters; or could be

smoothed by very low ASAP parameters. In this case, the attribute maps are very useful for the identification of pockmarks. Moreover, gas seeping through the pockmarks causes a decrease in the amplitude and frequency. Therefore, pockmarks in these maps could be detected by small amplitude or frequency anomalies. For pockmark target identification illuminated map and dip maps were useful as well (Charisma software). The most useful attribute maps are listed in table 4:

	Attribute map type	
Surface based attributes	Instantaneous amplitude	Fluid migration, changing sediment packages, reflector discontinuities
	Instantaneous Frequency	Fluid migration
	Correlation map	Scours, mega-scale leniations, channels, depressions, faults
Grid based attributes	Dip map	Morphological features (evidences of the former ice streams, depressions)
Volume based attributes	RMS Amplitude map	Changing of the sediment type, reservoirs

Table 4: Example of seismic attributes that support fluid identification

The seismic surface based attribute maps extract information from the picked seismic horizon *(Charisma, 2010)*. The grid based amplitude maps use only the interpreted horizon and show variations between grid cells and the selected horizon *(Charisma, 2010)*. The volume related attribute map describes the variations within a specified interval *(Charisma, 2010)*.

2. RESULTS

2.1. EL0001

2.1.1. Fluid flow expressions on the seafloor and subsurfaces

A total number of 22 and 32 circular and near-circular depressions were found in the seafloor and on the base Holocene (bH) subsurface respectively (fig. 2-1). The depressions on these two horizons are circular or subcircular with ratios between long and short axes 0.7-0.9 (fig. 2-2). The shapes and depths of the features could be correlated for some with the same depressions in the base Holocene subsurface.

The depressions on the seafloor are situated between the depths of 420-500 m. They are concentrated in the north-eastern part of 3D block and along the bottom of giant ploughmark stretching NE-SW through the seafloor horizon (fig. 2-1).

Depressions on the base Holocene subsurface are widespread and occur within the depths interval 515-525 m. The average long axis length for the seafloor depressions varies between 500-650 m and the diameter of subsurface depressions varies from 750-900 m. The common depths for depressions in both surfaces are approximately 3,5-5 ms TWT and dominated orientation for the long axes is E-W and NE-SW; however the depressions on the east of the bH paleo surface have a preliminary orientation to N-S. The depressions on the seafloor reflector are smaller than bH depressions and are more elongated (the short and long axis ratio of the features for seafloor vary between 0.7-0.8 while for bH reflector it alters between 0.8-0.9) (fig. 2-1).

In comparison with bH depressions the seafloor depressions are characterized by the irregular shape and noticeably more disturbed and eroded, whereas the features on the bH are previously circular and clearly defined. The base of depressions Nr. 1, 2, 3, 12 (seafloor reflector) are crosscut by irregular furrows that were identified as iceberg ploughmarks (fig. 2-3). The remaining depressions show no evidence for iceberg erosion. It signifies two possible events of seafloor depression formation: one occurred before or during the Last Glacial Maximum and the second was after the glacier retreat.

Depressions N 1,7,8,9, 13, 14, 15, 22 on the seafloor are associated with similar depressions on the bH horizon. Other depressions on seafloor surface and on the base Holocene horizon do not show a correlation; therefore the depressions on the seafloor and in the base Holocene horizon were created during two different time intervals. The bH depressions do not contain any iceberg scours.

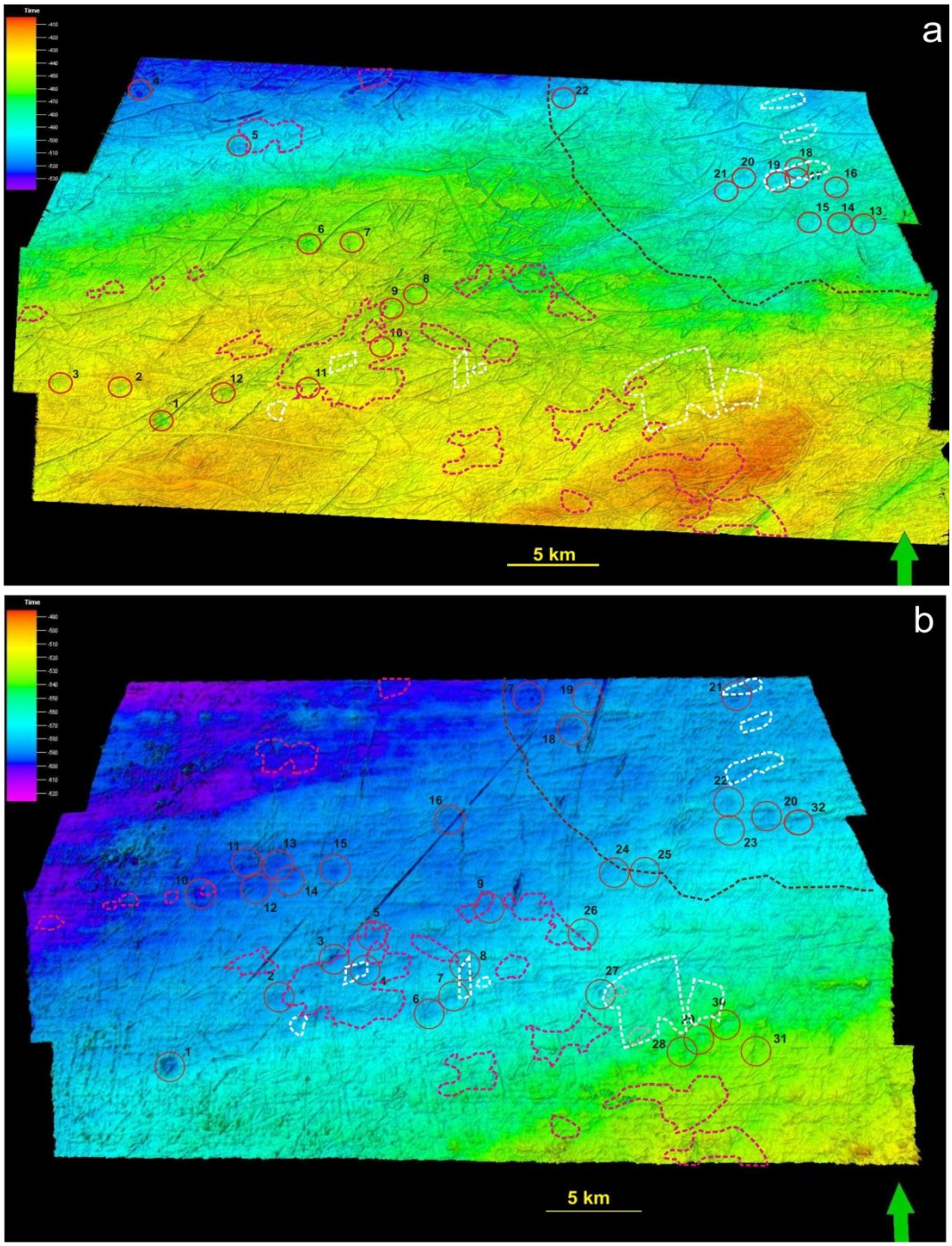

Fig. 2-1. Circular depressions distribution on seafloor and base Holocene (bH) subsurface; a. Seafloor horizon in the 3D window; b. bH horizon in the 3D window; white polygons outline high amplitude anomalies on the bH; pink lines mark seismic anomalies on the bF reflector and brown line defines the high amplitude area on URU.

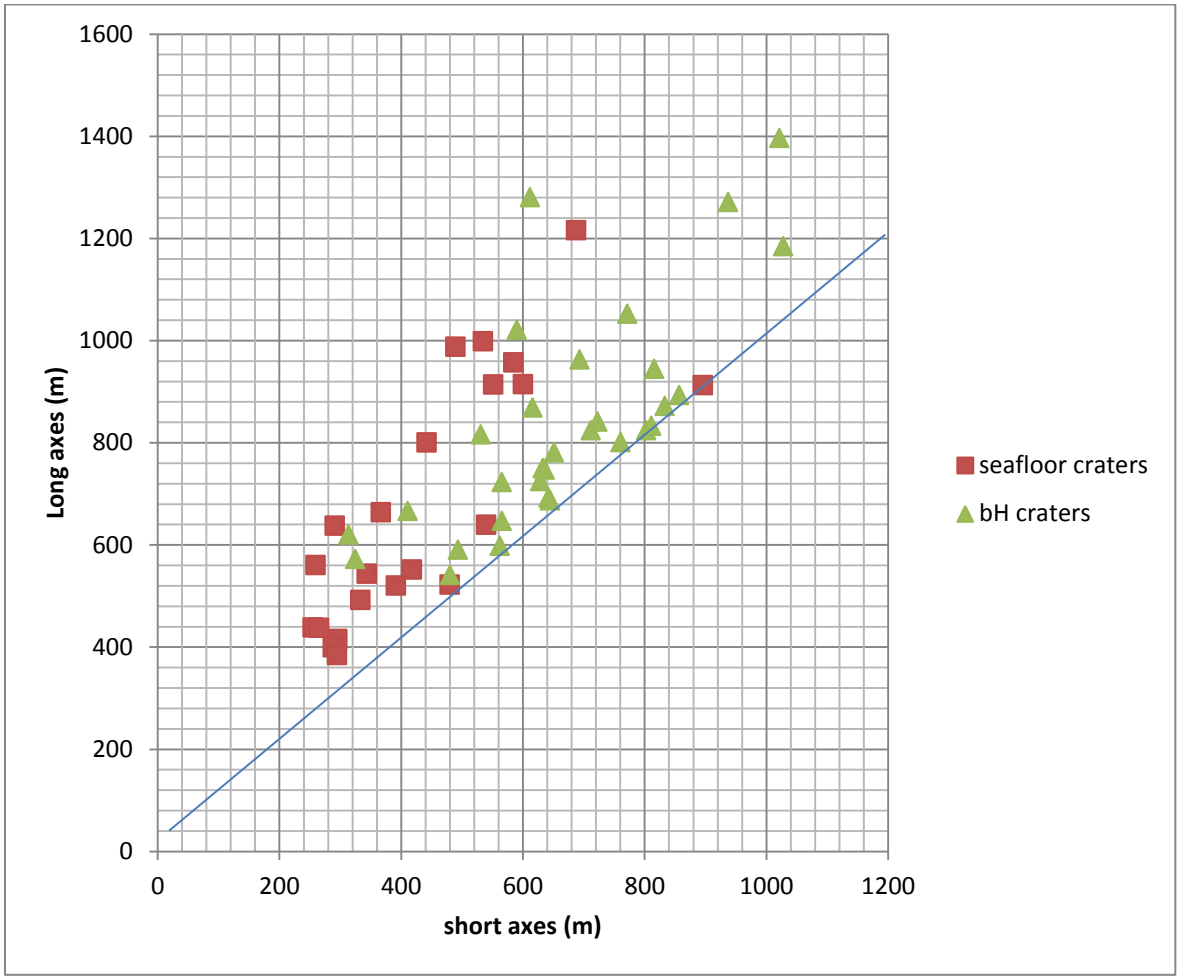

Fig. 2-2. Diagram shows relation between long and short axis of mapped depressions.

Most of the depressions are associated with high amplitude anomalies in bH, bF and URU (figs 2-1 to 2-4). The seafloor reflector shows three depressions (N17, 18, 19) that are seated above the anomaly on bH reflector (fig. 2-1 a); three (N 5, 10, 11) depressions occur above the bF anomalies and ten features are located above the URU large amplitude anomaly in the north-east. At the base Holocene subsurface, four (N4, 8, 21, 27) depressions are associated with the bH high amplitude anomalies; five (N2, 3, 4, 5, 10) depressions are situated above the anomalies on bF; and ten features are related to high amplitude anomaly on URU. The depressions could be interpreted as pockmarks (fig. 2-1 to 2-4).

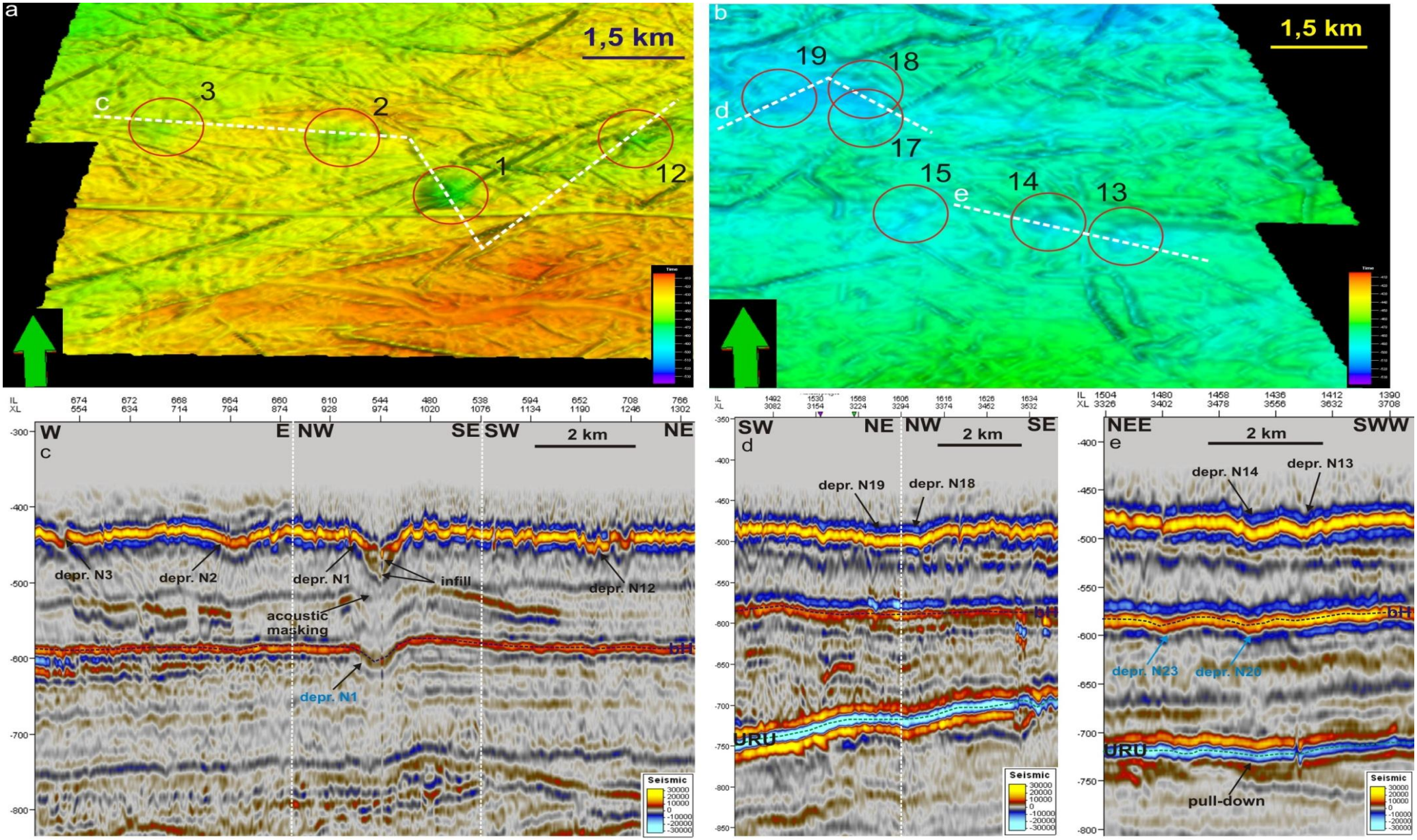

Fig. 2-3. Examples of seafloor depressions; a. and b. seafloor surface in 3D window; c., d., e. the seismic sections marked in fig. 2-3a and 2-3b.

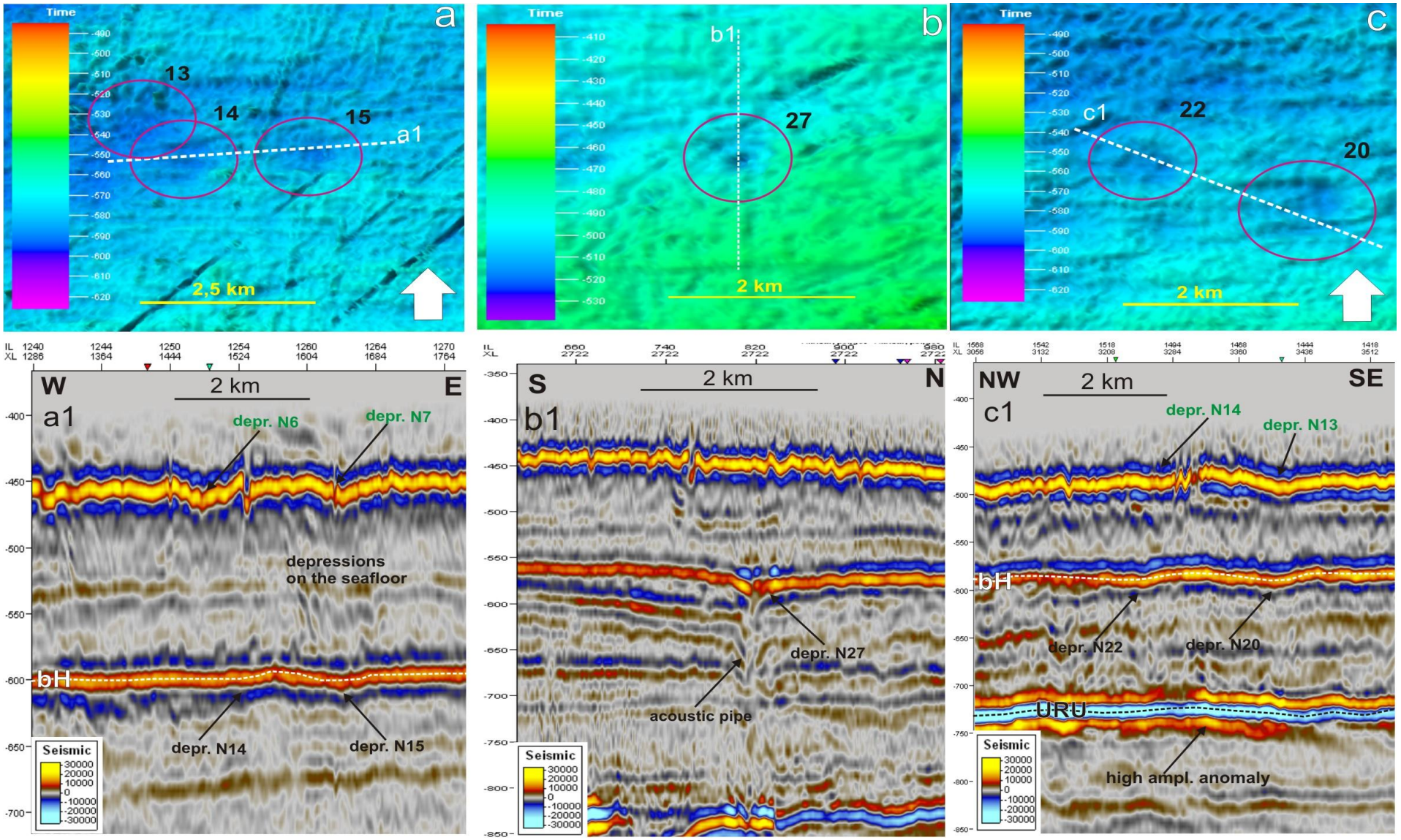

Fig. 2-4. a,b and c provide examples of circular and subcircular depressions at the bH reflector (3D illuminated surface of bH horizon in 3D view); a1, b1 and c1 show the seismic sections denoted in the fig. 2-4a, 2-4b and 2-4c.

2.1.2. Small irregular depressions on the top of the chimney structure (bH horizon)

Twenty-one small depressions concentrate in the south-eastern part of the bH horizon (fig. 2-5). The long axis varies from 185-300 m and the short axis from 120-150 m, with average values of 218 m and 117 m respectively. The common depth of depressions is 2-4 ms TWT, and the features have various orientations: NNE-SSW, E-W, SE-NW.

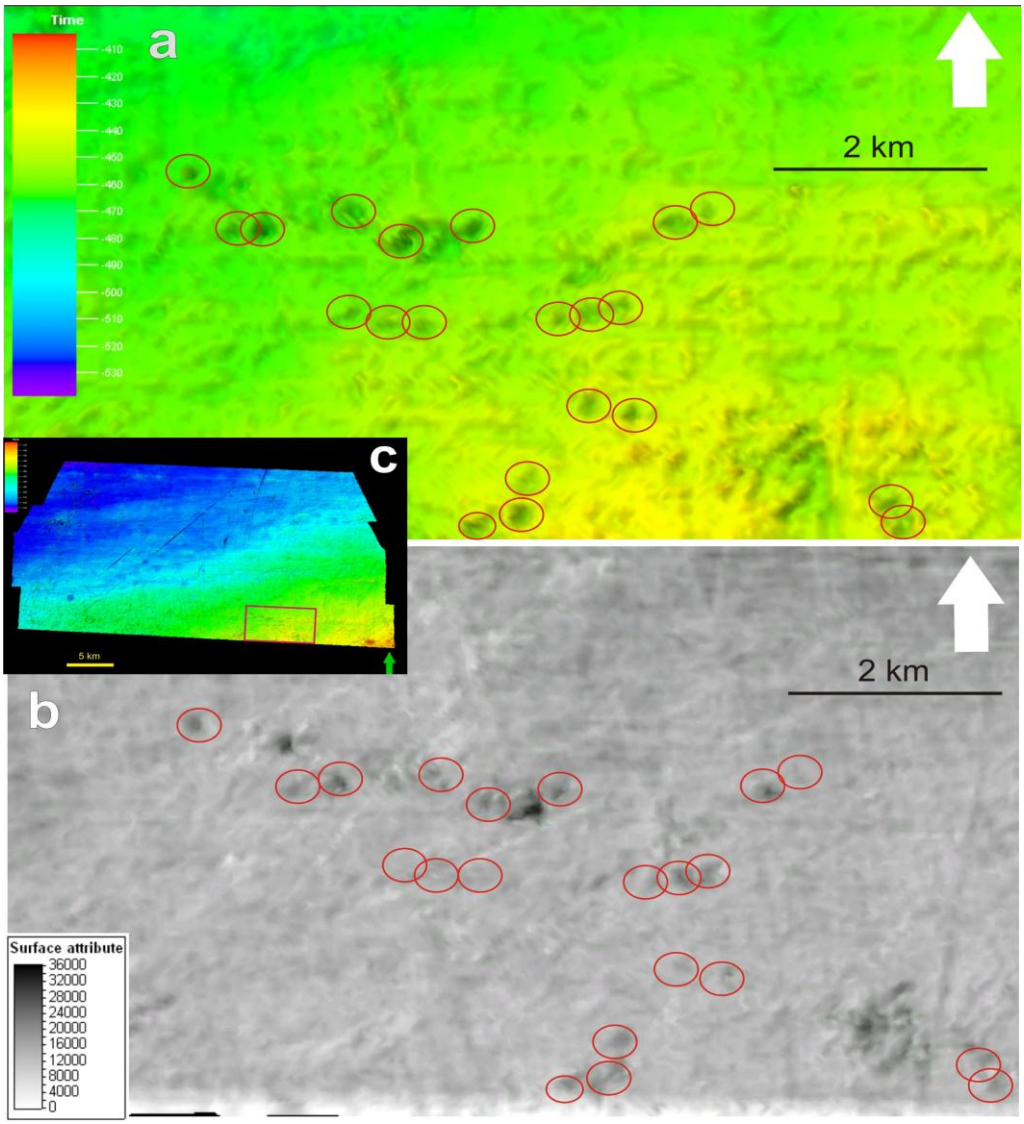

Fig. 2-5. a. part of the 3D illuminated surface show small depressions on the bH reflector; b. minimum surface attribute amplitude map (offset 0, search window 50); c. 3D sub surface of bH horizon, red square outlines the area shown in a and b with high concentration of depressions.

The observed depressions show amplitude increases (fig. 2-5b). In the seismic profile the depressions are seated above high amplitude anomalies in the bF horizon and connected to acoustic chimney at 730 ms TWT (fig. 2-6).

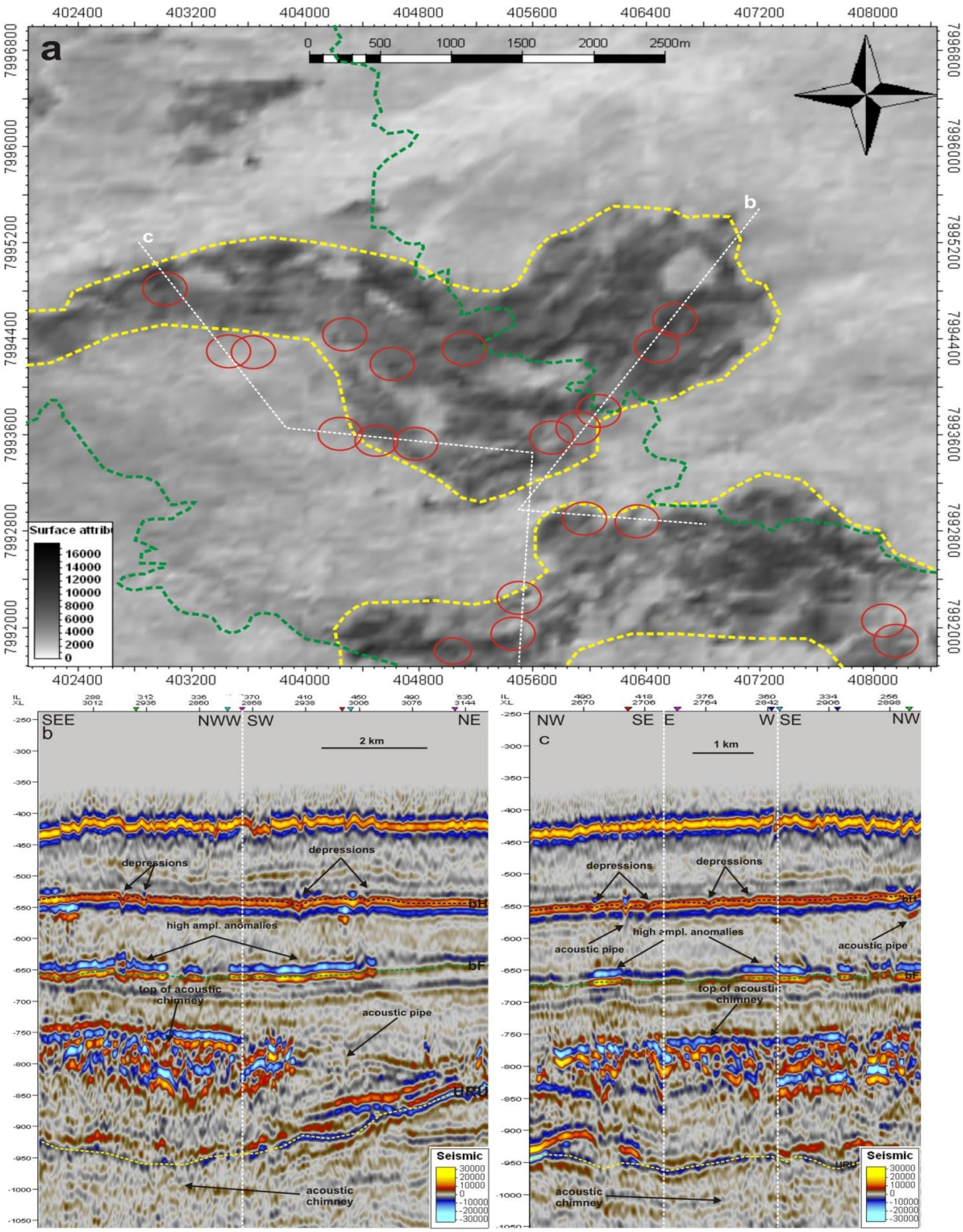

Fig. 2-6. The correlation between depressions on bH horizon, high amplitude anomalies and acoustic chimney at 750 ms TWT; a. the part of RMS amplitude map (offset -200, search window 100), yellow area mark the high amplitude anomalies on bF horizon, green dashed line denotes the top of acoustic chimney extension; b. and c. seismic profiles (the location of them is marked in the fig. 2-6a) show high amplitude areas

In the seismic profile the high amplitude anomaly terminates at the depth of 750-850 ms TWT.. The high amplitude area can be followed by clear acoustic masking extending from about 1800 ms TWT (from Cretaceous rocks). The feature could be interpreted as an acoustic chimney.

The two areas with high amplitude values are located on the bF reflector directly above the acoustic chimney. The reflectors are flat in the seismic profile and are associated with increasing acoustic impedance contrast inside the bF reflector. However, the polarity does not reverse, so that the bright spots are probably related to sediment changes inside the bF horizon from softer sediments to denser and porous deposits (e.g. sandstone) that could contain fluids that are seeping upwards *(Andreassen, 2007a)*.

The depressions on the bH are connected with thin acoustic pipes that provide evidence forfluid leakage from the sediment blocks on bF towards the modern sediments. The depressions on the base Holocene subsurface could be interpreted as unit pockmarks formed as a result of fluids seepage *(Judd and Hovland, 2007; Greinert, 2010)*.

2.1.3. Acoustic pipes connected with features on the seafloor and bH horizon

The seismic attribute maps made for bH horizon contain four amplitude and frequency scattering spots that could be identified as acoustic masking. Fig. 2-7 displays an example of a seismic amplitude attribute map for the subsurface where the acoustic pipes are clearly preserved. Two acoustic pipes connect with the depression N1 and N27 at the bH reflector in the seismic sections (fig2-3c and fig.2-4b1).

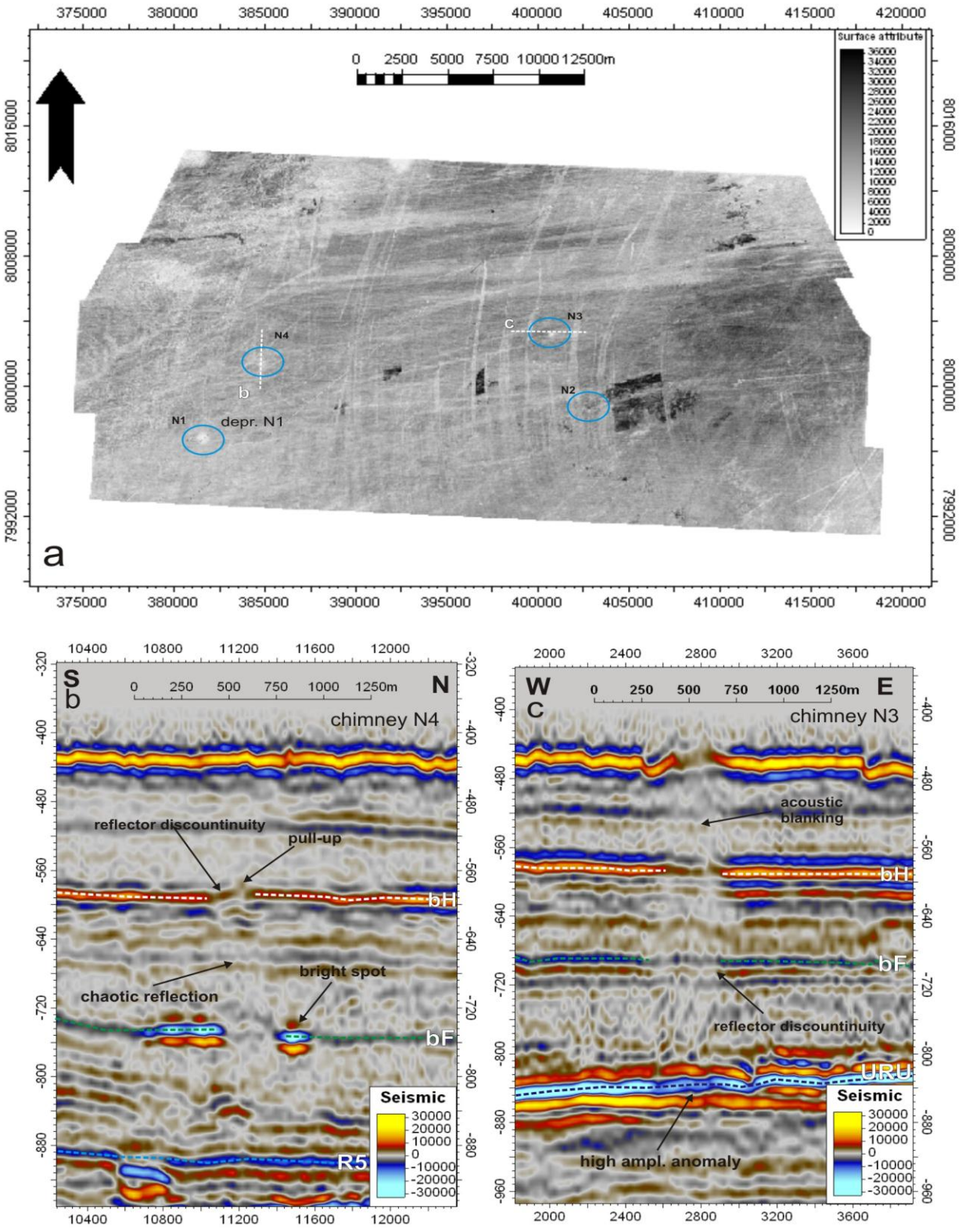

Fig. 2-7. Acoustic pipes; a. Seismic attribute maximum amplitude map (offset 0, search window 50); pink circulars correspond to high amplitude anomalies on bH reflector; blue circles mark the low amplitude areas; b and c. seismic profile across N3 and N4.

N	expression	extension	Long axis	Short axis
1.	Depr. N1 seafloor and bH	bF-seafloor	798,55 m	714,5 m
2.	Depr. N27 bH	R5-bH	198,09 m	113,76 m
3.	Mould on the seafloor	bE-seafloor	424,74 m	345,03 m
4.	Reflector discontinuity of bH	R5-bH	383,8 m	207,8 m

Table 5: Parameters of acoustic pipes

Acoustic pipe N1 (fig. 2-3c) is associated with depressions N1 at the seafloor and at the bH reflector. It extends from bF horizon towards the seafloor from the depth 750 ms TWT. The pipe is circular in shape; the length of the long and short axes are 798,55 m and 714,5 m respectively. In the R1 reflector the pipe is associated with a depression which is slightly shifted to the north from the seafloor and bH depressions (fig. 2-3c).

Acoustic pipe N2 (fig. 2-4b1) corresponds to the depression N 27 on the bH reflector. It extends from R5 to the bH horizon and is marked with a high amplitude at the top. In the amplitude map the pipe could be identified as high amplitude spot. The pipe is elongated in 2D and 3D surface and is oriented to S-N by its long axis.

Acoustic pipe N3 (fig. 2-7c) is expressed by the pull-up at the seafloor reflector and the bH horizon. In the seismic profile it is characterized by the reflector discontinuity or acoustic blanking and could be traced from the URU high amplitude anomaly upwards (500 ms TWT) (fig. 2-7c).

Acoustic pipe N4 (fig. 2-7b) is less clear if compared to the previous feature. It is located between R5 and the bH reflector and causes a slight pull-up effect at bH. In addition, it is associated with two high amplitude anomalies at the bF reflector at 720 ms TWT.

2.1.4. URU surface glacial morphologies

The URU horizon contains various glacial and subglacial morphological features where fluid-flow expression features such as mounds and depressions concentrate along the paleoshelf (fig. 2-8a and 2-10). The distribution of depressions indicate a correlation with the main glacial morphological elements: approx. 65 % of th e depressions are

situated in the front zone of glacial troughs and ridges that were interpreted as drumlins. Onthe ridges depressions are not highly preserved.

The most noticeable morphological features on the continental paleoshelf are the three large troughs which are situated in the in the south-east of EL0001 3D survey (fig. 2-8). The troughs have a flat bottom, are 25-30 m deep and SE-NW oriented. The largest trough, which is located in the south, is 5 km wide in the broadest area and approx. 2 km wide in the narrowest part. The second trough is much narrower. The trough is situated mostly outside the 3D block area but itsfront zone is visible. The large scale glacial morphology of the Barents Sea is characterized by the alternation of shallow banks and deep glacial troughs *(Andreassen, K., 2008)*.

The bottoms of the troughs are cut by parallel lines that consist of shallow grooves (0.3-0.5 m deep) and low ridges (0.3-1 m high) called lineations. The liniations are partly disturbed and eroded but well preserved on the south-western slopes. They can be traced outside the troughs towards the paleo continental shelf break. These elongated ridge-grooves features were described in various publications as mega-scale glacial liniations (MSGL) (*Andreassen, K. et al 2007a, 2008; Ottesen, et al, 2005; Winsborrow, M et al, 2009)*. The liniations on the URU horizon probably were formed by the rapid glacier flow according to their high elongated ratios 11:0.1 *(Andreassen, K. et al, 2008).* The ratios were measured on the assumption of equation (*Benn D.I. and Evans D.J.A., 1998)*:

R=l\w; where R-the ratio of the stream line;

l – the length of the leniation;

w – the width of the feature.

The orientations of MSGL and glacial troughs crest lines are not equivalent to each other (fig. 2-8). The difference in orientations could be related to reorganization of the ice sheet flow direction (*Benn D.I. and Evans D.J.A., 1998; Andreassen, K., 2008).*

East of the paleoshelf and to the north from the glacial troughs there is a large, deep and straight groove (7-10m deep and 540-550 m wide) which has the same orientation with the troughs in the south. The groove is U-shaped and contains three depressions on its bottom (fig. 2-8a). Similar features were described by Kuijpers et al. (2007) offshore Greenland and explained as giant iceberg ploughmarks.

The paleo surface includes three elongated ridges with E-W orientation (fig. 2-8). The highest feature is located in the north-east of the shelf and approx. 15 m high, 12,7 m long and 1,8 m wide ; the second elevation is 13 km long, 2 km wide and 10 m high. The third ridge is the smallest and it is only 5-7 m high,9 km long and 1,5-2,1 km wide. The ridges could be recognized as drumlins or mega-flutes that presumably were created by the erosional and depositional effect of the flowing ice (*Benn D.I. and Evans D.J.A., 1998; Boulton, 1987).* The features are not exactly straight and the direction of the crest lines curve to SW.

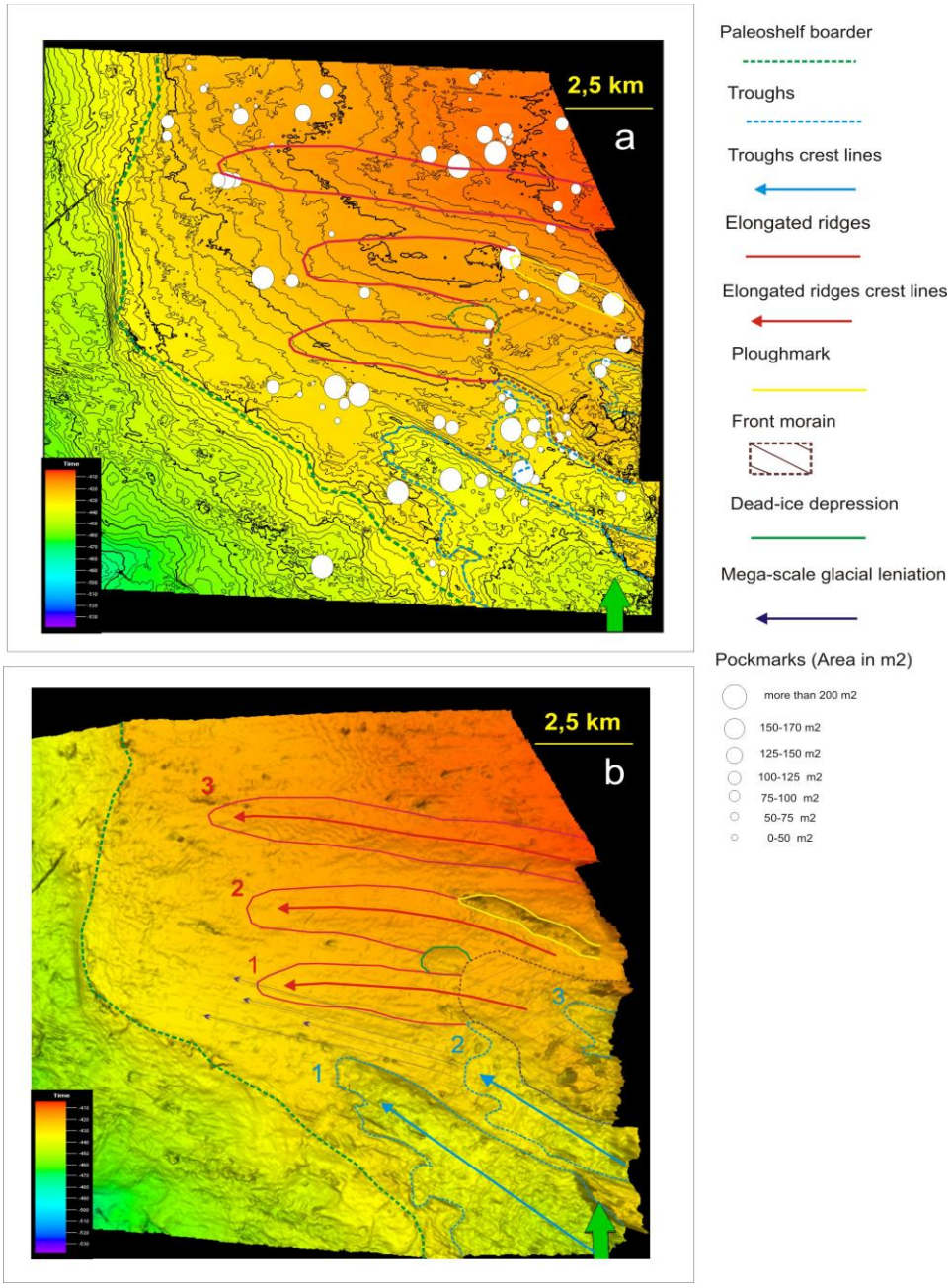

Fig. 2-8. Glacial geomorphology of the URU shows glacial ridges (red) and troughs (blue).

Between the second and third ridge there is a sub-circular depression which is 1,8 km long and 1,1 km wide with an orientation to the SE-NW by its long axis; the depressions is approx. 10 m deep (fig. 2-8). In the seismic profile (fig. 2-9), there is no evidence for an associated fluid migration that created the depression. In the 3D surface it is noticeable that this depression is connected with the second glacier trough with the depression extending to the third ridge. The depression could have been created by dead-ice that was trapped between the two ridges.

The depression N 9 (fig. 2-9) is located in the bottom of the “dead-ice” depression. The depression is elongated and oriented to the SE-NW. In the seismic profile it is followed by normal faults, a negative phase at the URU reflector and a positive phase at the pull-up reflection (fig. 2-9). The depression can be connected with normal faults extending from 1200 ms TWT to the shallow subsurface. As there are no clear evidences forfluid seepage the depression may have been created by an iceberg which could have been trapped inside the large depression.

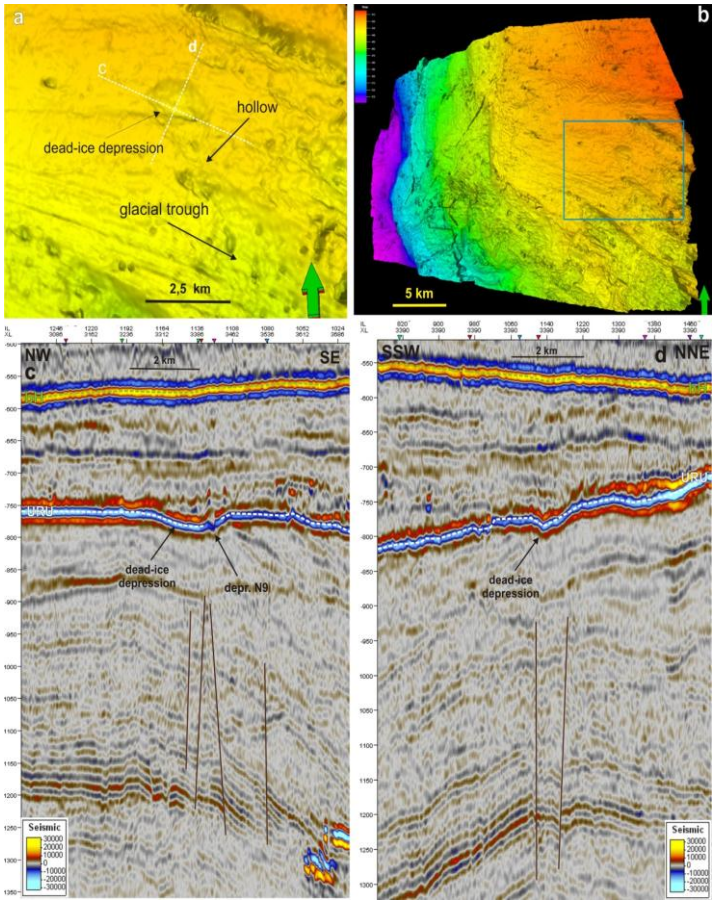

Fig. 2-9. Potential “dead-ice” depressions; a. part of 3D correlated surface of URU; white dashed lines show the positions of the seismic profiles across depressions; b. green square mark detailed area in figure a; c and d. seismic profiles show faults and depressions;

2.1.5. Depressions at URU

Within the URU interpreted horizon 83 depressions were mapped (fig. 2-10). They show a predominantly concave shape but five mounds are also visible. The observed features concentrate mostly at the paleoshelf between the depths of 550-700 ms (TWT) and do not appear at the paleoslope deeper than 700 ms (TWT) (fig. 2-10). Four main areas mark the concentration of palaeo-seabed fluid flow release features (fig. 2-10). Their distribution at the paleoshelf appears to be not random.

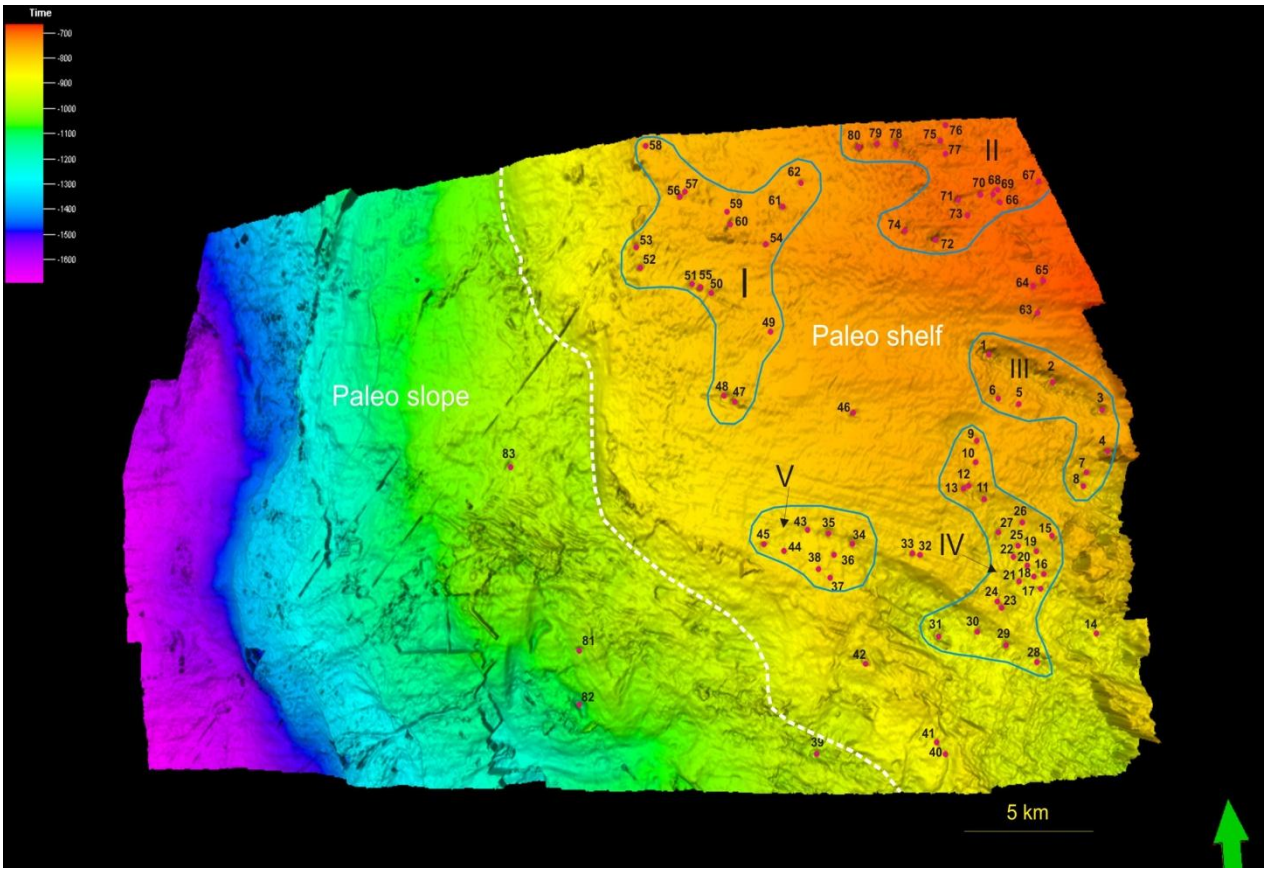

Fig. 2-10. URU interpreted paleo surface shows pockmarks distributions; white dashed line separates the paleo continental slope from paleoshelf; blue lines outline the areas (I-V) with high pockmark concentrations.

The parameters of some of the observed features are given in appendix 1. The parameters chosen for statistical analyses are: depth, length, width, shape (circular, elliptic or elongated), orientation and additional evidence for fluid migration (acoustic pipes, amplitude increasing, bright spots, reflector discontinuity). The length of the long axis varies from 85-1000 m and for the short axis from 60-500 m. The prevailing orientation of the features is SE-NW in the south and NE-SW in the northern part of the area. The average length of the long axis and short axis are 248,4 m and 161,98 m respectively. Thus, most of the features are elongated. A diagram (fig. 2-11) shows the

relation between the long axis and the short axis. Depressions that are lying above the trend line show a circular shape. The diagram indicates that small features (80-150 m for short axis) tend to be more circular than the large features (150-350 m for short axis).

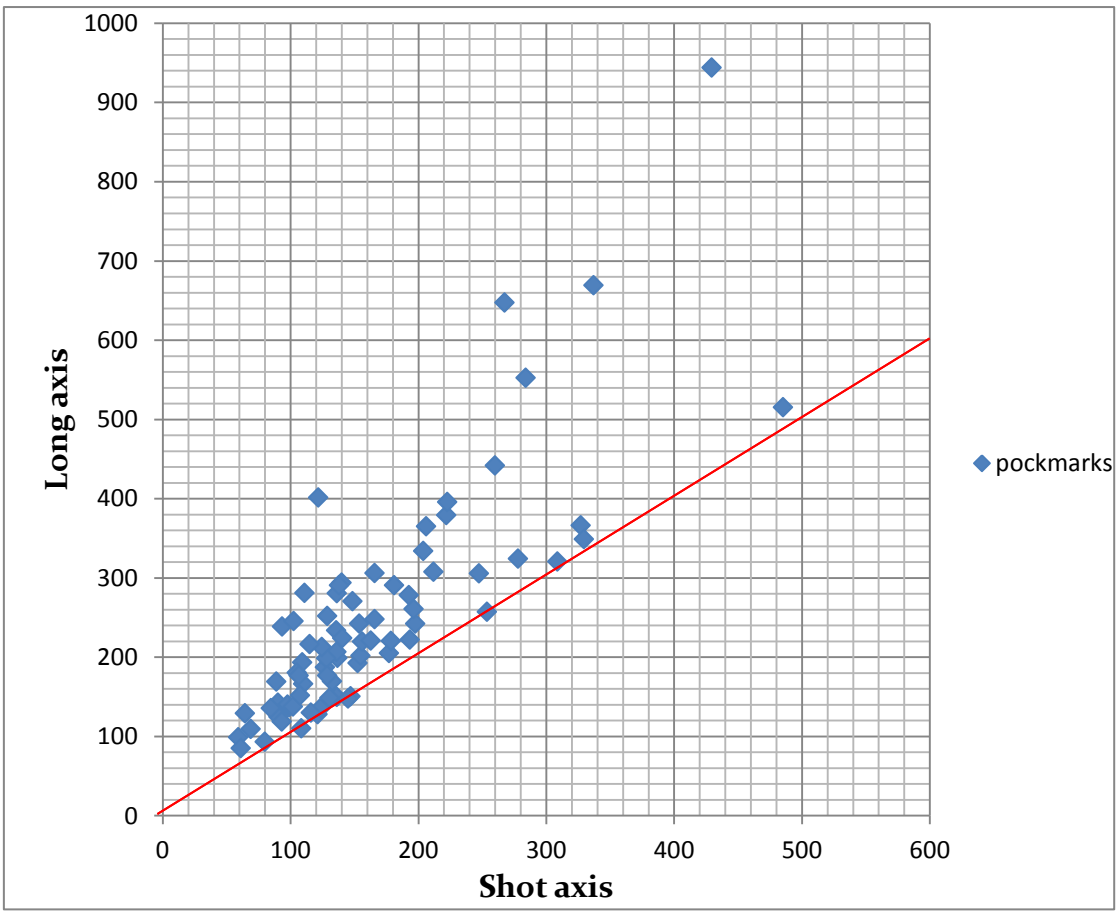

Fig. 2-11. Diagram shows relationship between short axis and long axis of depressions.

Fig. 2-12 shows the ratios of pockmark axis within each of the five areas of distribution (fig. 2-10). The largest features are located inside the area II, the smallest are concentrated in the area IV (100-250 for long axis). Area IV is characterized by pockmark shapes that are closer to circular. The smaller features with a long axis length from 80-200 m tend to be more circular than the large features with a long axis from 200-400 m.

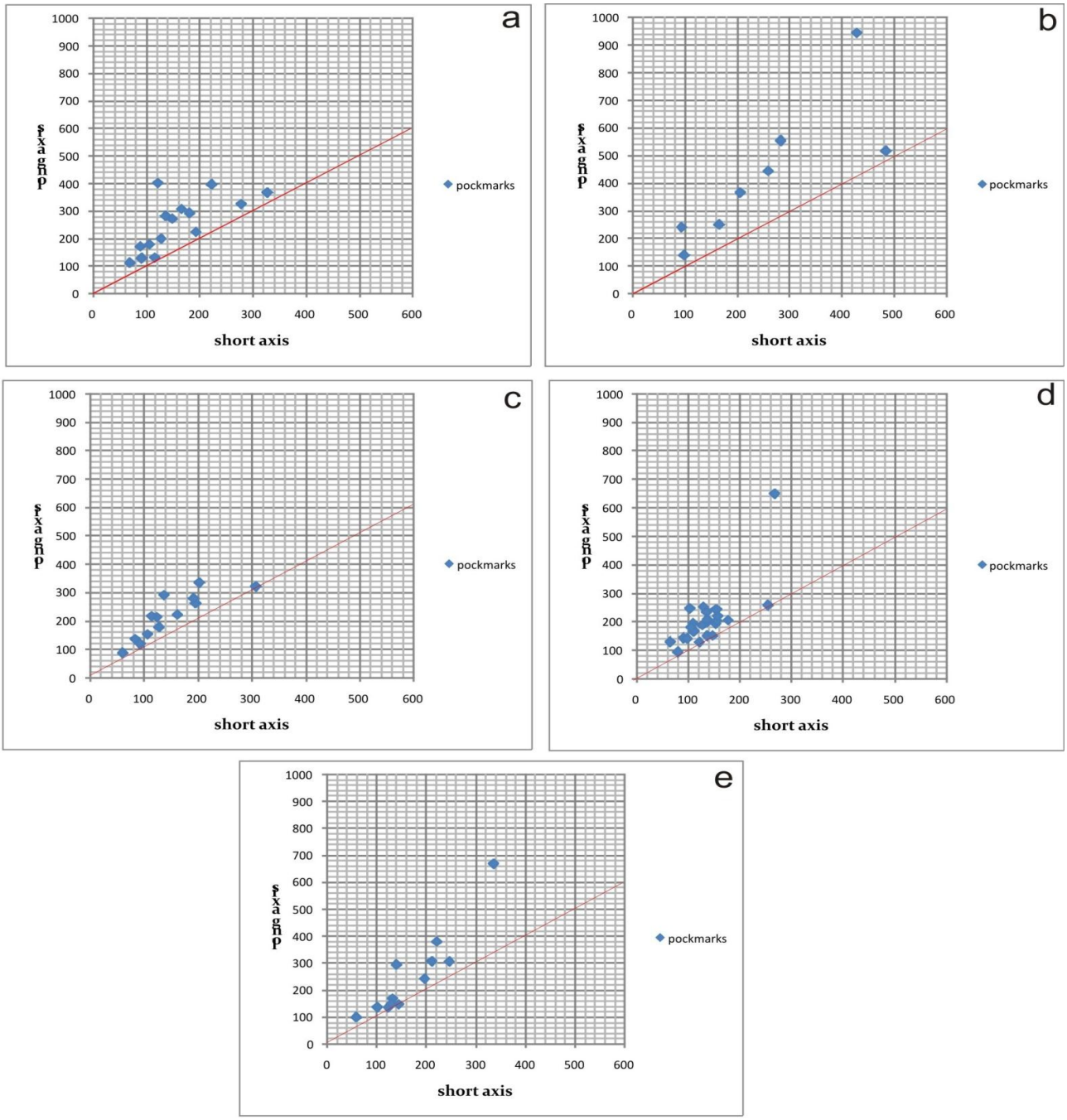

Fig. 2-12. Diagrams show long axis and short axis ratio for each of the five areas defined in the fig. 2-10; a. features in area I; b. features in area II; c. features in area III; d. features in area IV; e. features in area V.

Due to a lack of interval velocity information the depth of depressions were gathered in milliseconds and the average depth of depressions is ~ 5 ms TWT. Fig. 2-12(a) shows the relationship between pockmark areas and their depth of depressions. Areas were calculated according to the values of long and short axis. As the main shape of depressions are determined as elliptical, the formula for the depression areas are as follows:

A=πxL(la)xL(sa);

A = area of the depression;

π=3,14;

L(la)=length of long axes;

L(sa)=length of short axis.

The diagram does not identify strict connections between depression areas and depths. The average individual pockmark area ranges from 0,025 km² to 0,175 km². The depth of smaller depressions (with areas from $25x10^3$ m² to $50x10^3$ m²) varies between 1-6 ms TWT. The medium depth (areas values from $50x10^3$ m² to $175x10^3$ m²) varies between 9 ms TWT. The depression values from areas I, II and III spread chaotically across the diagram and do not indicate any defined relationship. However, fig. 2-13(b) which is based on average depth values found for each 25000 m² depression area, shows an increase of depth with an increase in depression area.

The URU subsurface contains features of various sizes, depth and shape and can be subdivided into several types:

- Small irregular depressions in the north-west of the paleoshelf (area I) without any clear fluid migration pathways;
- Depressions in the north-east of the URU subsurface which are connected with clear acoustic pipes (area II);
- Depressions inside the large ploughmark (area III);
- Circular or elongated NNE-SSW oriented depressions that are concentrate in the front zone of paleo troughs (area IV and III);
- Depressions in the south outside the glacier trough glacial trough (area V);
- Circular depressions connected with mega-scale glacial leniations (area V).

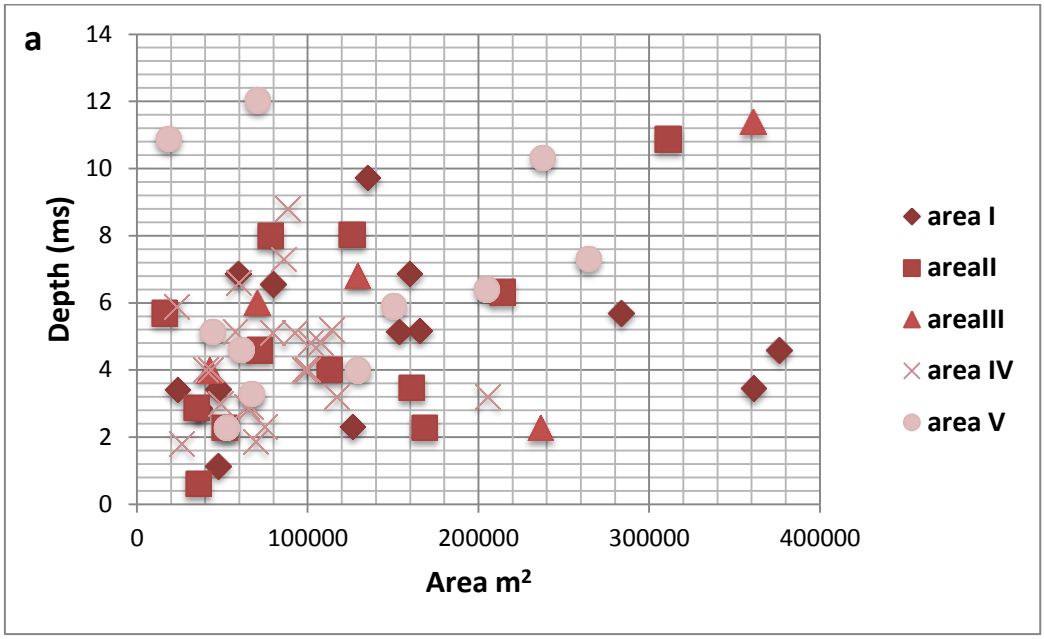

Fig. 2-13. The diagram shows the relationship between area, size and depth values;

Circular or elongated NNE-SSW oriented depressions that concentrate in the front of paleo troughs (area III and IV):

Depressions in the southern part of the 3D data cube concentrate in the front zone of paleo troughs and tend to spread along the north-eastern slope of the troughs. The lengths vary from 55-70 m to 330-550 m for the long axis. The small circular and large features are oriented in most cases NNE-SSW or NE-SW. The orientation of depressions does not correspond to the troughs axis or MSGL directions.

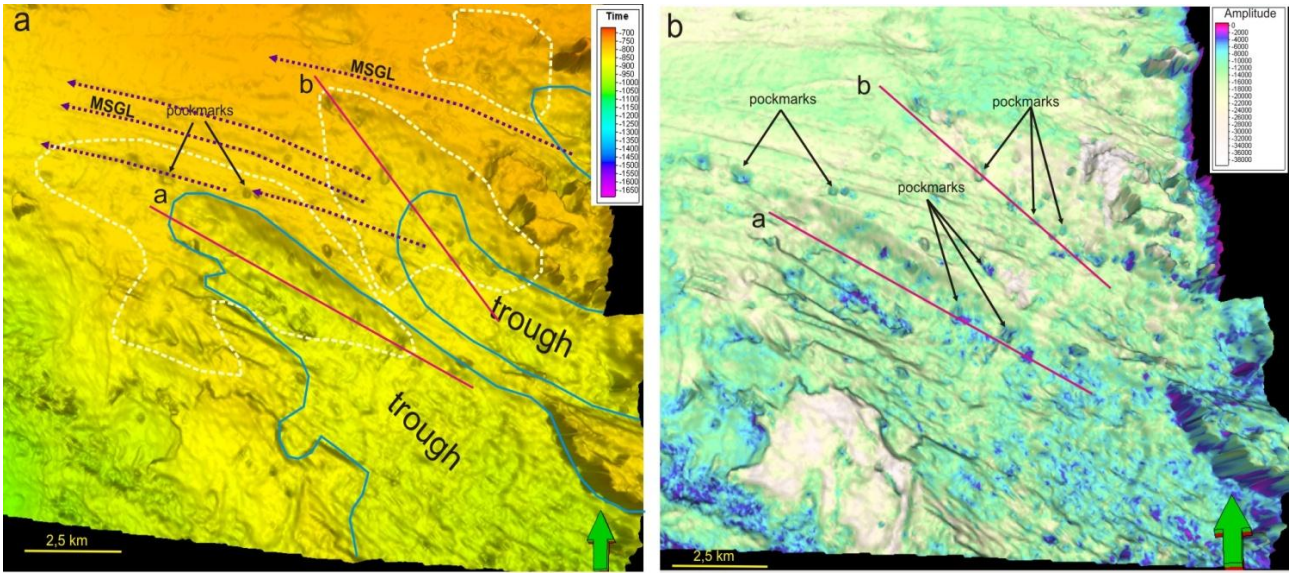

Fig. 2-14. Troughs in the south-eastern part of ELo001 3D block where red lines mark location of seismic lines shown in figure 2-15; a. 3D correlated surface area of URU horizon; b. minimum amplitude attribute map based on URU subsurface (offset -10; search window 50).

The depressions that are located in the bottom of the troughs show truncated toplap layers towards the URU (fig. 2-15). In the seismic profiles they are characterized by steep oblique slopes which continue in the direction of dipping layers (fig. 2-15). Short and high amplitude anomalies occur above the depressions. Some of the depressions are correlated with bH reflector pull-down (above the URU) (fig. 2-15a, 2-15b).

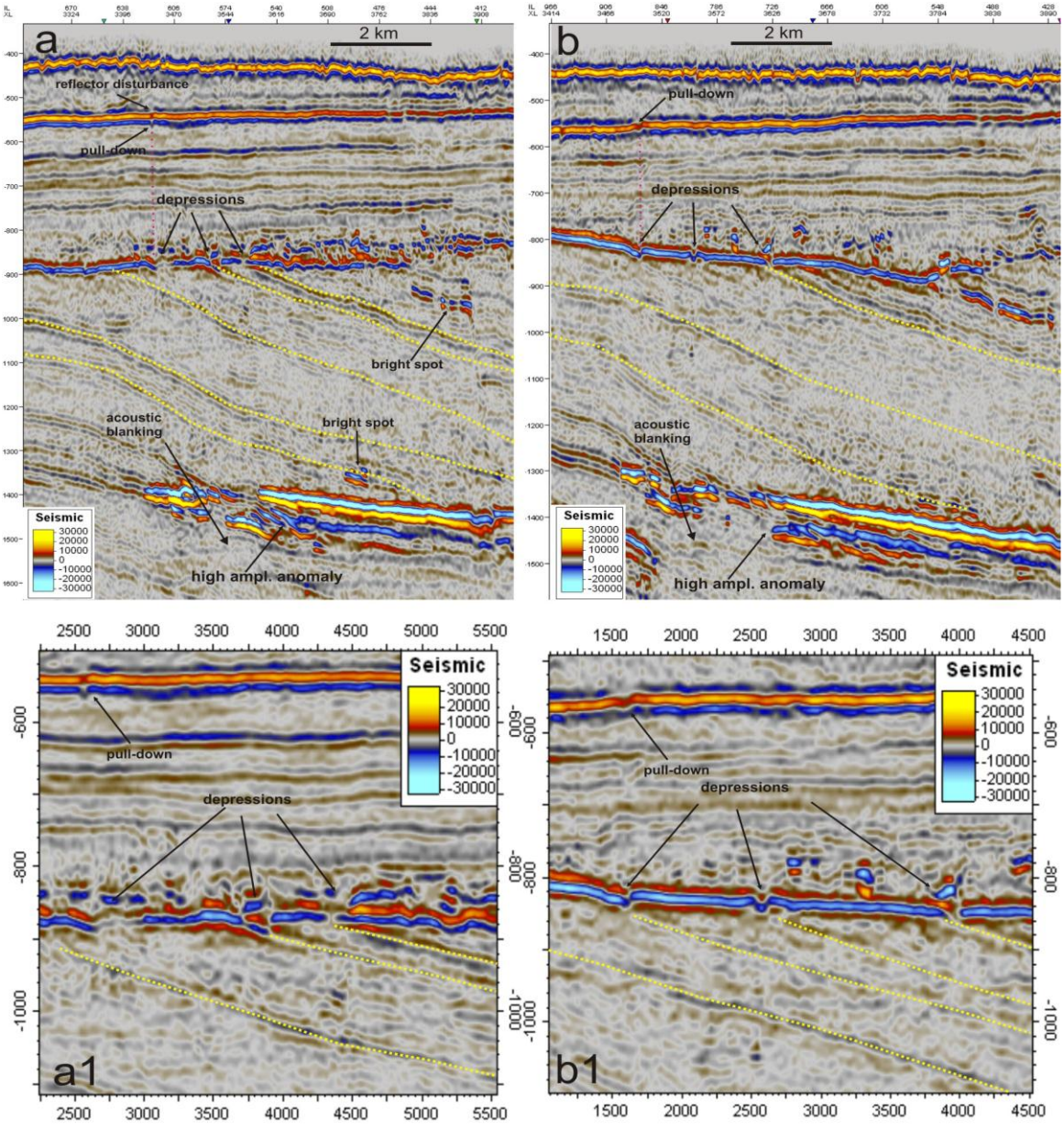

Fig. 2-15. Seismic profiles across the depressions. The location of the arbitrary lines is shown in fig. 2-15a and b.; the yellow dotted lines mark the truncated dipping layers. Fig. 2-15a1 and 2-15b1 are zoomed parts of seismic profiles a and b.

As shown in figure 2-15a and b some of the truncated layers are connected with high amplitude anomalies and depressions. The seismic anomalies may indicate the presence of gas in the sediments. Fluids may seep along strata boundaries of the

truncated Tertiary sediments and through the URU upwards. This is evidenced by the presence of small bright spots located directly above the depressions at the depth of 850 ms TWT (fig. 2-15a and 2-15a1); and at the depth of 750-800 ms TWT (fig. 2-15b and 2-15b1).

Circular or elongated depressions with evidence for fluid flow migration towards the shallower horizons, located in the southern part of paleo slope and in the north-east (area II and area V):

18 depressions and three mounds are situated in the URU subsurface and are followed by acoustic pipes that start from the Tertiary sediments towards bH reflector (fig. 2-16c and 2-16d). There are two zones where the features concentrate: one is located in the front zone of the southernmost trough (area V) and the other one in the north-eastern part of the paleo shelf (area II) (fig. 2-10).

Depressions in the southern area are dominantly circular or subcircular oriented E-W or NNE-SWW (fig. 2-16, 2-17). The area consists of two large circular depressions (N34 and 35) which are seated in the bottom of mega-scale glacial lineations (fig. 2-16a). The depression N34 is 379 m long and 222 m wide. The length axis of the depression N 35 is 307 m long and the cross axis is 211 m. The features are oriented E-W and are 5-6,5 ms TWT in depth. The remaining six depressions inside the glacial lineation area are quite shallow, i.e. 3-3,5 ms TWT in depth. The length of the long axis varies between 130-250 m and for the short axis between approx. 120-200 m. Acoustic pipes that connect to the depressions start at 1300 ms TWT and extend towards the high amplitude anomaly on the bH reflector (fig. 2-16 c. and d.).

The north-eastern area consists of nine depressions and two mounds (fig. 2-17 a). The depressions vary in size and depth. The most significant features are three deep depressions located at the end of iceberg ploughmarks (fig. 2-17a). They are approx. 6,5-10 ms TWT in depth and oriented NE-SW. The long axis varies from 260-350 m and the short axis is approx. 200 m. These three depressions are distinguished from the other features inside the lineations by their clear shape and larger size. The other features are more shallow and characterized by an unclear shape. They show a 10-150 m long axis and are only 0,5-4 ms TWT deep with an NE-SW orientation.

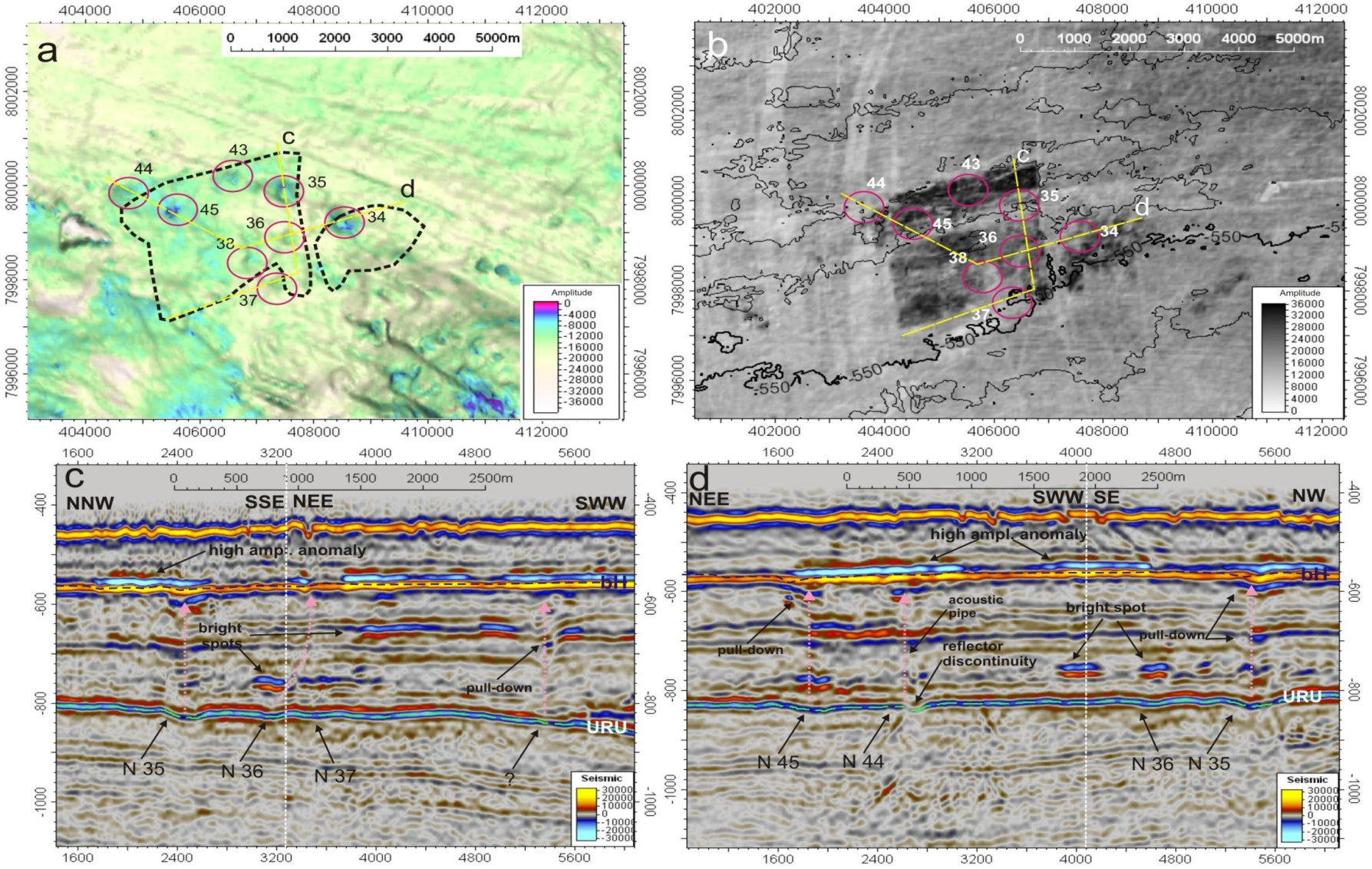

Fig. 2-16. a. Minimum seismic amplitude attribute map (search window 50 offset 0) of URU interpreted surface 3D window; b. maximum amplitude map (search window 50 offset 0) of bH interpreted surface in 2D window; c. and d. arbitrary seismic lines generated across the depressions on URU.

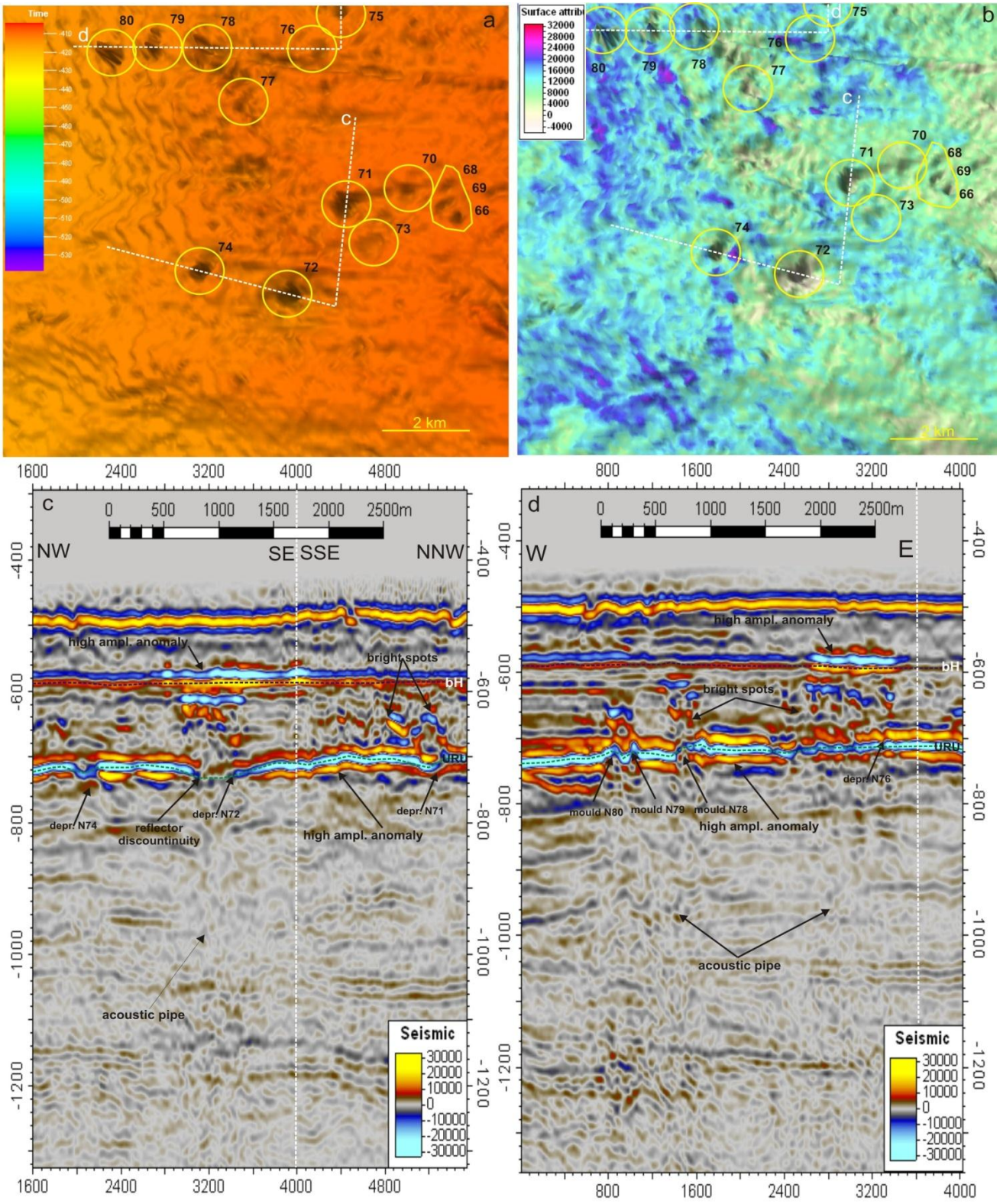

Fig. 2-17. Depressions and mounds in the northern part of the URU sub surface; a. 3D surface; b. average peak seismic attribute map (offset 0, search window 50); white dashed lines shows the location of seismic arbitrary lines in the fig. 2-17c and 2-17d.

In the seismic amplitude maps the features appear on the high amplitude anomaly at URU (fig. 2-17b,c,d). The low amplitudes of the depressions correspond to the reflector discontinuity caused by acoustic pipes (fig. 2-17c. and d.). The top of acoustic pipes and

the depressions at URU are marked by bright spots at the depth interval between 650-580 ms TWT. Some depressions do not show any clear evidence for connectivity to an acoustic pipe, however they are also accompanied by a bright spots located 20-50 ms TWT above them (fig. 2-17d).

Circular depressions inside the MSGL

In the southern part of the paleo shelf two couples of circular and deep depressions occur (fig. 2-18). The depressions are located in the bottom of mega-scale glacial lineations. Two large depressions (N 35 and N34) are situated at the front of the glacial trough (figs 2-18 and 2-16).

Two smaller depressions (N33 and 32) are found at the northern side of the trough (fig. 2-18 e,f,g). The distance between two depressions is 25-30 m. They are characterized by a clear rim and circular shape. The depression N 33 is approx. 200 m in diameter while depression N 32 is smaller and 110 m in diameter. The depth is 7,3 ms and 5 ms TWT respectively.

The seismic profile shows depressions N35 and 34 connected to acoustic pipes that continue to the bH horizon (fig. 2-16 c,d, 2-18b). The depressions N33 and N 32 do not indicate any acoustic evidence for fluid migration (fig. 2-18 e.f.g). However, evidence exists that they are related to normal faults in Tertiary sediments caused by the anticline structure in underlying rocks (fig. 2-18 b). In addition, the seismic section shows an infill of depressions after their development (fig. 2-18e).

Depressions connected with iceberg ploughmarks

A large groove occurs at the eastern part of the paleo shelf (fig. 2-19a). The feature is 6,2 km long, 550 m wide and 10 m deep. The SE-NW orientation coincides with the direction of the glacial troughs in the south-east. The feature resembles the morphology of an iceberg ploughmark. Three wide depressions (N1, 2, 3) occur at its base. The largest depression (N1) is 943,8 m long and 429,5 m wide and it is located in front of the ploughmark (fig. 2-19a). In the seismic profile, the depression is characterized by a seismic amplitude polarity change. It marks the sediment infill which may represent lower density and/or higher porosity than the adjacent strata.

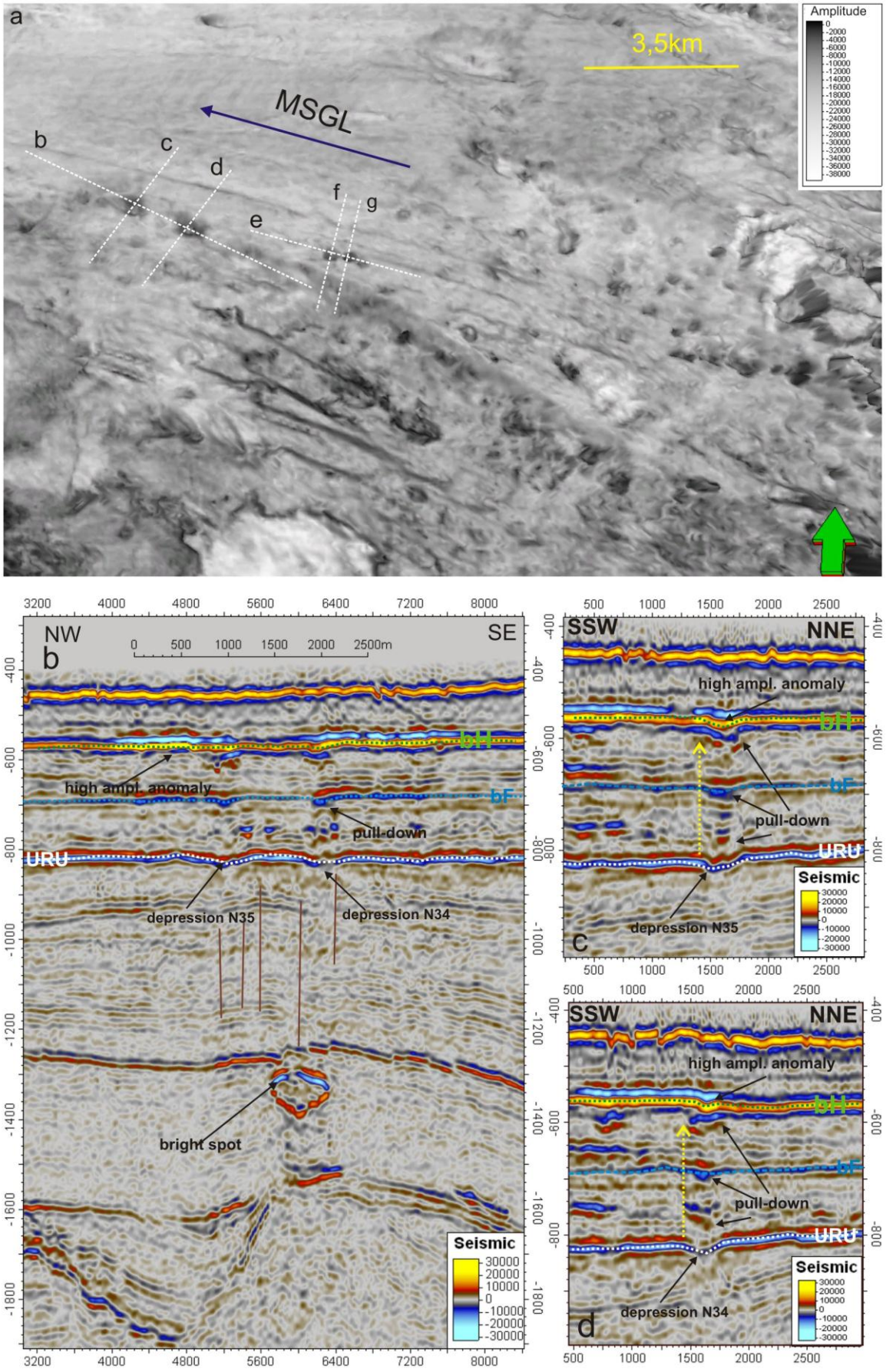
a
3,5km
MSGL
b
c
d
e
f
g
Amplitude
0
-2000
-4000
-6000
-8000
-10000
-12000
-14000
-16000
-18000
-20000
-22000
-24000
-26000
-28000
-30000
-32000
-34000
-36000
-38000
NW
SE
0 500 1000 1500 2000 2500m
bH
bF
URU
high ampl. anomaly
pull-down
depression N35
depression N34
bright spot
Seismic
30000
20000
10000
0
-10000
-20000
-30000
SSW
NNE
c
d

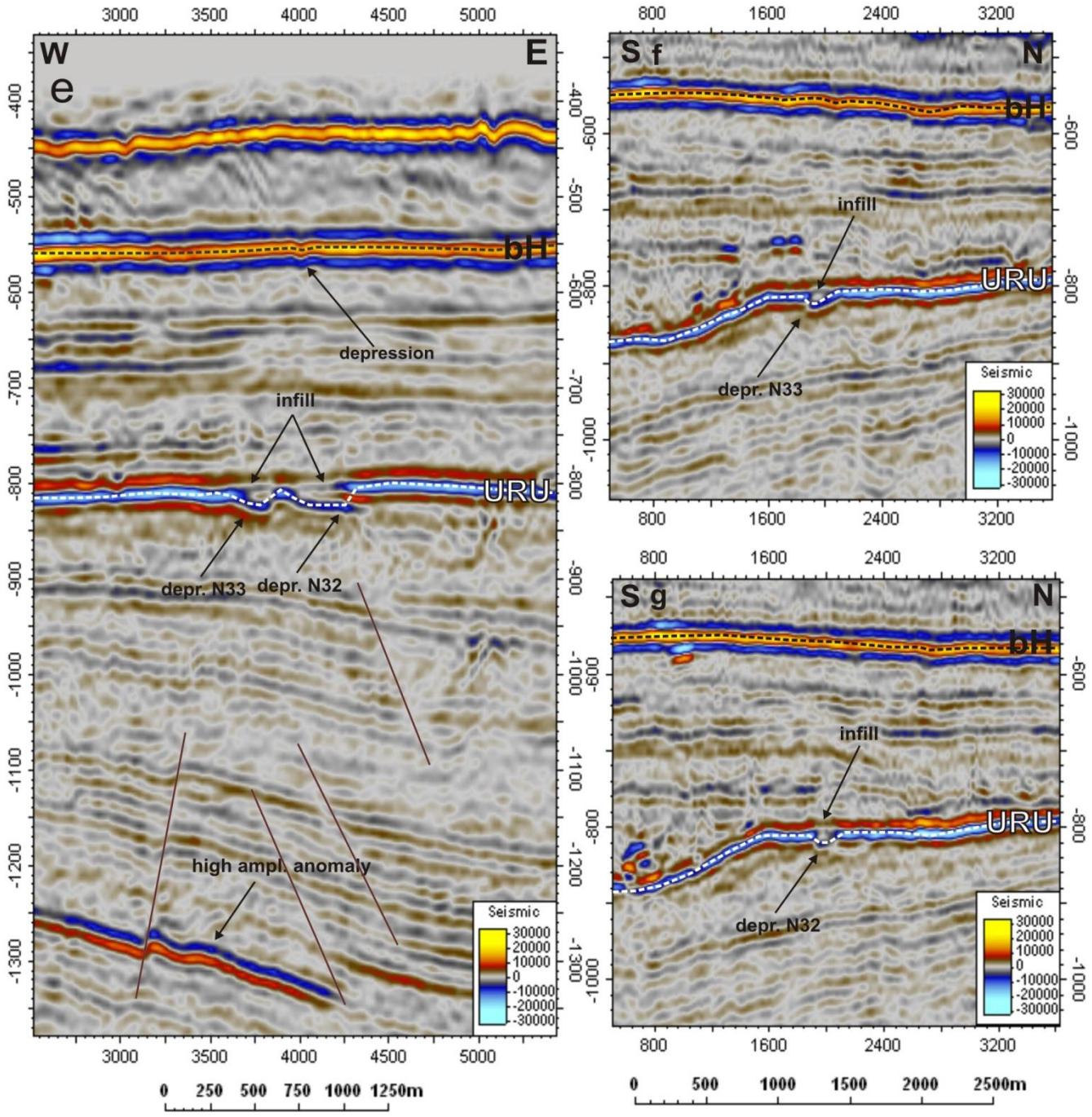

Fig. 2-18. Circular depressions; a. minimum seismic amplitude attribute map (offset 0, volume window 50); white lines show the location of seismic sections in figs. 2-18 b, c, d, e, f, g; b. seismic section show the depression N34 and 35; c. seismic section shows the depression N35 ; d. seismic section show the depressions N34; e. seismic section show the depressions N33 and N32; f. seismic section shows the depression N33; g. seismic section shows the depression N 32.

The second depression is located in the center of the iceberg ploughmark (fig. 2-19a). The depression is circular, 500 m in diameter and 8,58 ms TWT deep. The feature is composed of three smaller depressions. In the seismic profile it is followed by a polarity change at the URU reflector. The depression N3 is situated in the beginning of the ploughmark; it is 552,7 m long and 284,1 m wide. All features are accompanied by a disturbance of reflections due to chaotic reflections that can be followed vertically from

1500 ms to 850 ms TWT (fig. 2-19b). The chaotic reflection could be interpreted as acoustic pipe or artifact (linear noise).

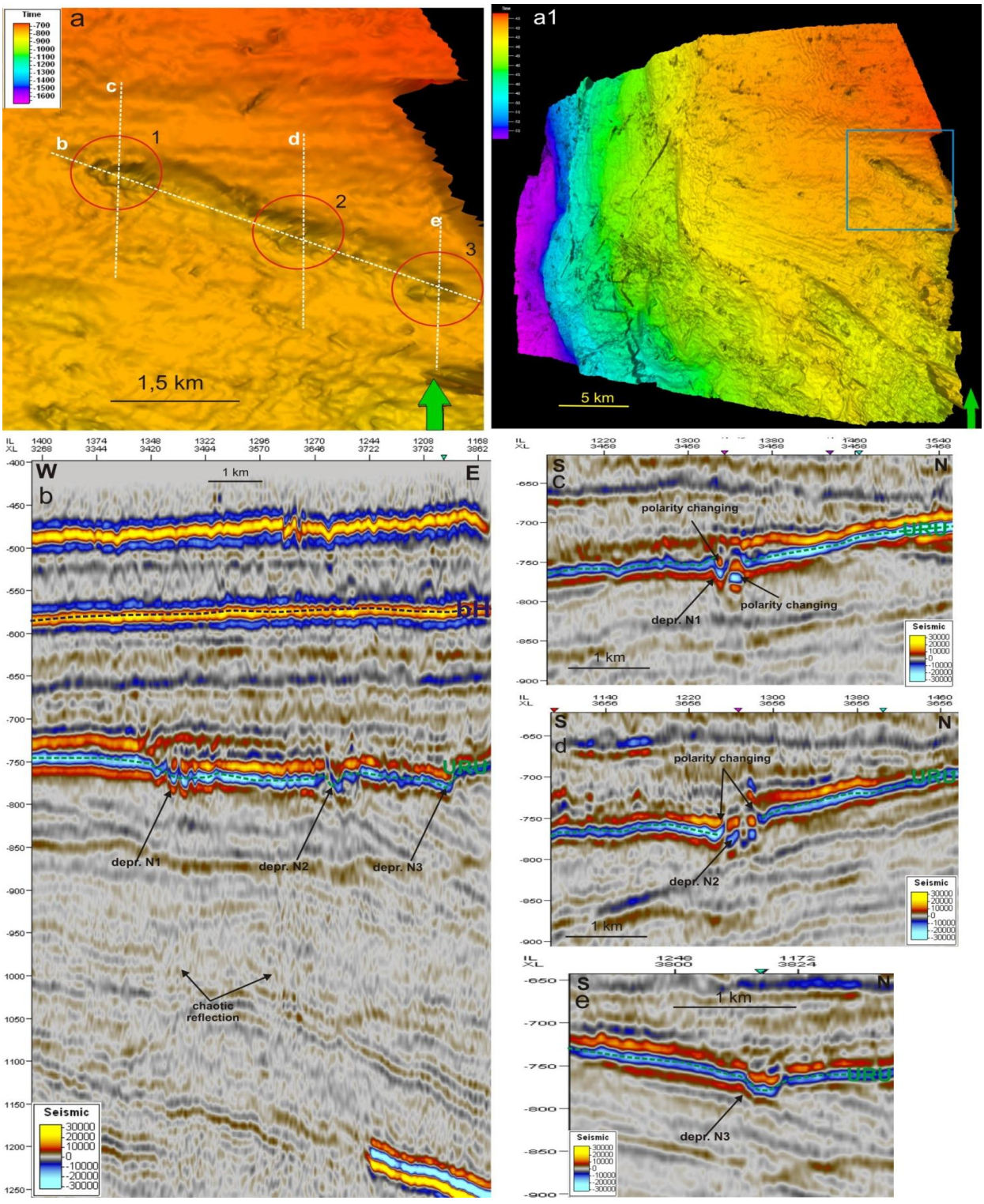

Fig. 2-19. Depressions in the bottom of iceberg ploughmark; a. Part of 3D surface (URU horizon) shows a ploughmark; white lines mark the location of seismic sections; b. seismic section across the ploughmark bottom; c. seismic section shows the depression N1 ; d. seismic section shows the depression 2; e. seismic section shows the depression N3.

2.1.6. Acoustic pipes associated with URU depressions

13 depressions and 3 mounds in the Upper Regional Unconformity reflector are associated with clear acoustic pipes (table 6).

N	expression	extension	Long axis	Short axis
1.	Depr. N 35 URU and high ampl. anomaly on bH	URU-bH	438,5 m	337,4 m
2.	Depr. N34 URU and high ampl. anomaly on bH	URU-bH	369,46 m	563,48 m
3.	Depr. N45 URU and high ampl. anomaly on bH	URU - bH	208,47 m	208,47 m
4.	Depr. N44 URU and high ampl. anomaly on bH	URU - bH	283.18 m	270,8 m
5.	Depr. N 36 URU	URU - bF	244,48 m	205,57 m
6.	Depr. N38 URU	URU-bH	283,18 m	193,1 m
7.	Depr. N4 URU (bright spot)	Top Cretaceous - URU	708,377 m	463,17 m
8.	Depr. N72 URU and high ampl. anomaly on bH	Top Cretaceous - bH	643,98 m	417,96 m
9.	Depr. N71 URU	Top Cretaceous - bF	370,49 m	224,98 m
10.	Mould N 78 URU and high ampl. anomaly on bH	URU-bH	193,0 m	258,99 m
11.	Mould N79 URU	Top Cretaceous - bF	322,0 m	226,0 m
12.	Mould N80 URU	Top Cretaceous - bF	353,98 m	224,98 m
13.	Depr. N 73 URU	URU-bH	320.95 m	208,46 m
14.	Depr. N70 URU	URU – 650 ms TWT	370,49 m	193,0 m
15.	Depr. N68,69,66	URU-bH	437,57 m	412,15 m
16.	Depr. N75 URU	URU – 650 ms TWT	373,17 m	257,59 m

Table 6: Parameters of pipes related to depressions at URU.

Depressions with acoustic pipes are concentrated preliminary in the south of the paleo-shelf outside the glacial trough (fig. 2-16) and in the north-eastern part of the 3D block connected with the high amplitude anomaly on URU (fig. 2-17).

The first group of acoustic pipes (Nr. 1-6) corresponds to the depressions from area V. The acoustic distortion starts from URU and continue towards bF-bH reflectors. The bright spot between the depths 700-800 ms could be an indicator of fluid presence in the pore space of sediments (fig. 2-16 and 2-18).

The second group of the pipes (Nr. 8-16) are extended previously from top Cretaceous reflector or URU and stops on bH, bF or in between in the depth aprx. 650 ms TWT (fig. 2-17). Four pipes (8, 9, 11, 12) are more clear and start from the source rocks, while the rest of the pipes could be traced only from URU (fig. 2-16 and 2-17).

2.2. ST0309 (Nordkappbanken)

2.2.1. Depressions at the base of a meandering channel at the seabed

Eleven depressions (Fig. 2-20) were identified inside a channel which is located in the east of the ST0309 3D cube (fig. 2-21). The depressions concentrate in the meandering channel. Four depressions have been observed outside (fig. 2-21a).

Figure 2-20 shows an example of a clear depression outside the channel identified by using the instantaneous frequency surface attribute map for the seafloor horizon. The depression is characterized by a low frequency area caused by a bright spot. The bright spot is clearly obvious at 430-450 ms TWT and very close to the seafloor reflector (fig. 2-20c,d). The bright spot is characterized by a polarity reversal, amplitude increase and scattering of frequency. Such geophysical evidence might be caused by fluids accumulating beneath the depression (Andreassen, 2007b).

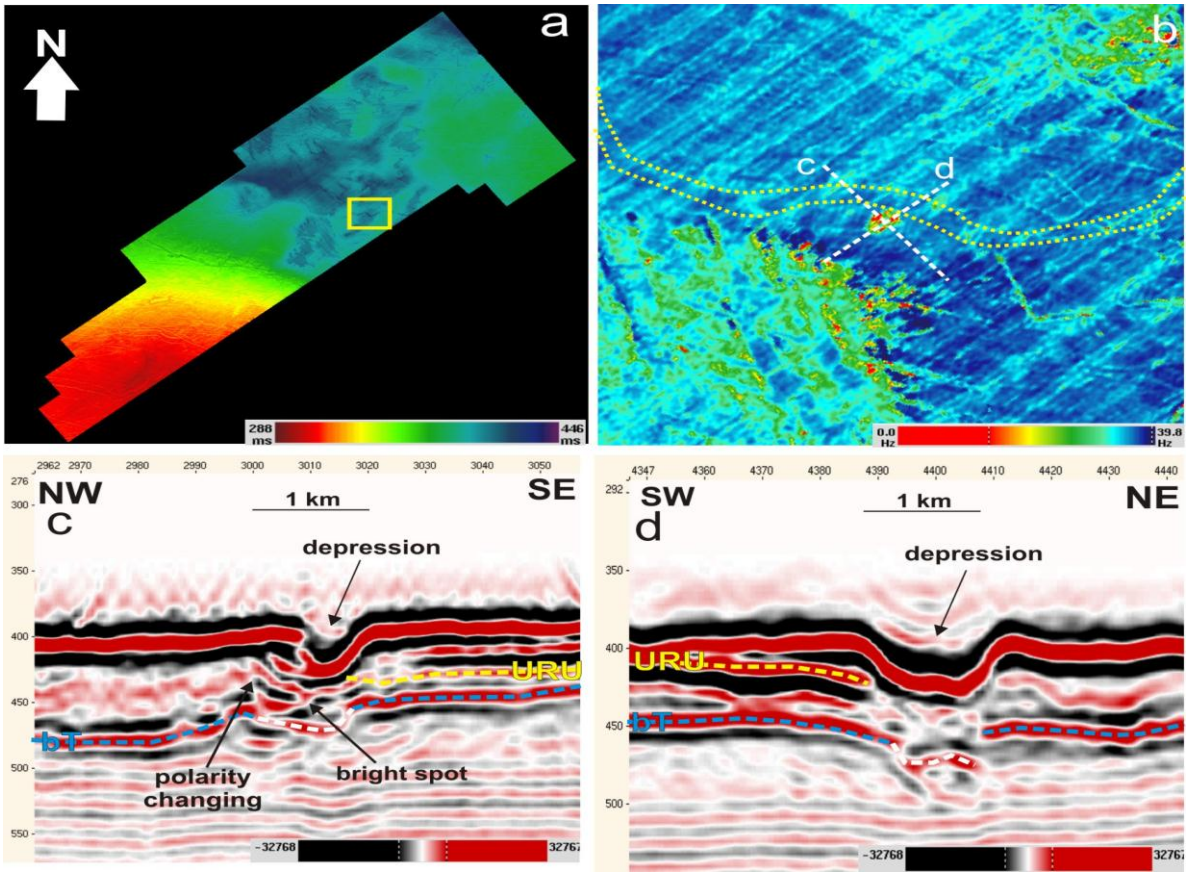

Fig. 2-20. The depression outside the channel on 2D bathymetry map; a. Position of the depression on the seafloor; yellow square outlines the zoomed part of frequency map shown in fig. b; b. zoomed frequency map where the depression is associated with a low frequency area; white lines indicate the position of seismic lines in fig. c and d; the yellow dashed line reconstruct the meandering channel bottom; c. seismic line across the depression; yellow line follow the URU, blue dashed line marks the bT reflector; white dashed line indicates the erosion on bT d. seismic line across the depression; yellow dashed line shows URU; blue dashed line indicates bT reflector; white line shows erosion on bT.

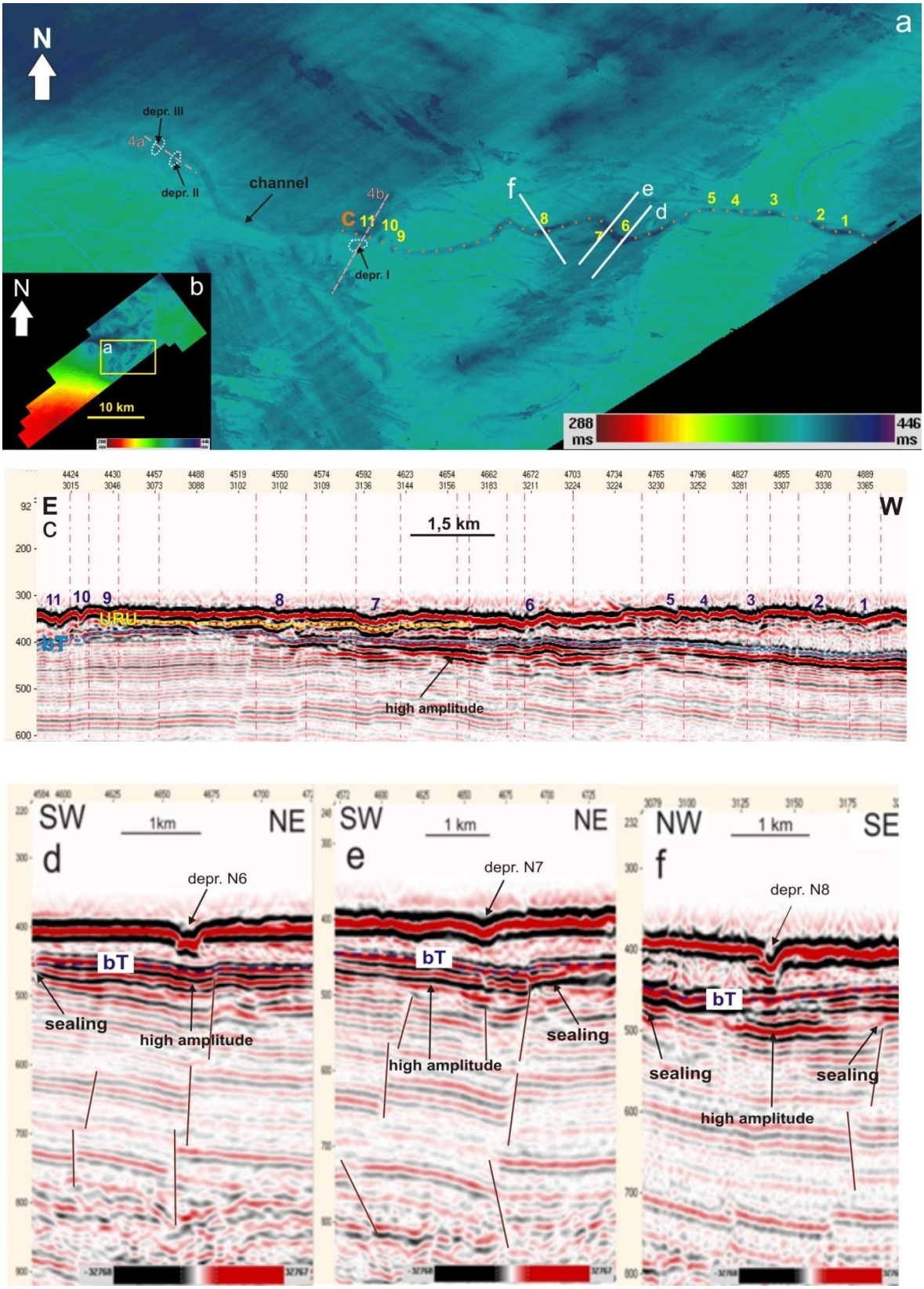

Fig. 2-21. 2D bathymetry map illustrates depressions inside the channel; a. zoomed part of the bathymetry map, the orange dotted line marks the channel and the location of the seismic lines, the numbers show the location of eleven depressions inside the channel bottom; c. seismic section shows the depressions, blue dashed line marks URU, velvet dashed line marks base Tertiary (bT) reflector, yellow line outlines bright spot area close to the Tertiary sediments.; d. seismic line across the channel shows the depression N6; e. seismic line across the channel show the depression N7; f. seismic line across the channel shows the depression N8.

An elongated depression shows a diameter of approx. 270 m for the long axis and 145 m for the short axis. The feature is SW-NE oriented. The depression is characterized by a clear rim and it is U-shaped in the seismic profile (fig. 2-20c). The depression appears to be not filled by sediments. The observation may suggest a more recent seafloor expulsion and seeping of shallow fluids, i.e. during postglacial time.

Figure 2-21c provides clear evidence for a connection between seismic anomalies and normal faults. The anomalies were probably formed during the rising of fluids. The channel is located between two salt diapirs,which host environments that make fluid flow processes very likely (fig. 2-22).

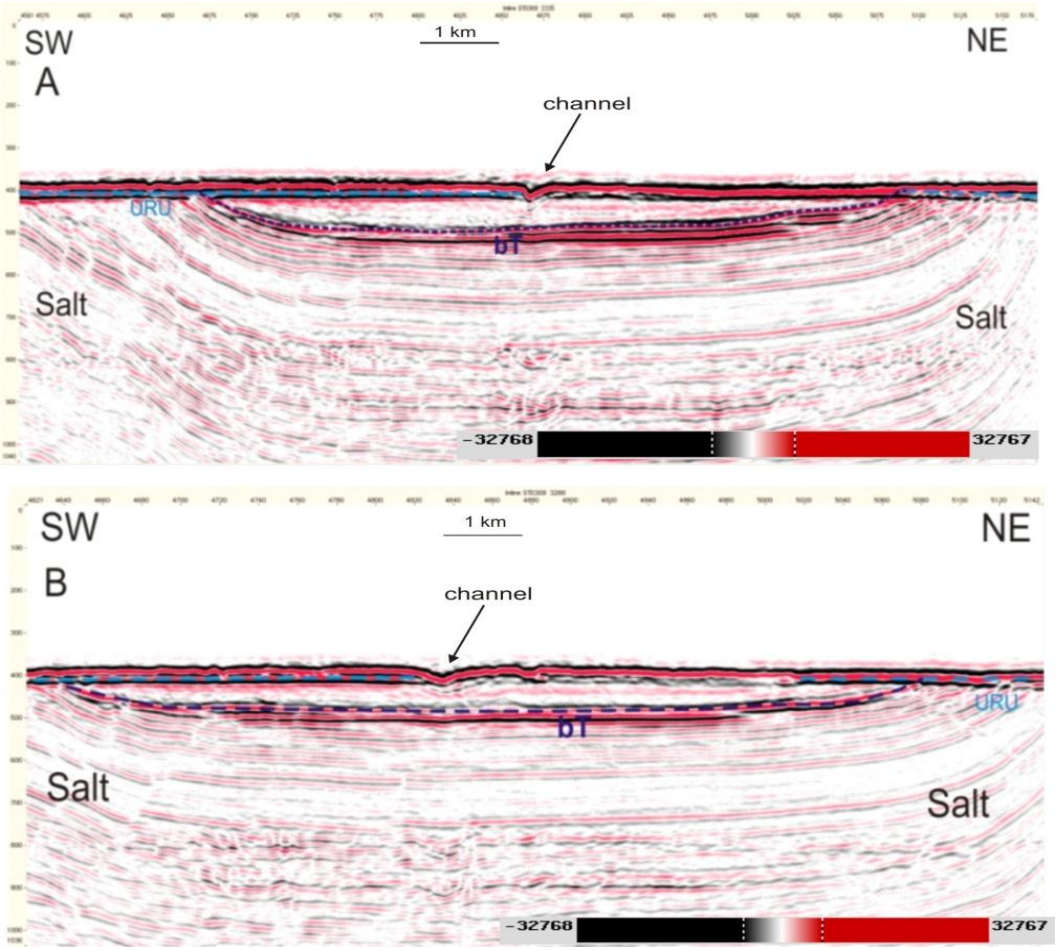

Fig. 2-22. Random seismic profiles across the channel in the seafloor illustrate the position the of it in connection to salt diapirs.

The amplitude anomalies (fig. 2-21 c, d, e, f) are not characterized by a polarity change. The observation may suggests the existence of only minor quantities of fluids in pore volumes and/or amplitude increases caused by less lithified sediments between two salt diapirs *(Posamentier H.W., 2003)*..

The seismic sections across the channel indicate the sealing of the bright spot towards the bT reflector indicating, that the fluids are possibly trapped near the top of the deposits (fig. 2-21 d, e, f).

Figures 2-21d, e, f illustrate some cross sections along the depressions inside the channel. The depression N7 is similar to depressions outside the valley (see fig. 2-20). It is also deep (20 ms TWT) and U-shaped in the seismic profile showing steep slopes. Depression N8 is marked a by high amplitude that is located very close to the seafloor at the depth 430-440 TWT (fig. 2-21 f).

The depression Nr. I is located outside the channel and N11 inside the channel (fig. 2-23a). The seismic profiles across these two depressions (fig. 2-23b) indicate that the features are associated with erosion of bT reflector (fig. 2-23b). The depressions Nr. II and III outside the channel are also related to the concave shape of the bT reflector that could be interpreted as an erosional feature (fig. 2-23a).

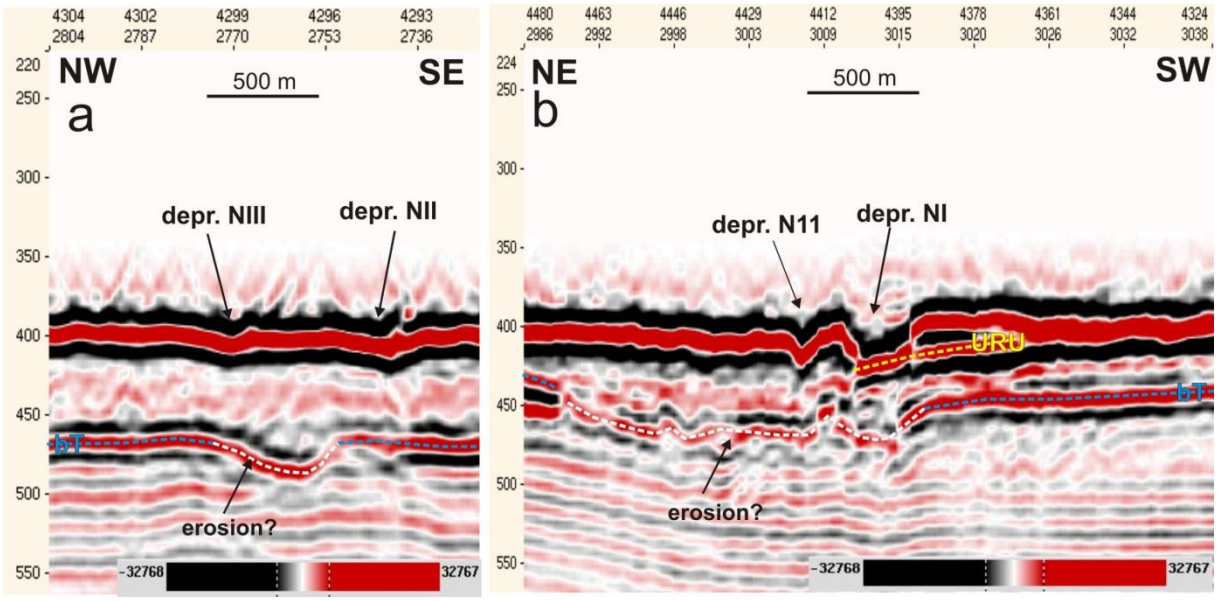

Fig. 2-23. Seismic profiles through the depressions located outside the meandering channel, the position of the seismic sections is shown in fig. 2-21a.

The correlation map made for the bT horizon interpreted surface shows the elongated furrow exactly under the depression Nr.I and depression Nr.11 (fig. 2-24). The feature is aprox. 25 ms deep, 1,3 km long and 200-400 m wide. The erosion groove is SW-NE oriented. The correlation map of the area contains the lineament structure that partly

repeats the configuration of the channel in the seafloor (fig. 2-24a). The seismic profiles across the feature show the displacement in the bT (fig. 2-24b and 2-24c). The displacement could be caused by a fault that was initiated by salt diapir. However, the feature is bending and not straight and that is not typical for faults.

A similar structure appears 1,1 km to the north (fig. 2-24a) and it is divided into two segments. The seismic profiles across the feature indicate the concave of the bT reflector that could be the result of erosion. The structure could be defined as the second paleochannel which is not preserved in the seafloor.

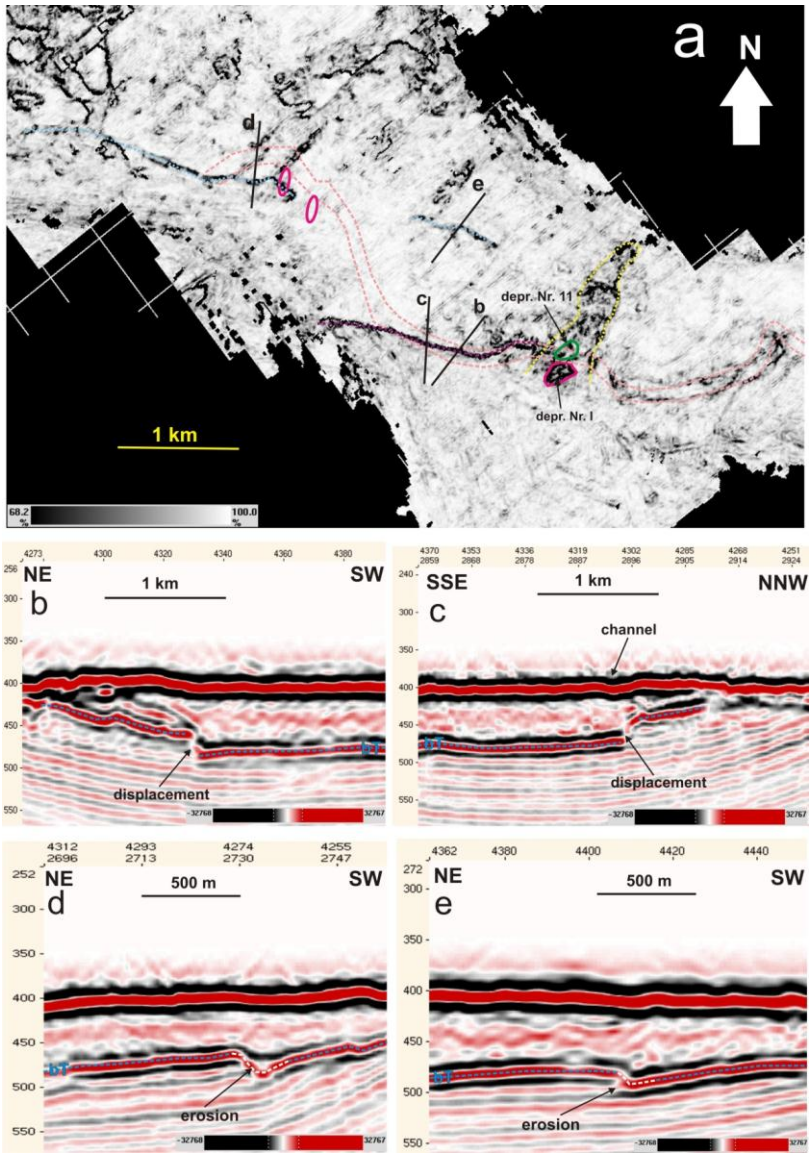

Fig. 2-24 a. Correlation map created for the bT reflector; the pink ovals mark the position of depressions in the seafloor outside the channel; the green oval shows the location of depression N11 inside the channel bottom; the yellow dashed line outlines the edges of erosion furrow; the pink dotted lines mark the boundaries of the recent channel in the seafloor; the light-blue dotted line follow the possible paleochannels bottoms on the bT interpreted horizon; black lines show the position of seismic lines; b.c.d.e. seismic profiles across the possible paleochannel on bT subsurface.

2.2.2. Evidence for paleo-seabed fluid flow at URU

URU shows a flattened and undisturbed reflector in the northeastern part of ST0309 3D (fig. 2-25). In contrast, disturbed and interrupted reflections exist in the north-eastern part of the 3D cube (fig. 2-25 to 2-27). The large channel bifurcation close to the URU subsurface does not show any evidence for potential fluid flow release features or seismic bright spots (fig. 2-25).

N1 and N6 are expressed as depression on the URU paleo surface (Figure 2-26c,d). Eleven depressions or reflector disturbances were identified on URU using seismic attribute maps generated for the interpreted surface (Fig. 2-25 and Figs.2-26 and 2-27).

The depressions and reflector discontinuities on URU occur outside the location of salt diapirs. The reflector discontinuities in the northern part of the 3D survey are spread around the southernmost diapir at the distance of 1,5-3 km away from its top.

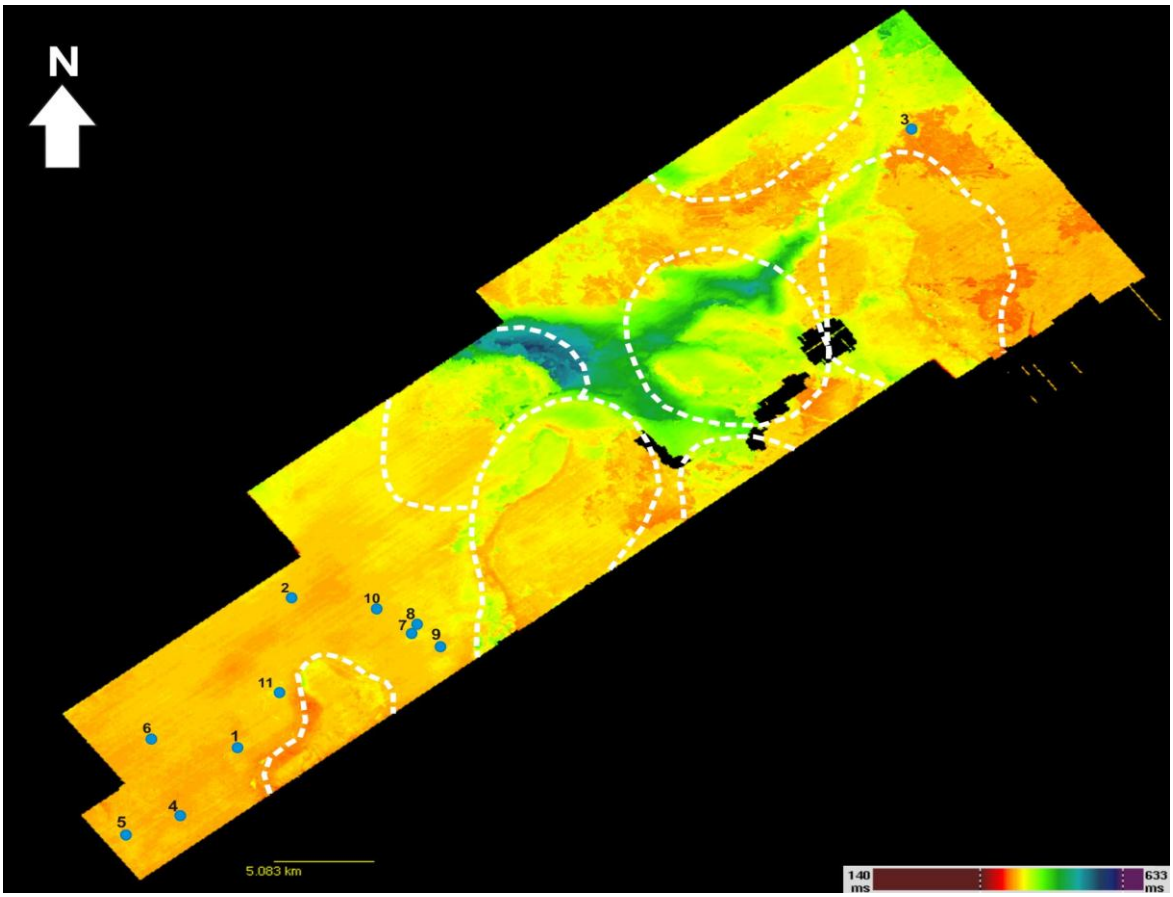

Fig.2-25. URU (R1) interpreted subsurface in IMAIN-Grid window (Charisma software); blue dotes mark the position of potential fluid-flow expressions at the URU paleo surface; white dashed lines outlines locations of salt diapers.

N	Long axis	Short axis	orientation	Evidence of fluid expressions
1.	270,4 m	110,6 m	N-S	The satellite depressions are associated with faults
2.	400,2 m	140 m	NE-SW	URU reflector discontinuity, pull-up effect of URU reflector
3.	362,7 m	173,4 m	NNW-SEE	URU reflector discontinuity, pull-up effect of the deeper reflectors
4.	314,1 m	113,4 m	NE-SW	URU reflector discontinuity
5.	136,4 m	116,2 m	NW-SE	URU reflector discontinuity
6.	157,1 m	81,9 m	E-W	URU reflector discontinuity, pull-down effect
7.	165 m	92,79 m	NW-SE	URU reflector discontinuity, pull-down effect
8.	143,9 m	114,7 m	NE-SW	URU reflector discontinuity, pull-down effect
9.	86,25 m	44,48 m	NE-SW	URU reflector discontinuity, pull-down effect
10.	129,8 m	114,7 m	NWW-SEE	URU reflector discontinuity, pull-down effect
11.	179,4 m	157,8 m	NNW-SSE	URU reflector discontinuity, pull-down effect.

Table 7: Parameters of the observed potential fluid flow features.

Depression N1 (fig. 2-25 and table 7) is located 1,7 km away from a salt diapir that is located in the north-east of the study area. The long axis of the depression is aprox. 207 m and the short axis is aprx. 110 m. The feature is N-S oriented by its long axis and is 25-30 ms

TWT deep. In the seismic profile it shows a pull-down effect at the bT and URU reflector discontinuity (fig. 2-26), which could be caused by a shallow fault. Deeper horizons do not provide evidence for possible pathways for fluids migration. The large depression is surrounding by four smaller satellite depressions at the north-eastern side. The satellite depressions N1 and 2 could be correlated with a pull-down effect at the bT reflector. They are also connected to faults possibly related to a salt diapir. The satellite depressions N3 and 4 are associated with a high amplitude anomaly at the depth of 420-450 ms TWT (fig. 2-26d).

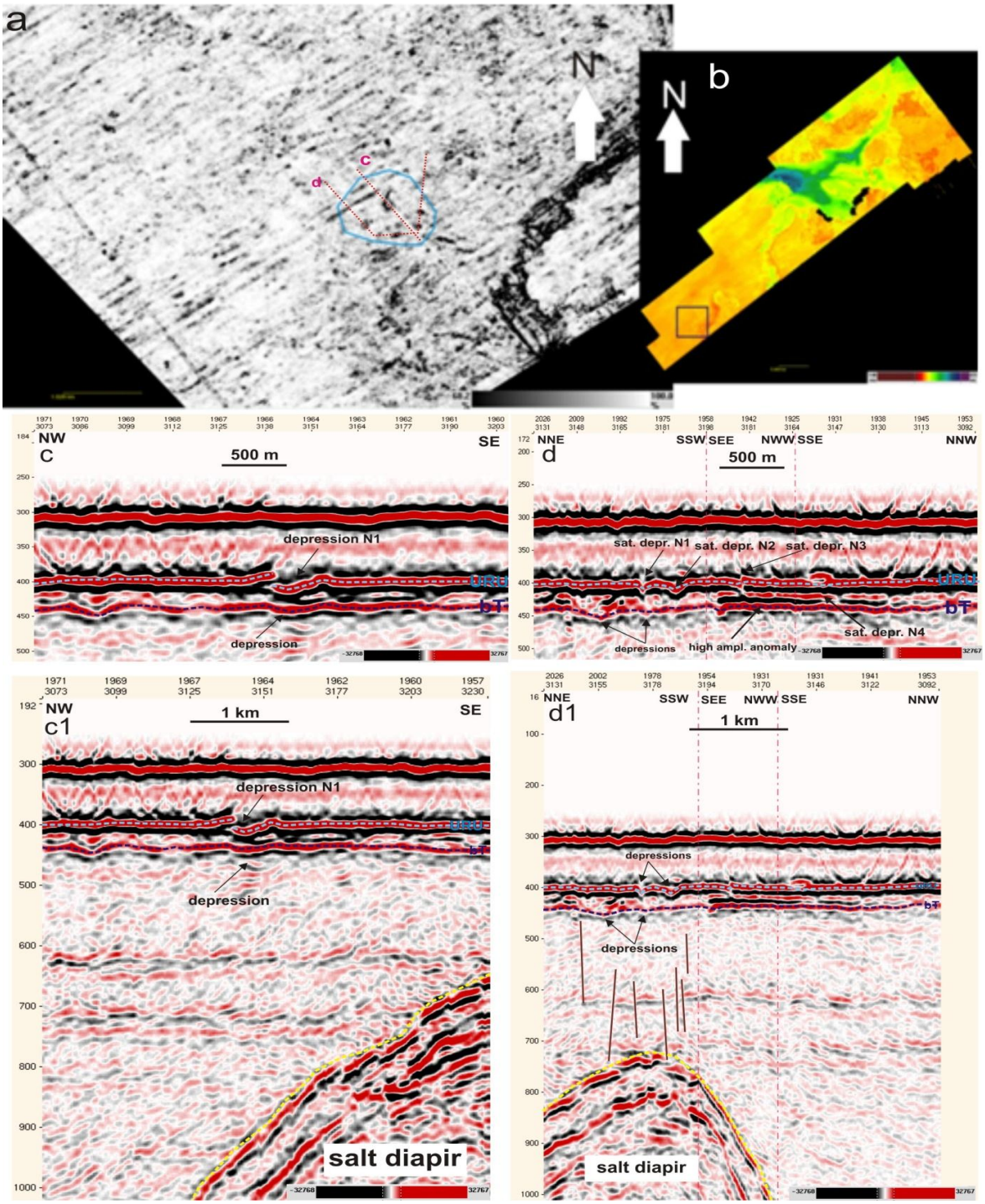

Fig. 2-26. a. Depression N1 on URU surrounded by satellite depressions ,blue line outlines the depression location area, red dotted lines show the location of seismic sections c, c1,d, d1. Seismic section illustrating the large depression and smaller depressions surrounding it.

The other potential fluid flow release expressions are expressed as URU reflector discontinuities and are not associated with any depression or anomaly at the seafloor (fig. 2-27).

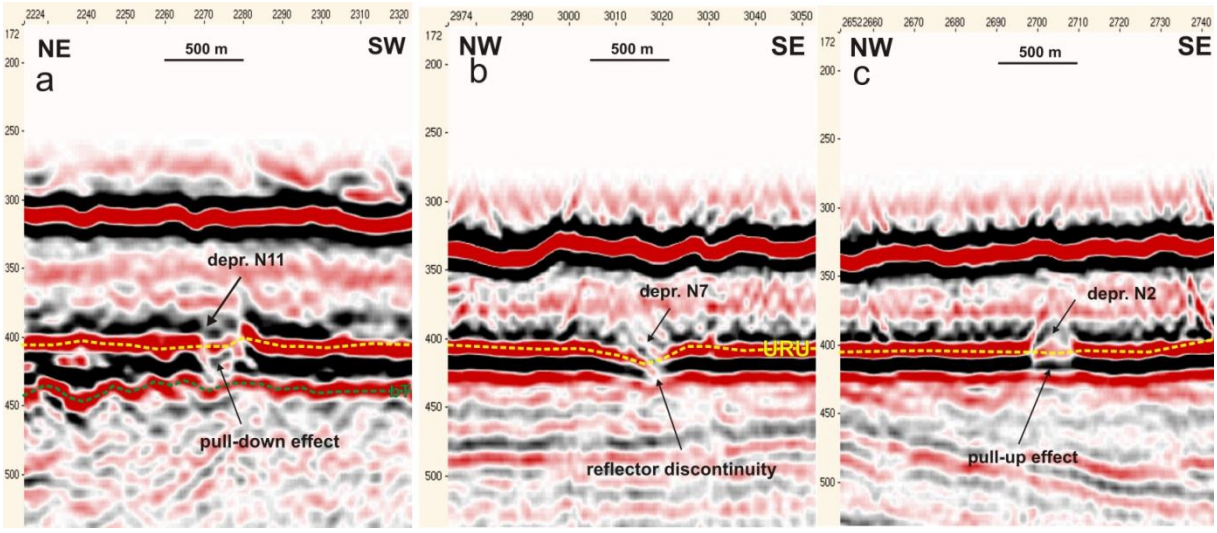

Fig. 2-27. The seismic profiles through the potential fluids migration pathways on URU reflector.

2.3. St05M09 (Ingøydjupet)

2.3.1. Depressions at the seafloor

The ST05M05 area contains 171 circular to oval-shaped seafloor depressions at the southwestern and northeastern part of study area (fig. 2-28). The large scale geomorphology shows that depressions tend to be concentrated at the top of a lobate moraine ridge that lies in front of a large depression, the so called Ingøydjupet. Depressions also concentrate around the front zone of the main Ingøydjupet trough (fig. 2-28).

The depressions are preliminary elongated; the long axis varies from 110-225 m and the short axis between 80-200 m (fig. 2-29). The average depths of the seabed depressions are from 1,7 to 6 m. The dominant orientation of the depressions is NE-SW or N-S. The deepest depressions are located between two parts of the Ingøyduppet trough (fig. 2-29). The features are circular or subcircular with diameters varying from 130-300 m and depths from 4-8 m. Examples of depressions are presented in fig. 3. The parameters such as length of the long and

short axis, depth, and orientation of the long axis and evidence for fluid migration are given in table 9.

Fig. 2-30 shows that depressions tend to be elongated and the average ratio values vary between 0,5-0,9. The distribution of the depressions according to their size and area was plotted in fig. 2-31. The area of individual size for depressions or pockmarks range between 150 m^2 and 25 m^2 (fig. 2-31). It illustrates that depressions of various sizes are spread evenly over the study area. However, smaller pockmarks tend to concentrate in the center of the 3D area and outside the Ingløydjupet main trough. Large and medium size depressions distribute predominantly along the SW part of the 3D survey (Fig. 2-31). The NE part of the study area is characterized by a slightly lower density distribution of pockmarks, but the area includes some large pockmarks and small features.

The highest pockmarks concentration exists in the center of the survey and it shows 6-7 features per sq. km. At the lobate moraine ridge the density of depressions is 2-4 per sq. km.

The mapped seafloor depressions have two prevailing orientations based on the long axis: NE-SW and NW-SE (fig. 2-32). Depressions in the south-eastern part of 3D block are mainly NE-SW oriented. In the center of 3D area the depressions are oriented in both directions.

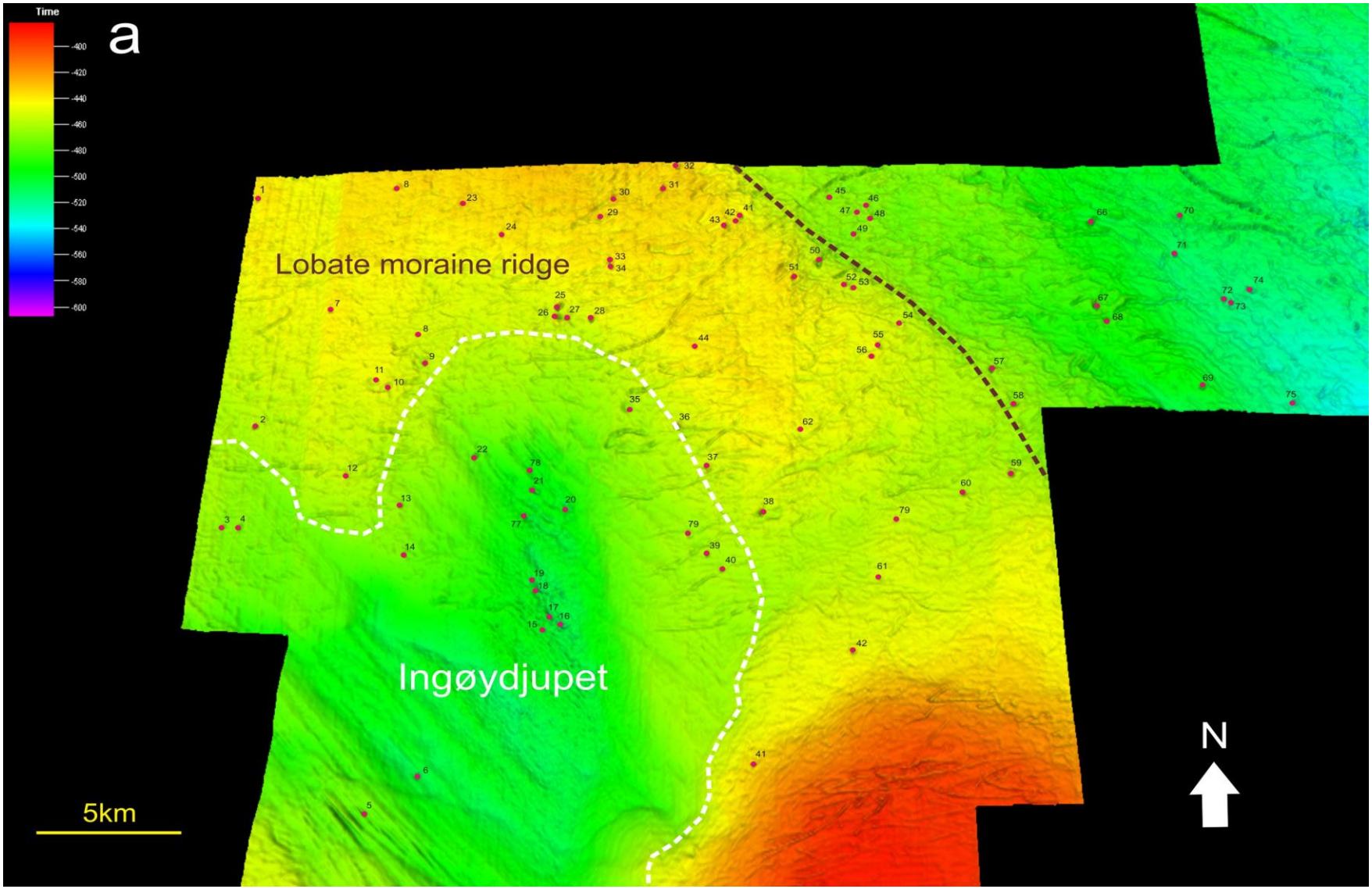

Fig. 2-28. The location of the seafloor depressions; a. SW part of the ST05M09 3D block area.

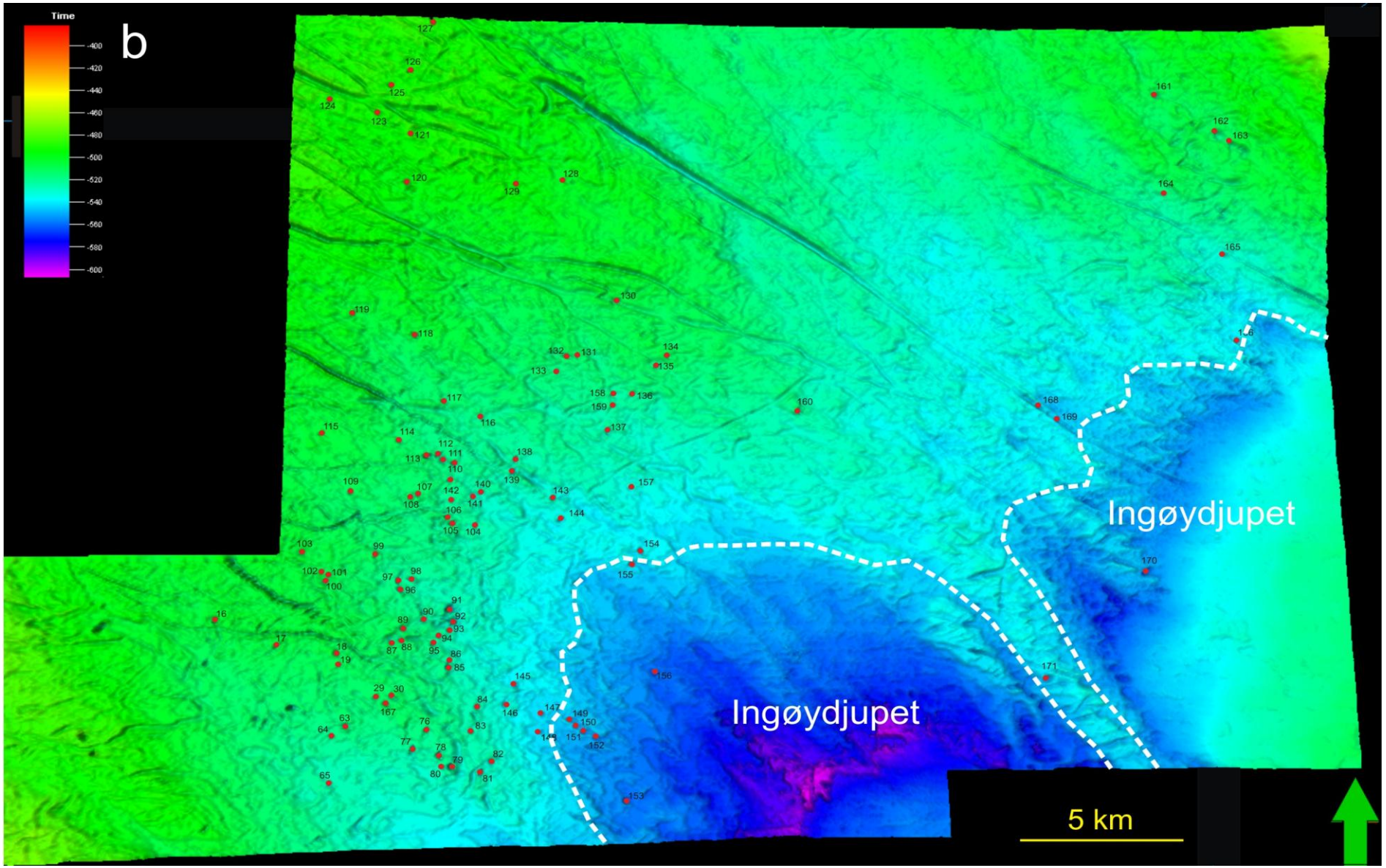

Fig. 2-28. The location of the seafloor depression; b. NE part of the study area.

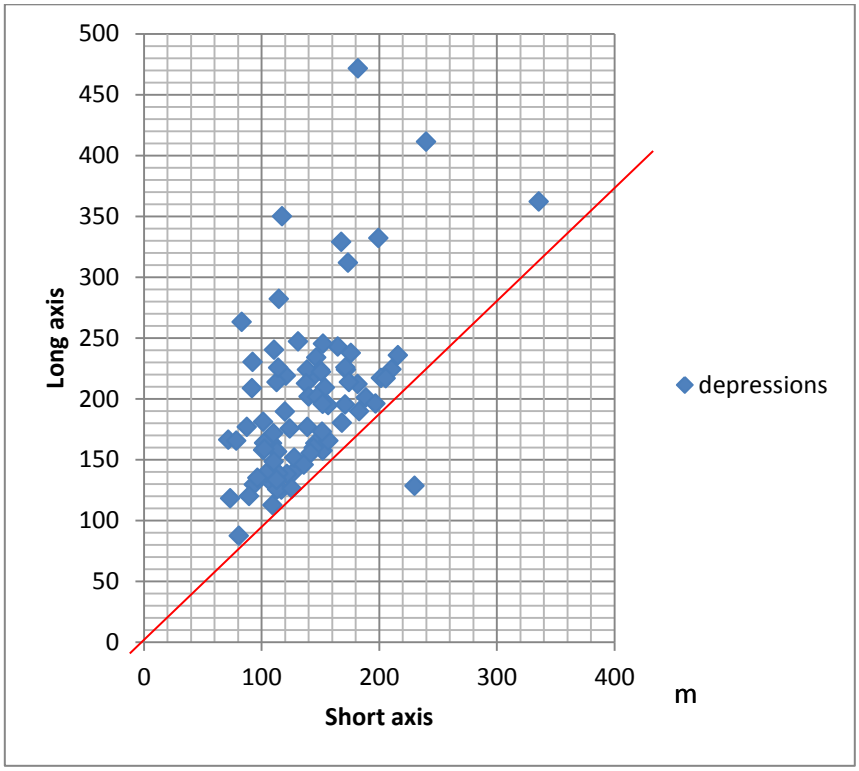

Fig. 2-30. The diagram shows the relationship between the short and long axis of the mapped depressions; the red line indicates the ratios values equivalent to 1.

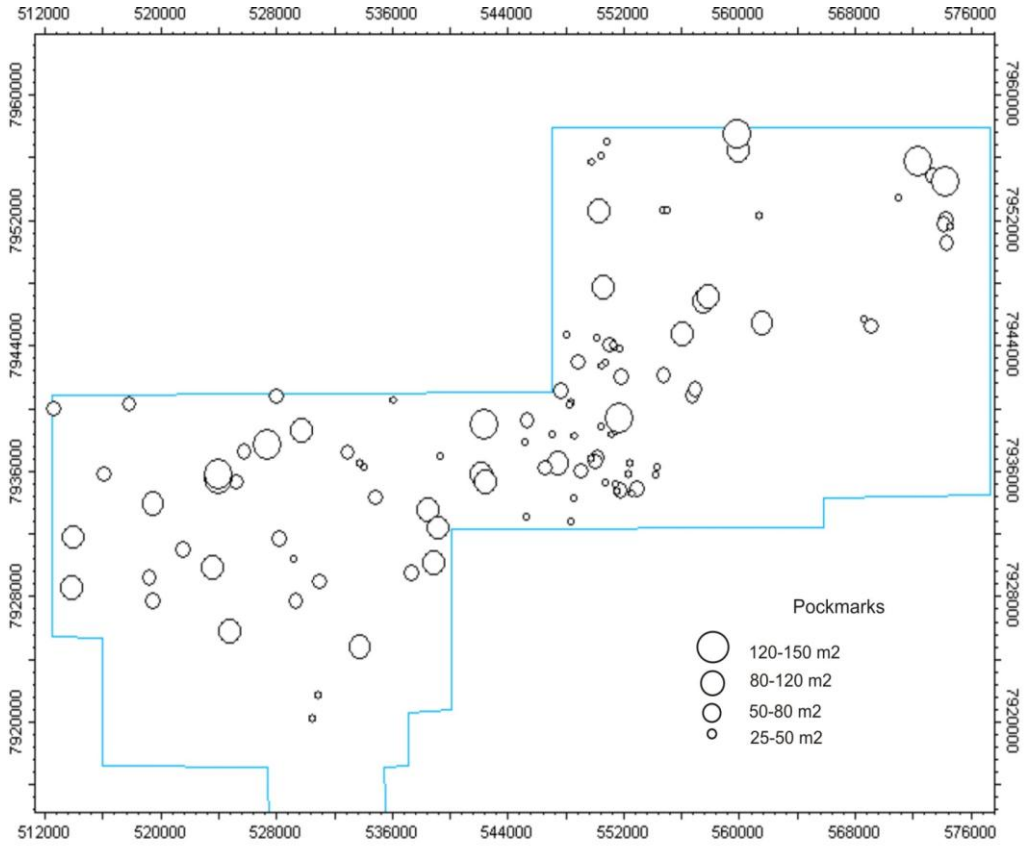

Fig. 2-31. The distribution of the size of pockmarks within the ST05M09 area.

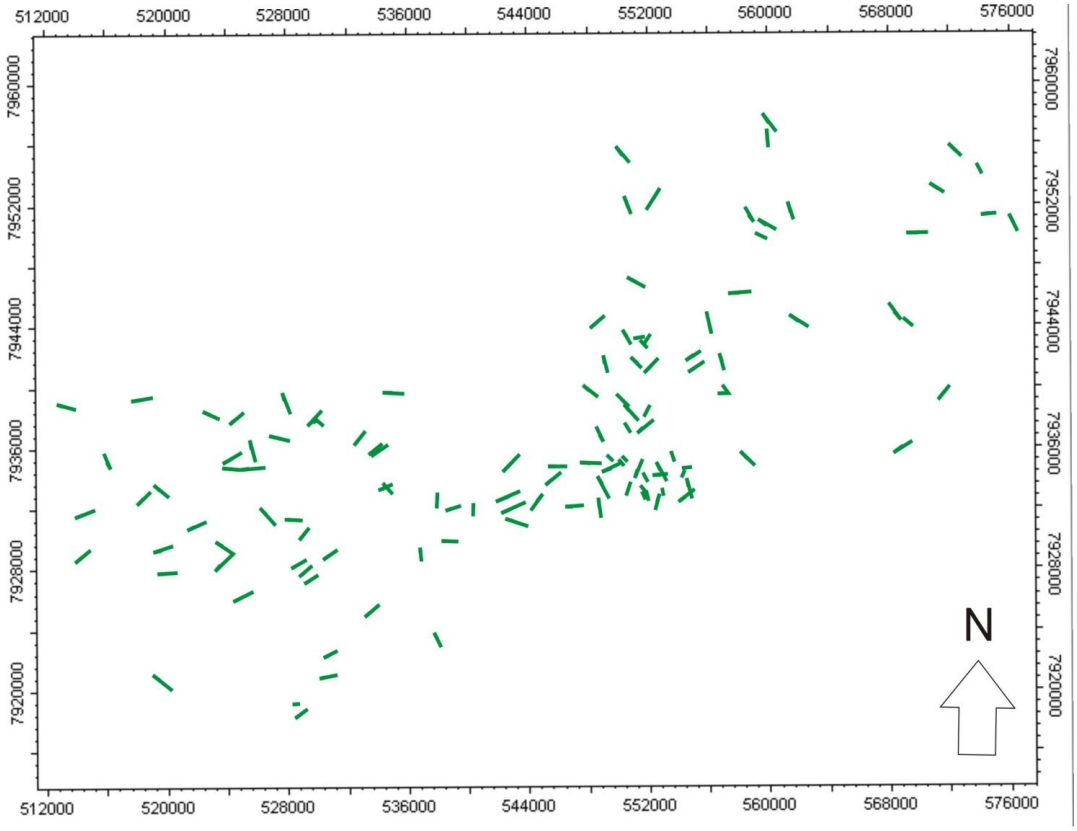

Fig. 2-32. The orientation of pockmarks according to their long axis orientation.

The orientation of the long axis could be compared with iceberg ploughmark orientations. The iceberg scours extend from Ingløyduppet to the south-west across the moraine ridge and further SE-NW trough the NE part of the 3D area. This part of the seafloor surface is shaped by ploughmarks that are NNE oriented. The ploughmarks are eroded, disturbed and crosscut by NW oriented grooves, which are a result of later glacier movements *(Andreassen, K. et al, 2008; Ottesen, D. et al., 2005)*.

The depressions of the area are more uniform if compared to the previous study area (EL0001). However, they could be subdivided into three groups:

- Circular depressions;
- Large and medium elongated depressions with ratios range 0.5-0.7;
- Small elongated depressions with ratios 0.3-0.5.

Circular depressions

The depressions are approximately 150-200 m in diameter, The circular pockmarks concentrate in the upper slope of the Ingøyduppet through and also occur on the lobate moraine ridge in the north-eastern area (fig. 2-33b).

Large elongated depressions

These depressions tend to concentrate in the lobate moraine area (fig. 2-33a) They show a 400-470 m long and a 275-300 m short axis. Depressions of this type usually appear at the end of iceberg scours, therefore originally they have developed as marked craters *(Bass D. W. and Woodworth-Lynas C., 1987) (fig. 2-35 and 2-33a).* The large elongated depressions are often followed by mounds from the side of the depression. The mound could be interpreted as a rim that comprises debris that were moved upward from the depression *(Forwick, M., et al., 2009).*

Small elongated depressions

The small elongated depressions show no preferred area (fig. 2-34c). However, their highest concentration could be observed in the center of the surveyed area outside the Ingløyduppet main trough. They are characterized by significant differences between the long and short axis (fig. 2-34c).The average short axis varies between 110-130 m and long axis between 250-300 m.

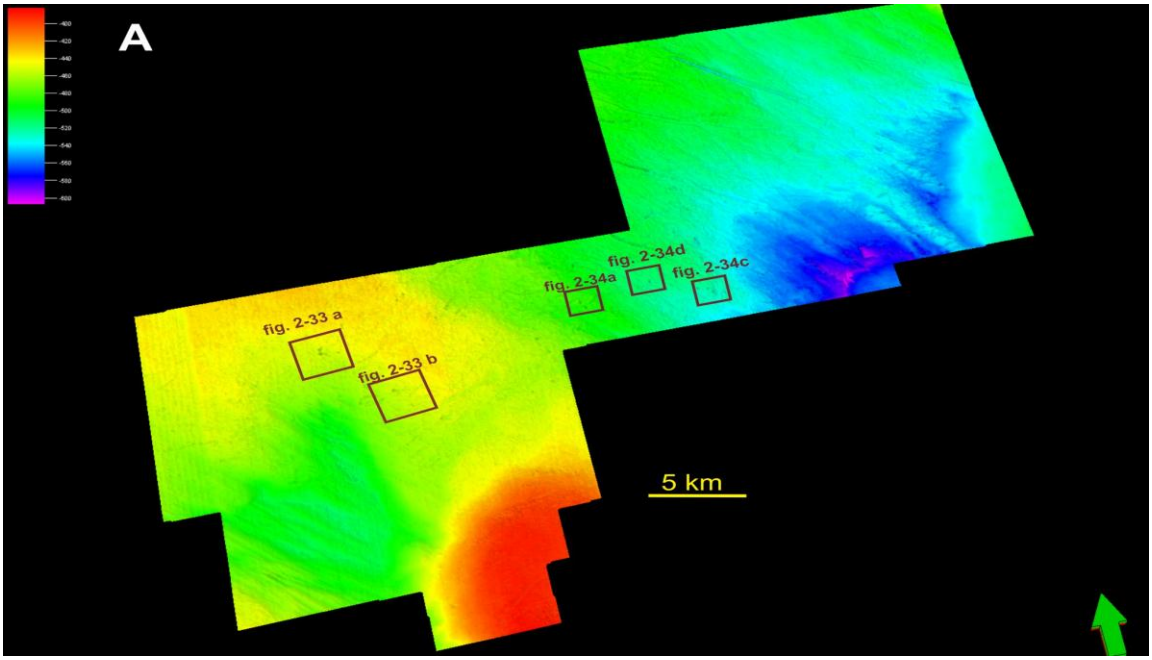

Fig. 22-33A: Location overview for figures 2-33a,b

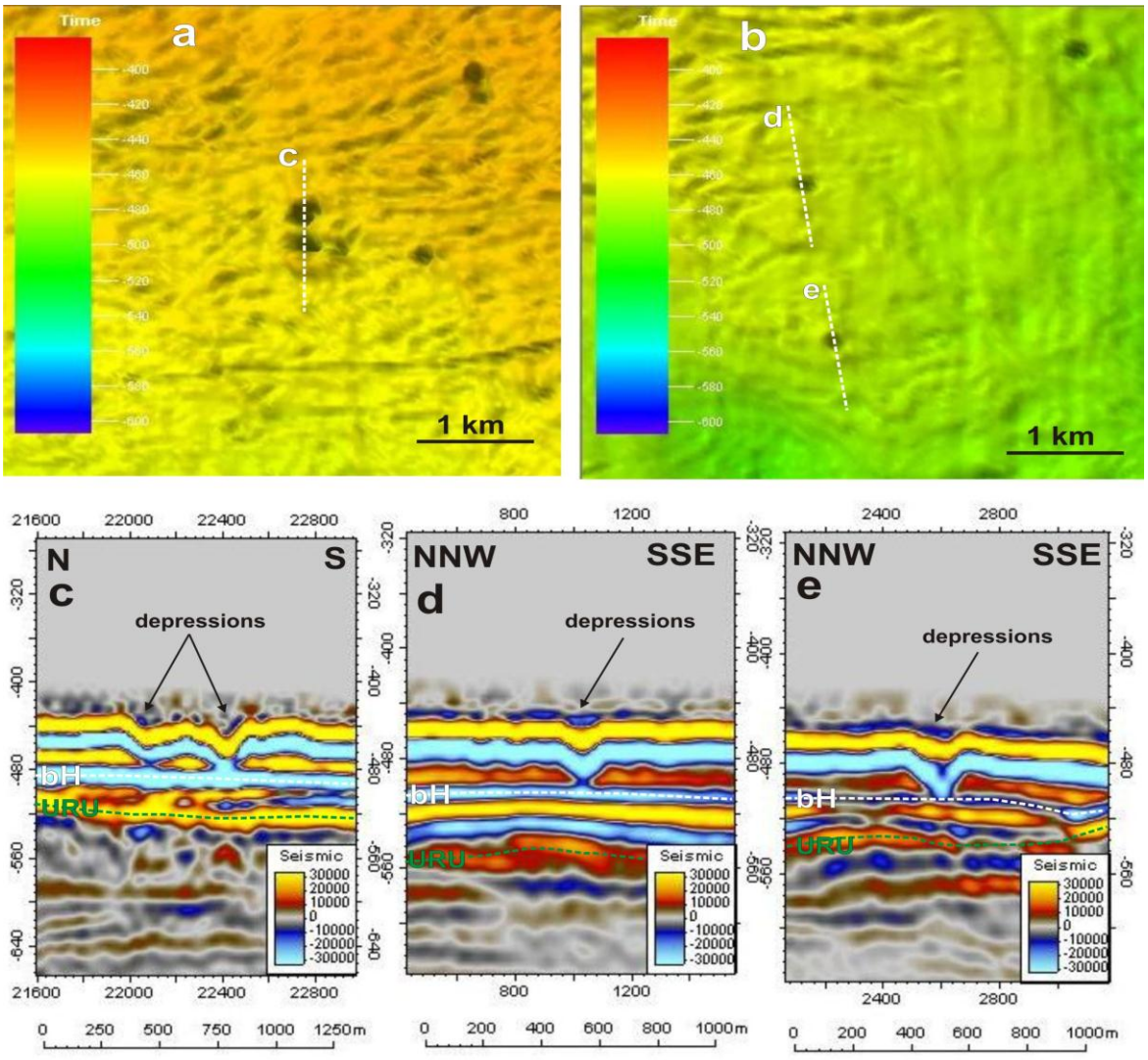

Fig. 2-33. a-b. Various seafloor depressions and c-e. seismic sections across them. Location overview in figure 2-33A.

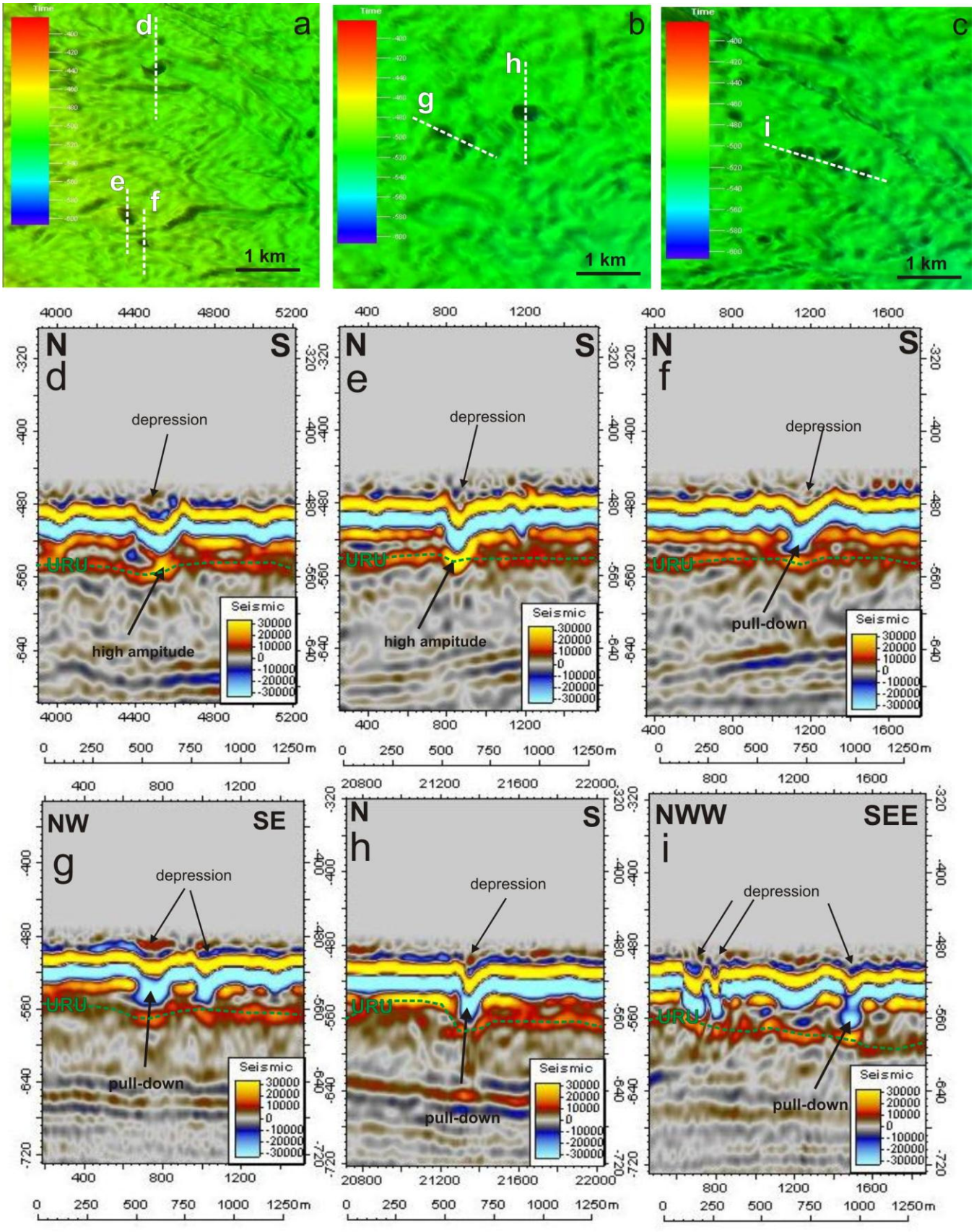

Fig. 2-34. a-c. Various seafloor depressions and d-i seismic sections across them. Location overview is shown in figure 2-33A.

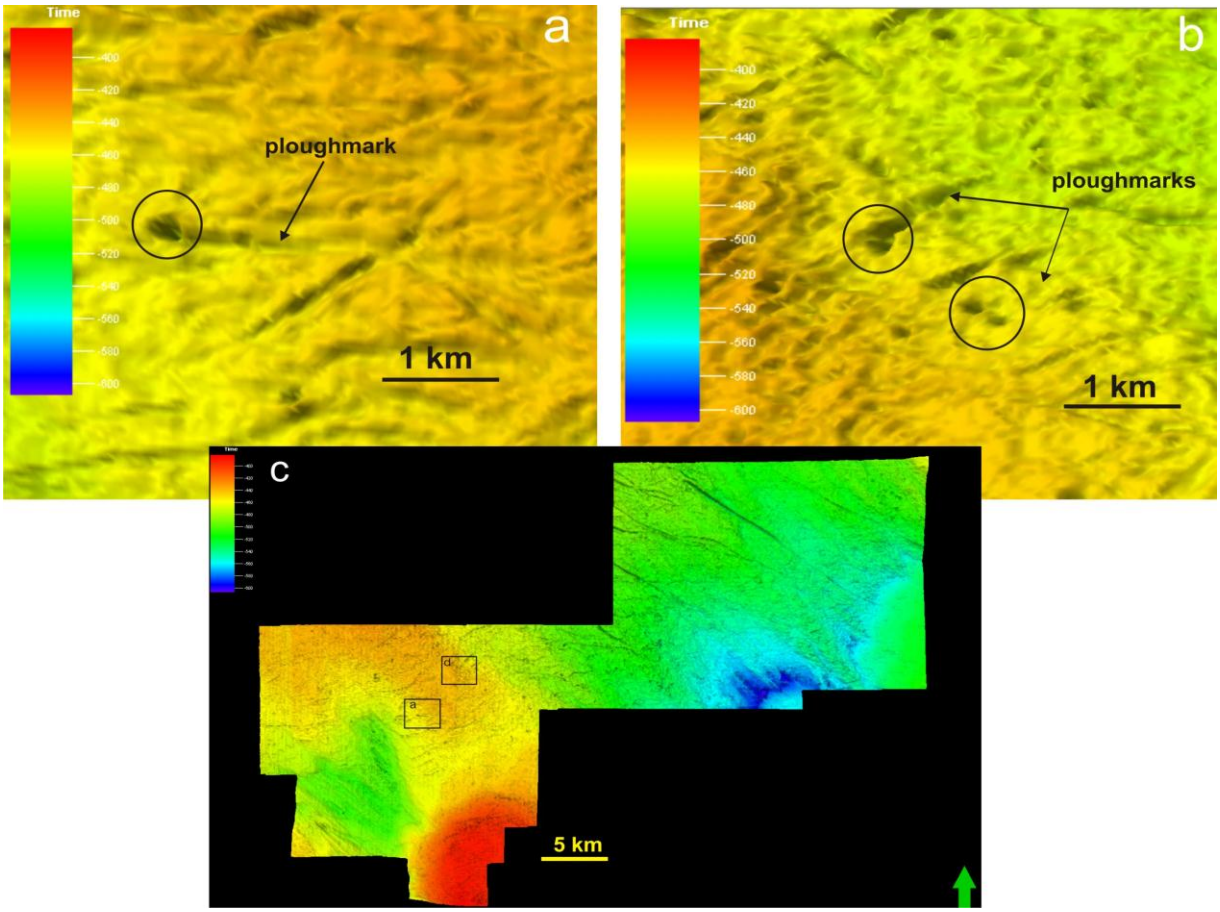

Fig. 2-35. Depressions inside iceberg ploughmarks.

2.3.2. Structures associated with depressions

Ninety percent of the pockmarks found within the ST05M09 area are associated with structures that are within the upper sub seafloor or, at or close to the seafloor. The following structures were mapped:

—Normal faults oriented E-W and N-S (fig.2-36);

—Truncated layers of three different dip directions: NE-SW, NW-SE and NEE-SWW (fig. 2-36);

Normal faults

Depressions on the lobate moraine are related to normal faults that extend from greater depth (fig. 2-36). The normal faults in the SW part of the ST05M09 3D cube have two prevailing orientations that are E-W and N-S. The depressions could be correlated only with faults that penetrate the northern side of the moraine (fig. 2-37).

Faults that reach the Quaternary sediments, could be traced until 550 ms TWT (fig. 2-37). They are potential pathways for fluids seeping from source rocks. Evidences for migrating fluids could be bright spots located at the depth 600-650 ms TWT. They are characterized by high amplitudes and a polarity reversal. Bright spots can mark the presence of gas inside Tertiary sediment layers *(Andreassen, K., 2007b; Hovland, M and Judd, A, 2007)*. The pockmarks and bright spots that concentrate along the faults are presented in the fig. 2-37.

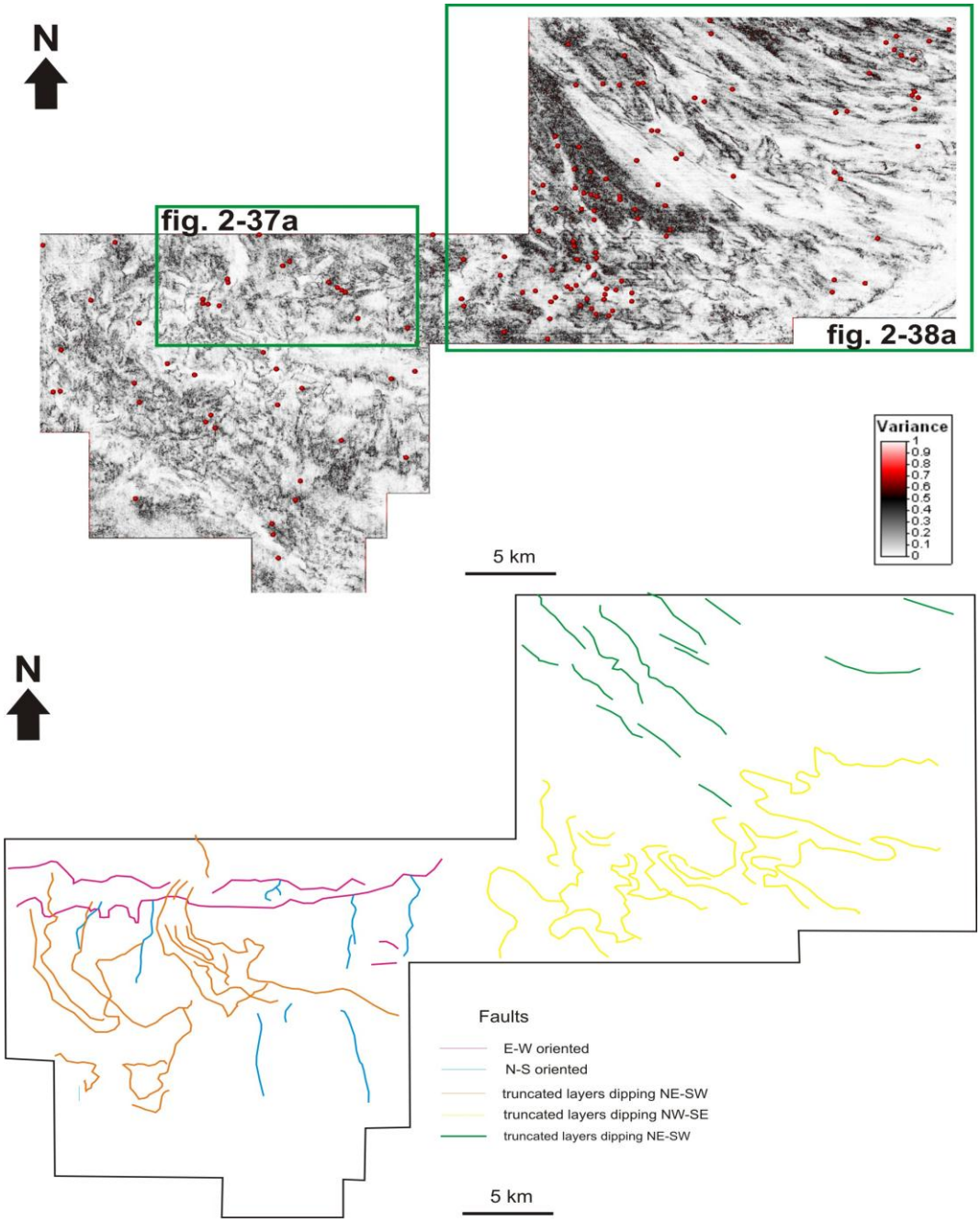

Fig. 2-36. a. Volume based chaos attribute time slice at the depth of 640 ms TWT; b. distribution of normal faults and truncated layers.

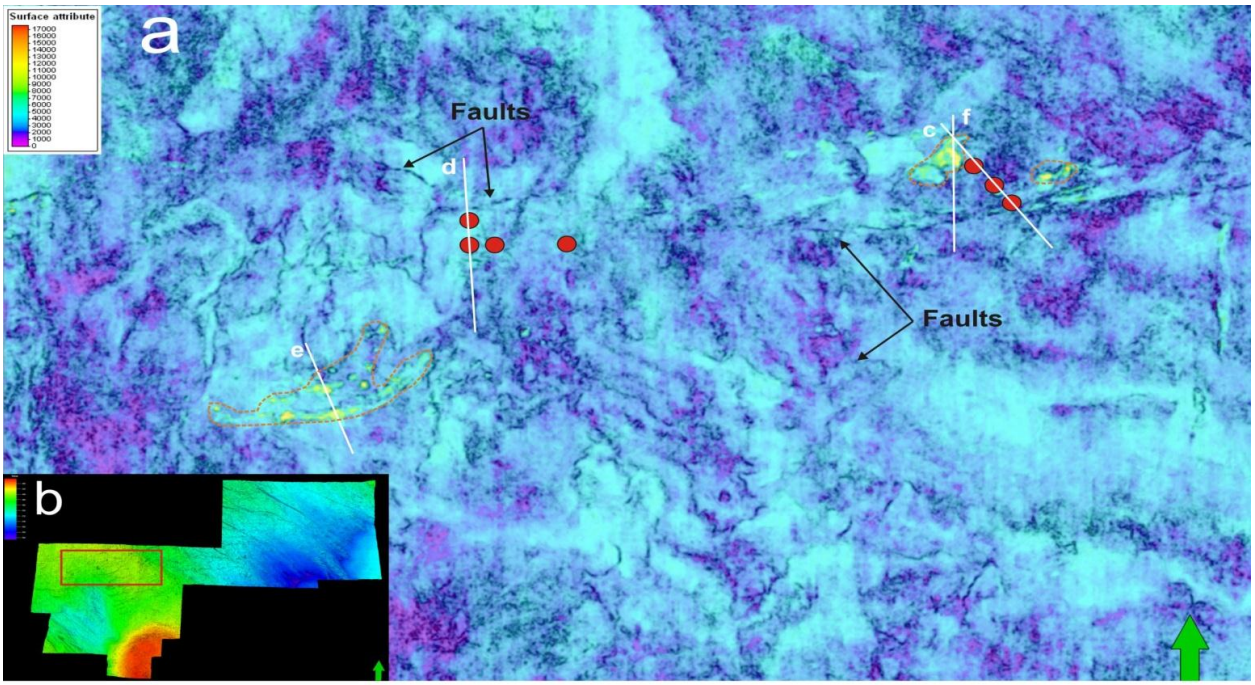
Surface attribute
a
Faults
d
c
f
Faults
e
b

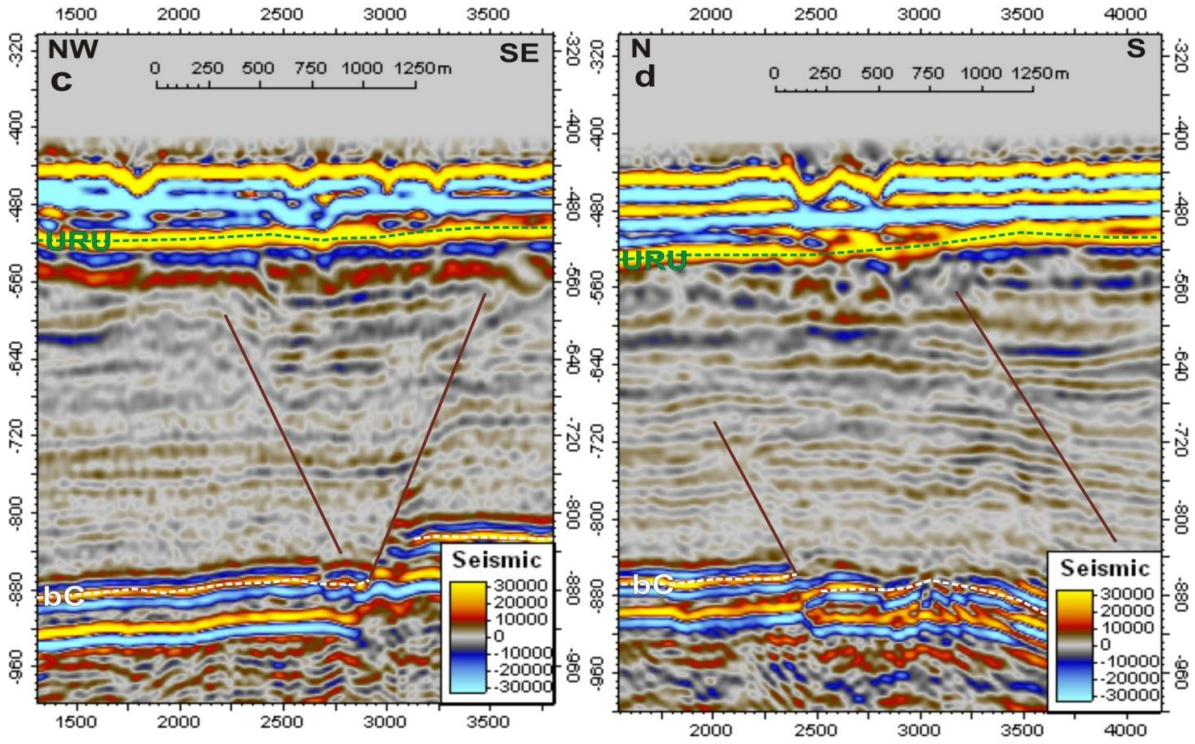
NW
c
SE
0 250 500 750 1000 1250m
URU
bC
Seismic
30000
20000
10000
0
-10000
-20000
-30000
N
d
S
0 250 500 750 1000 1250m
URU
bC
Seismic
30000
20000
10000
0
-10000
-20000
-30000

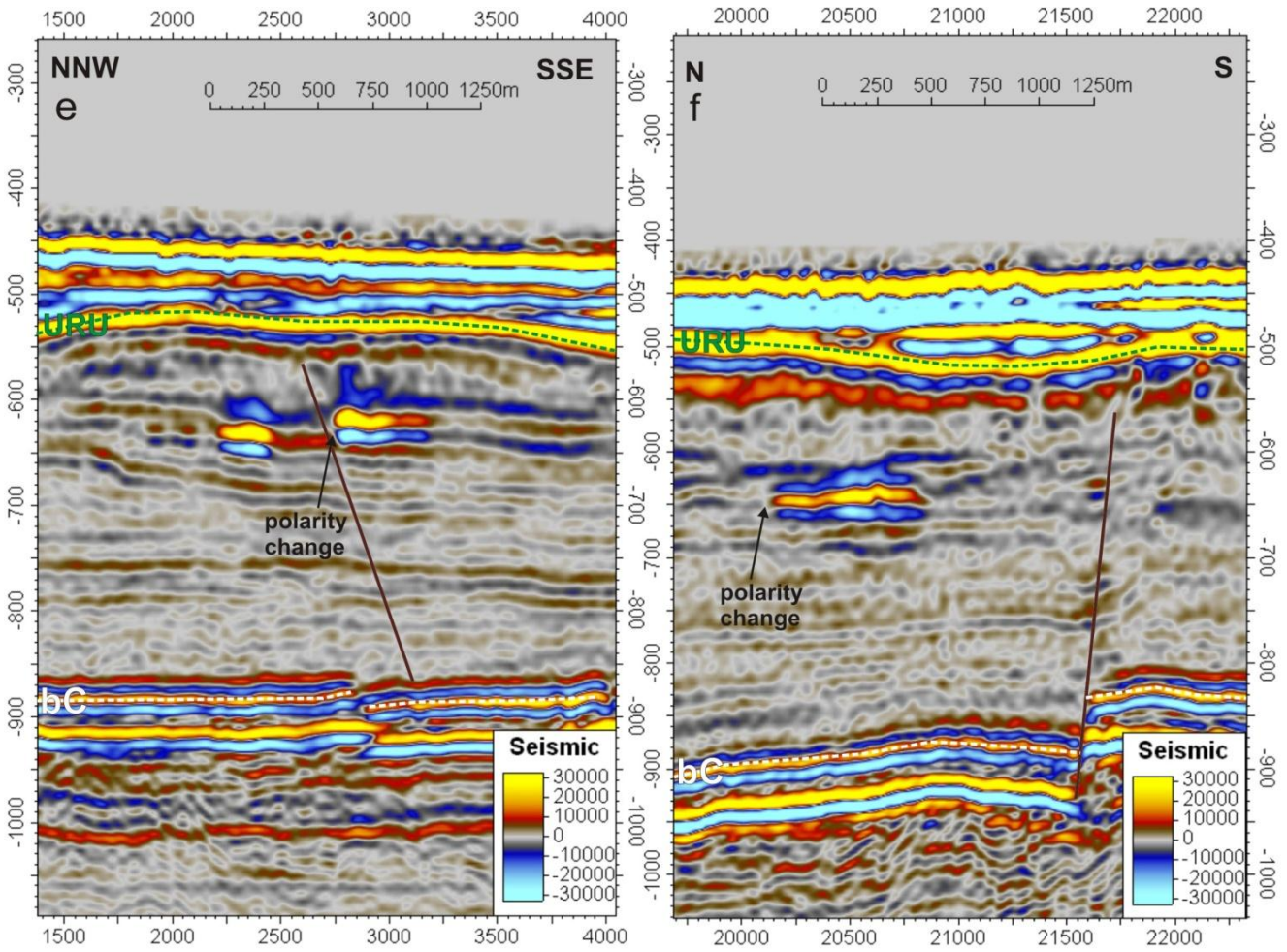

Fig. 2-37. a. RMS amplitude map at the depth 640 ms TWT (for location see fig. 2-36a); b. location of the area shown in the 2-37a; c. and d. seismic profiles across the pockmarks possibly associated with a fault; e. and f. seismic profiles across the bright spots lying close to the normal fault. Location overview given in fig. 2-36.

Truncated layers

Volume stratigraphy based attribute time slices indicate top-lap truncated layers inside the non-glacial sediment package at the depth 580-680 ms TWT (fig. 2-38). The layers are dipping in three different directions: NE-SW in the north-east of the study area, NW-SE in the center of 3D cube and NEE-SWW in the south-western part (fig. 2-38). The layers in the north-east and south-west are possibly related to elevated tectonic (horst) structures in the Cretaceous rocks. The high amplitudes and polarity changes seen in the seismic profiles (fig. 2-38) could be caused by less lithified sediments. A reflector truncation in the central ST05M09 area is located in the front zone of the Ingloydjupet trough and probably was formed by glacier erosion. An example of the association between existing depressions and truncated layers is presented in the fig. 2-38. It shows the part of the chaos volume attribute time slice around the Ingløydjupet trough (fig. 2-38).

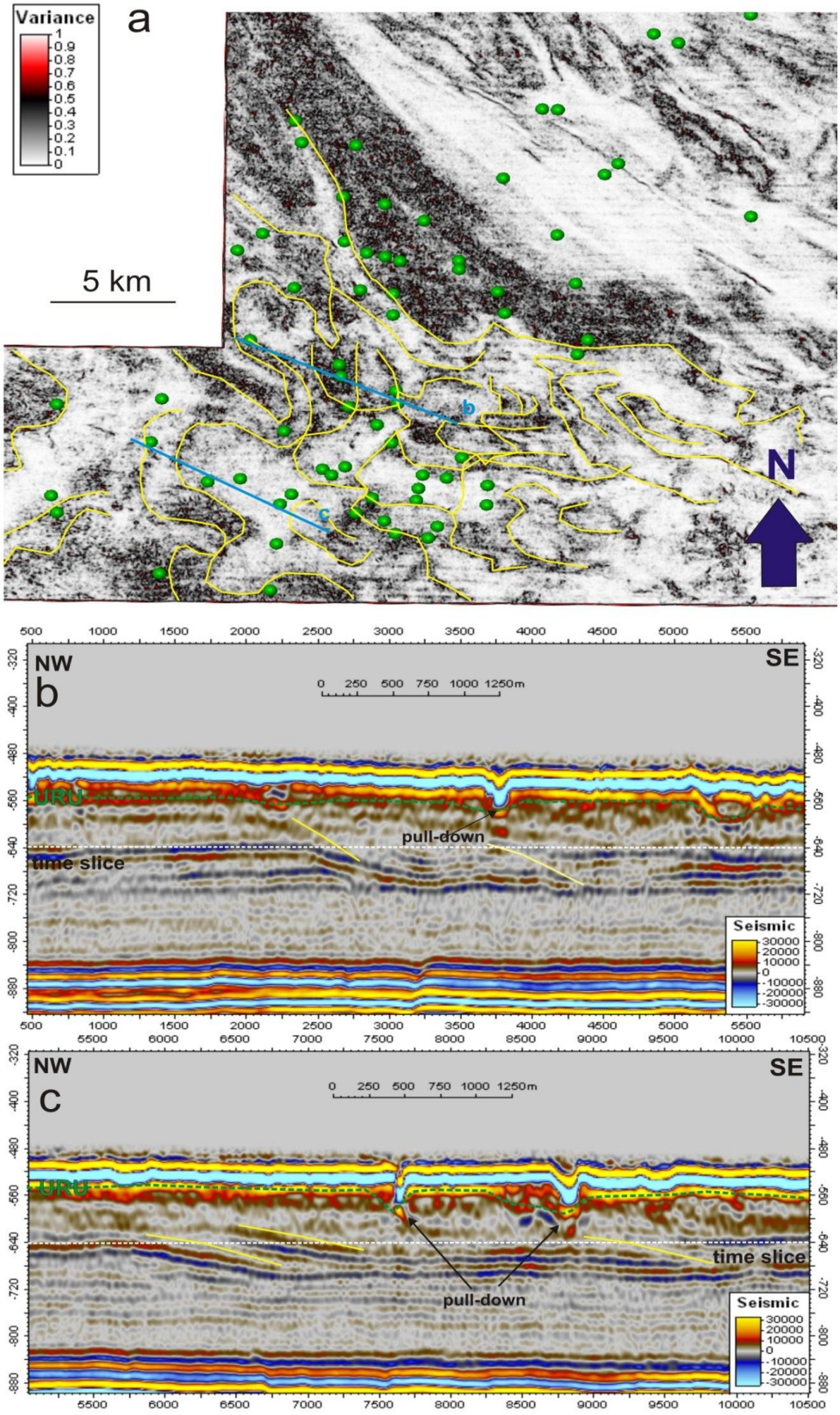

Fig. 2-38. Pockmark distributions in front of Ingøydjupet; a. Volume based chaos attribute time slice for the depth 640 ms TWT; yellow lines follow the truncated layer boundaries; green dots are pockmarks; blue composite lines mark the location of seismic lines; b. seismic line shows a link between depressions and truncated layers; c. seismic line shows link between depressions and truncated layers Location overview given in fig. 2-36.

2.3.3. Depressions at URU

Large elongated crater-like depression can be identified on the URU reflector. A total number of 27 of these depressions are concentrated in the SW part of the 3D seismic area (fig. 2-39). They are spread along the northern slope of the Ingøydjupet paleotrough. The values of their long axis vary from 680-2100 m with an average value of 1250 m. The length of the short axis varies between 300-1400 m; the average values are 750 m. Thus, the ratio between short axis and long axis are 0.5 –0.6; it means that the dominant shape of the depressions is elongated.

In the NE part of the study area, depressions are identified 1,5-2 km outside the Ingøydjupet main trough. In comparison with depressions in SW part of 3D cube the depressions in the east they are circular or subcircular and smaller: the short axis length ranges between 300-700 m and the long axis between 200-700 m. The depth of the depressions in the east is 35-40 ms TWT.

The dominant orientation of the long axis of the depressions is SE-NW and several depressions form a chain of depressions, which is stretching out from the trough body to the NW (depressions Nr 1-3-8; Nr. 2-9; Nr 4-10-11-13) (fig. 2-39a and b). Fig. 2-39b contains the SW part of the 3D block in perspective view nicely showing MSGL in the east which terminate in craters N30, 17, 14.

In seismic profiles, it is noticeable that the depressions were filled by sediments and overlain by modern sediment starting at the base Holocene reflector

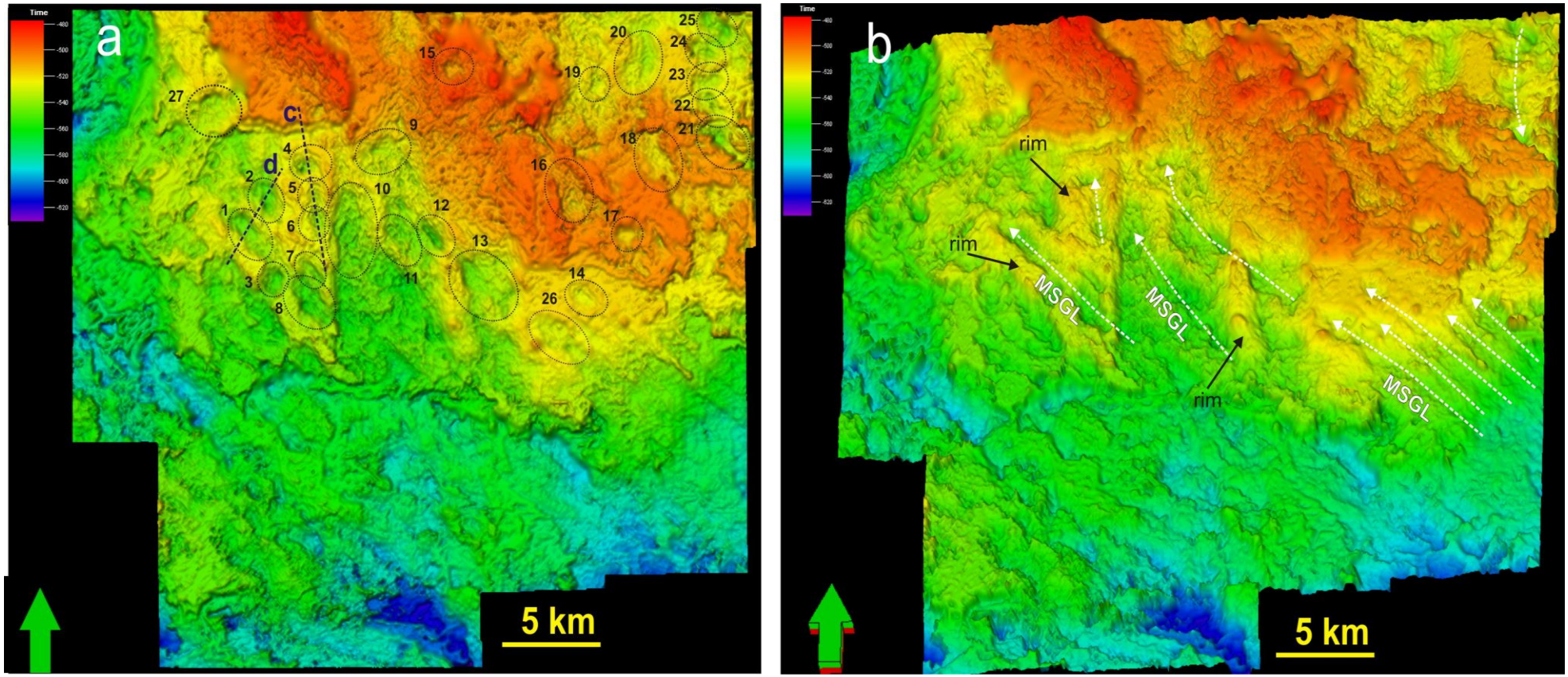

Fig. 2-39. a. 3D view of the SE part of URU subsurface, black dashed lines show the position of seismic lines (fig. 2-39c-d), black circulars outlines the depression areas; b. 3D view of the SE part of URU subsurface; white arrows illustrate the direction of MSGL;

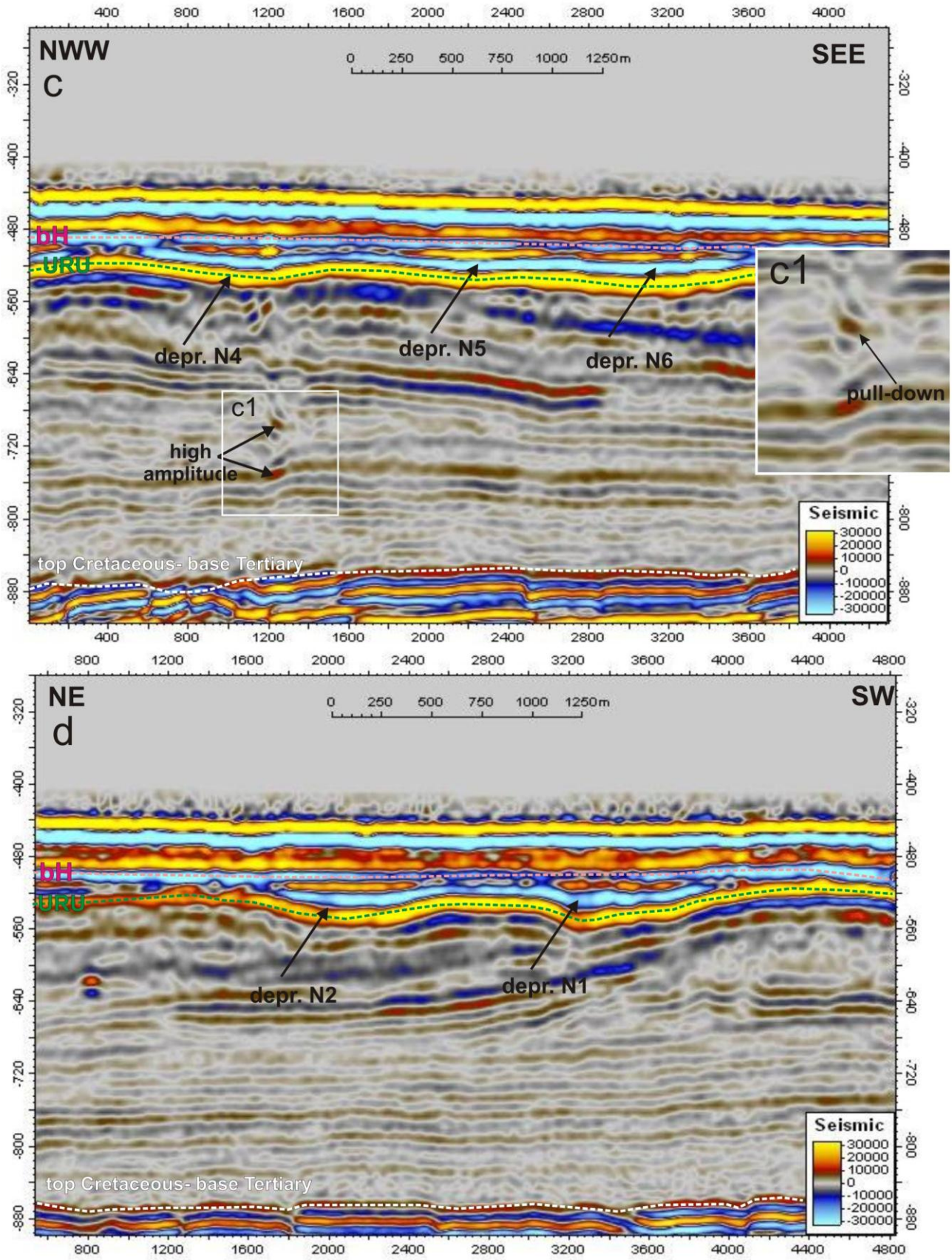

Fig. 2-39. a. c. seismic profile across the depression shows thickness variations and high ampitudes, d. seismic profile shows clearly the depressions.

The depression Nr4 (fig. 2-39c) is characterized by a high seismic amplitude of depressions infill, which could be caused by the presence of gas *(Andreassen et al., 2007a)*. Seafloor pockmark distributions along the western part of 3D cube spread between the depressions on URU (fig.2-40). That may indicate that the Quaternary deposits are thinner between the depressions and might be more permeable for fluids (fig. 2-40).

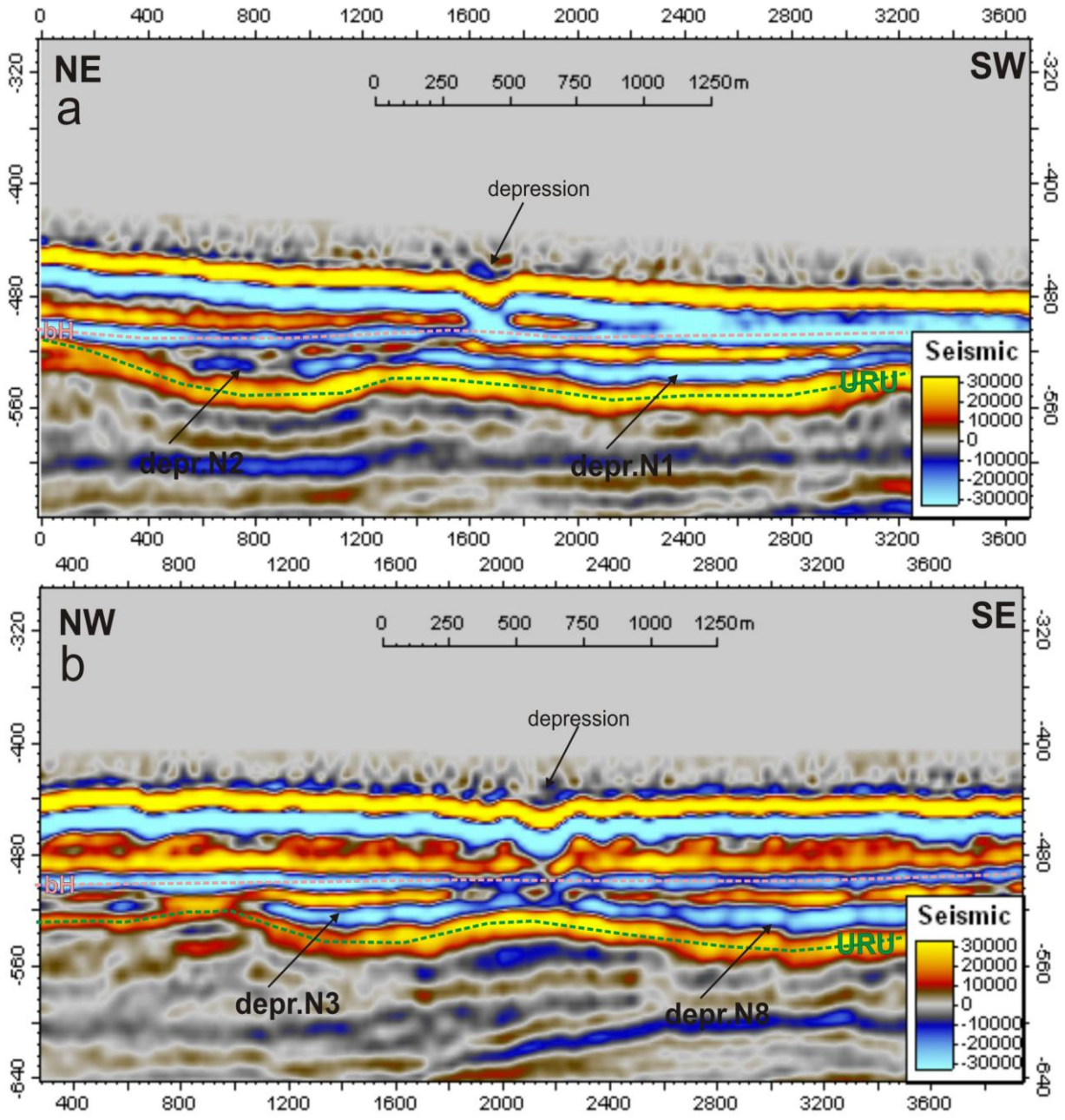

Fig. 2-40. a. and b. Seismic profiles show examples of depressions on the seafloor that are placed between two depressions on URU.

3. DISCUSSION

The results present various depressions on the seafloor and on URU that will be discussed concerning possible causes for their development. They may have been formed by processes such as fluid flow, melting of dead ice, iceberg grounding and/or melt water erosion. Possible mechanisms of creating the observed depressions will be proposed in the following chapters.

3.1. Origin and distribution of the depressions according to glacier morphology

The distribution of depressions on the seabed and URU provides a first baseline for understanding better possible scenarios for their development. The results from the EL0001 and ST05M09 3D studies show that the depressions on the seafloor and subsurfaces tend to be concentrated around glacial troughs and related morphological elements (fig. 2-28 and 2-8). The EL0001 seafloor and bH horizon show a concentration of depressions at the south side of Bjørnøyrenna trough at a depths 450-500 m. The remaining depressions are distributed around the westernmost elongated ridge that was interpreted as a drumlin. The depressions on URU (example area IV) are located in the front slope and northern slope of the glacial troughs. Along the ST05M09 seafloor the depressions are spread in the front and side moraine of the Ingøydjupet paleo-trough (SW part of the cube) and along the western side of the recent Ingødjupet trough.

An obvious lack of depressions inside the central part of the glacial troughs may suggest that fluid migration – if it existed- does not occur in potentially more consolidated sediments of glacier troughs. However, it may also indicate that the 3D data resolution is not good enough to identify small depressions inside the troughs as the depressions probably tend to be smaller in size from the edges towards the deeper parts of the troughs *(Chand et al, 2009)*.

According to *Judd and Hovland (2007)* the density of pockmarks and the size of the depressions tend to increase with a decrease in grain size of the sediments. *"Soft silty clays seem to provide the ideal sediments for pockmarks formation" (Judd and Hovland, 2007)*. Within the Barents Sea the fine sediments are spread along the bottom of troughs and coarsening towards the flanks and banks *(Elverhøi, 1989)*. From this presumption, the best

sedimentary conditions should occur inside and not around the troughs as observed in this this study. However, seismic data indicate that decreases in the thickness of the Quaternary sediments also favor the creation and distribution of pockmarks (fig. 2-40). As the glacier moved along the troughs it caused the erosion of the upper sediment layers and excavated harder and deeper sediment strata (Winsborrow, 2009; Andreassen, 2007). Based on the presented observations, the location of depressions in the study area where pockmarks exists cannot be easily explained.

The seafloor from the EL0001 shows depressions in the north-east of the 3D block (craters Nr. 13, 14, 15, 16, 17, 18, 19, 20, 21) (fig. 2-1). The area of depressions is located at the side of the Bjørnøyrenna trough where URU is located close to the seafloor. The ST0309 3D cube shows depressions that were found in the east where the thickness of Quaternary deposits decreases (fig. 2-21).

Fig. 2-1 illustrates (EL0001 3D cube) that depressions (Nr. *1, 6, 7, 9, 10, 11)* are distributed around the westernmost elongated ridge that was interpreted as a drumlin (fig. 2-8). On URU, subsurface depressions are distributed in front of the drumlin (fig. 2-8). The lack of depressions on the drumlin is explained by the greater thickness of glacigenic deposits and very heterogenous material that may prevent fluid flow. As suggested by *Benn and Evans (1998)* most of drumlins are composed of unconsolidated but very heterogeneous sediments.

3.2. Possible origin of depressions inside glacial erosional features.

All three 3D data show depressions that occur inside glacier ploughmarks, MSGL or channels.

Mega-scale glacial lineations

Some depressions identified in the ST05M09 and EL0001 3D seismic surveys are located inside MSGL (figs. 2-8, 2-28). The orientation of the long axis of the depressions does often but not always coincide with the direction of the MSGL. On the ST05M09 3D survey the depressions that are connected with the MSGL are also located inside a glacial trough. The long axis of the depressions is oriented parallel to the MSGL but not to the glacial trough direction. On the EL0001 3D data the depressions occur also within theMSGL and are located on the bH subsurface. They form chains of depressions along the MSGL (fig. 2-1).

The pockmarks inside the MSGL could be formed by subglacial drainage *(Benn and Evans, 1998)*. A high pore-water pressure build up may have existed due to rapid loading by glacier ice. When the glacier retreated, the overpressured water and fluids were discharged,

which may have caused the depressions inside the MSGL *(Chand et al, 2009; Benn and Evans, 1998).*

Iceberg ploughmarks

Depressions occur also at the end of iceberg ploughmarks (fig. 2-35 and 2-33a). The depressions could be interpreted as iceberg groundings. An iceberg could be stopped because of grounding in stiffer sediments or elevated seabed morphology. It could move around at the locked position creating a depression in the bottom *(Bass and Woodworth-Lynas, 1988)*. Iceberg scours on the ST05M09 seafloor were observed from the Ingøydjupet trough towards the moraine ridge in the front of a paleotrough (figs.2-28, 2-35). An iceberg could have been stopped due to increases in seafloor height and formed a depression during its movement on the site (fig.2-35).

Depressions occur in the URU interpreted surface of EL0001 3D data (fig.2-19). The depressions are located in the north-east of the continental paleo shelf (fig. 2-17). However, here the depressions are connected with clear acoustic pipes which started from URU and are traceable to the bH reflector. From this acoustic observation, the depressions could be interpreted as fluid flow related pockmarks *(Hovland, 1981; Judd and Hovland, 2007) that have nothing to do with ice-formed depressions.* The seismic profiles show chaotic reflections below depressions (for example N1) and also seismic phase polarity changes (fig.2-19) indicating possible gas accumulation.

Subglacial channel

ST0309 3D data contains the meandering channel in the east of the study area (fig.2-21). The feature was interpreted as subglacial channel because the channel moves upward and also cuts through elevations in bathymetry. According to Benn and Evans (1998) "*in water filled subglacial channels, flow is driven by gradients in water pressure as well as elevations, so water can flow upwards*." At the interpreted bT horizon which is the base Tertiary two large faults or erosion features were found under the meandering channel (fig. 2-21). Thus, subglacial channels could be "*influenced by bed topography because anyway meltwater tend to avoid the highest points in bathymetry*" *(Benn and Evans, 1998)*.

Many depressions were found in the bottom of the subglacial channel (fig.2-21). These depressions may have formed because of increasing flow velocity in places where meltwater overflow obstacles and create erosional depressions *(Kor et al, 1991)*.

Kettle outwash landscape

In ST05M09 on the URU horizon there are 31 elongated depressions (fig. 2-35). The depressions are surrounded by a rim. The depressions could be interpreted as *kettle outwash plain* or *pitted sandar (Benn and Evans, 1991).* The depressions form a chains of depressions that repeat or continue the direction of the stream lines inside the glacier paleo trough. The "craters" probably were created by the melt-out of the transported ice blocks *(Benn and Evans, 1991).*Within ST05M09 area the ice sheet went up to the elevated topography, lost its velocity and started to outflow leaving the ice blocks (Benn *and Evans, 1991).*

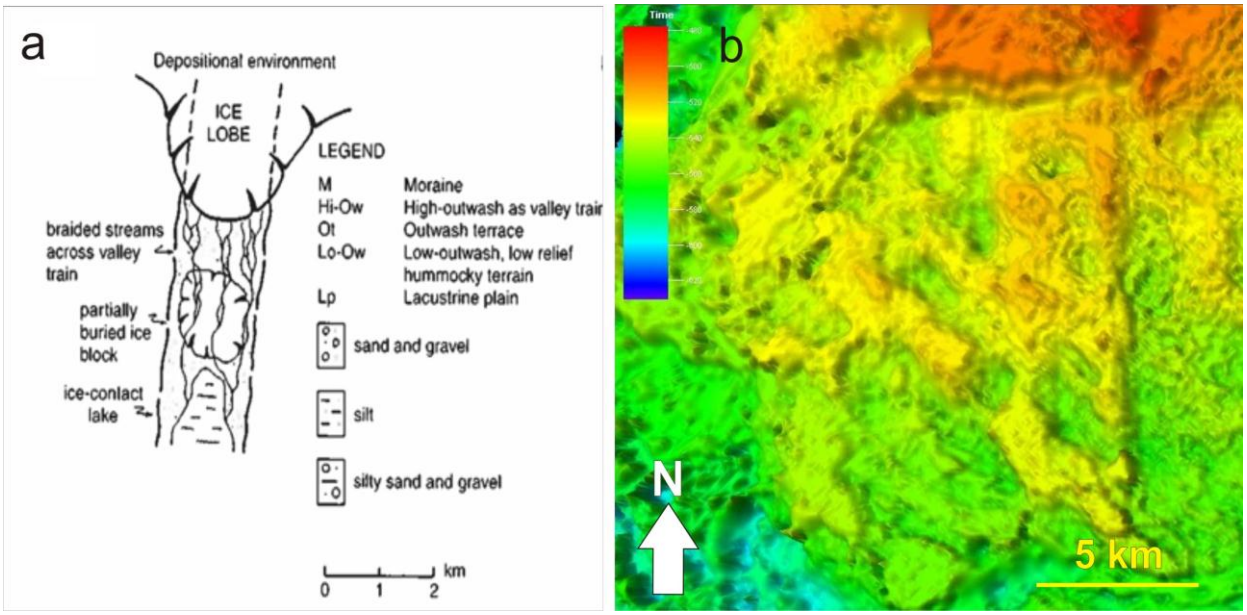

Fig. 3-2. The kettle outwash plains formation (Benn and Evans, 1998).

3.3. Fluid flow migration

At the seafloor and interpreted base Holocene reflector there are shallow crater-like depressions in 3D cube Eloo01 (fig. 2-1). Three main observations connected with the depressions are:

- Depressions on the seafloor are not placed directly above the depressions on the bH reflector (fig. 2-1);
- Most of the depressions are not associated with interpreted shallow fluid accumulation features and fluid pathways (figs.2-3, 2-4);
- Most depressions (except of Nr. 1, 2, 3 and 12 on the seafloor) penetrate through ploughmarks (figs 2-3a,b).

The depression Nr. 1 at the seafloor and at the bH reflector (fig.2-3) shows acoustic blanking which starts from the URU. The acoustic dimming could be interpreted as an acoustic chimney. The chimney is circular in the seismic amplitude base attribute map and vertical in the seismic profile (fig. 2-7). Accordingly, the chimney could be interpreted as a blow-out pipe *(Cartwright, 2007)*. Therefore, the crater-like depression N1 probably could have been formed due to fluid expulsions. As the craters are uniform in shape and size they could have been created by a similar process in time and space.

Fluids were under higher pressure during glacial times due to glacier load on top of the sediment layers beneath the ice sheet. After the glacier retreated the upper sediments were rapidly unloaded, which may have caused overpressurized sediments to release fluids in blow-outs. The creation of seafloor crater-like depressions probably was occurring in postglacial times and lately after the Last Glacial Maximum (22 ka).

Four depressions on the seafloor (Nr. 1, 2, 3 and 12) are crosscut by iceberg scours (fig...). It provides evidence that some of these depressions were created in postglacial times. The depressions 2 and 3 are located on one of the elongated ridges (fig.2-1a). As the crater-like depression Nr. 1 at the seafloor is placed above the same crater at the bH subsurface and connected with it by an acoustic chimney, the crater Nr.1 possibly stayed active after the Weichselian glacier retreat. The depressions Nr. 1, 2, 3 and 12 located in the south of the study area are on a topographic high if compared to other depressions. The glacier retreated towards the Bjørnøyrenna first from the topographic highs (S-N direction within the study area) *(Winsborrow, 2009)*. Therefore, the four depressions may have been formed earlier than other depressions on the seafloor located in topographic lows.

One depression shows three layers of sediment infill (2-3c), . The observation suggests that fluid expulsions may have been reinitiated for at least three times.

The area of depressions concentrated in the south (area V) includes acoustic pipes that pierce through depressions towards bF and bH reflections (figs. 2-16, 2-18). The depressions (Nr. 34-38; 43-45) may have been caused by the presence of migrating gas in the

pore space of the sediments *(Andreassen, 2007a)*. The depressions (Nr. 34 and 35) are seated above normal faults that develop from the depth of 1250-1300 ms TWT. They are connected to amplitude anomalies which are located beneath at 1300-1350 ms TWT (fig. 2-16). The seismic anomaly suggests the presence of fluids: it is marked by a bright spot at the top and a flat spot at the base (fig. 2-18) *(Andreassen, 2007a)*.

Through Tertiary sediments composed of mudstone fluids can migrate along fault surfaces *(Aydin, 2000)*. Reaching the glacial sediments the fluids continue to migrate through the interconnected pores of sediments to the bH horizon *(Ryseth, 2003)*, which is more permeable for fluids *(Brandes, 1995; Shepherd, 1989)*. Fluid pathways inside the Plio-Pleistocene layers are expressed as acoustic pipes and are characterized by a seismic amplitude increase and acoustic distortions. The acoustic pipes are topped by the high amplitude anomaly on the bH reflector where the fluids probably stopped as there are no noticeable acoustic pipes between the bH horizon and the seafloor and no clear morphological expressions of fluid migration exists at the seafloor (fig. 3.3.).

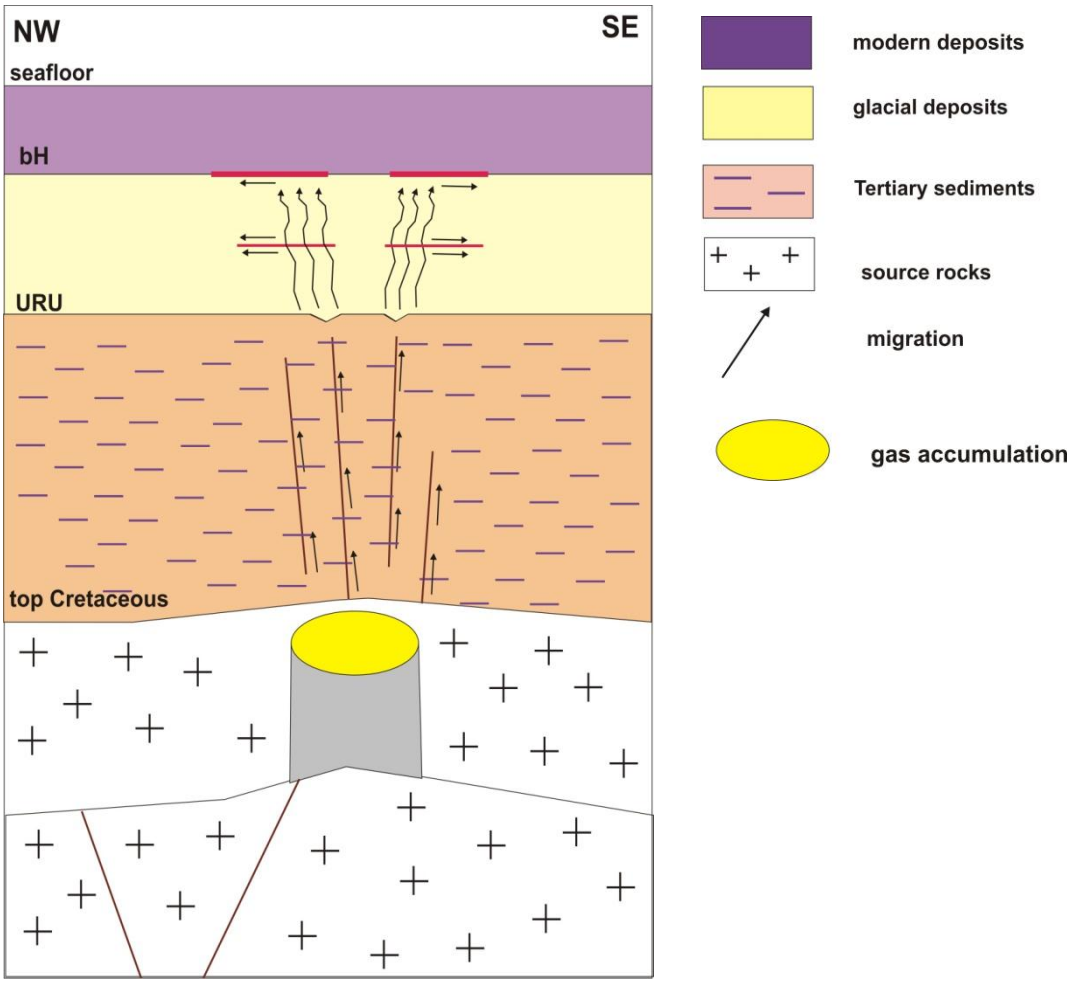

Fig. 3-3. Sketch of gas migration through Tertiary sediments based on (seismic cube ELoo01) figure 2-18b.

Depressions (area III and I, fig. 2-10) concentrate in the front zone of glacier troughs (fig. 2-14 and 2-15). In the seismic profiles that cross some of the depressions it is noticeable that they are distributed at the top of the truncated Tertiary layers. The depressions are placed exactly under the boundary of the two truncated layers of the Tertiary and Cretaceous. The truncated layers are connected with deep potential gas accumulations that are located at the depth of 1350-1500 ms TWT (fig. 2-15a,b). At the shallow subsurface, small but high amplitude anomalies occur 10-20 ms TWT above the depressions and at the URU (fig. 2-15a1).

The depressions could have been particularly formed in areas of both different lithologies and intensive glacial erosional processes. Before the glaciations (2,7 Ma ago) fluids may have been trapped within favourable strata. After glaciations with intensive erosion and after the layers were eroded fluids could reach and leak through the seafloor forming the depressions (fig. 3-4.).

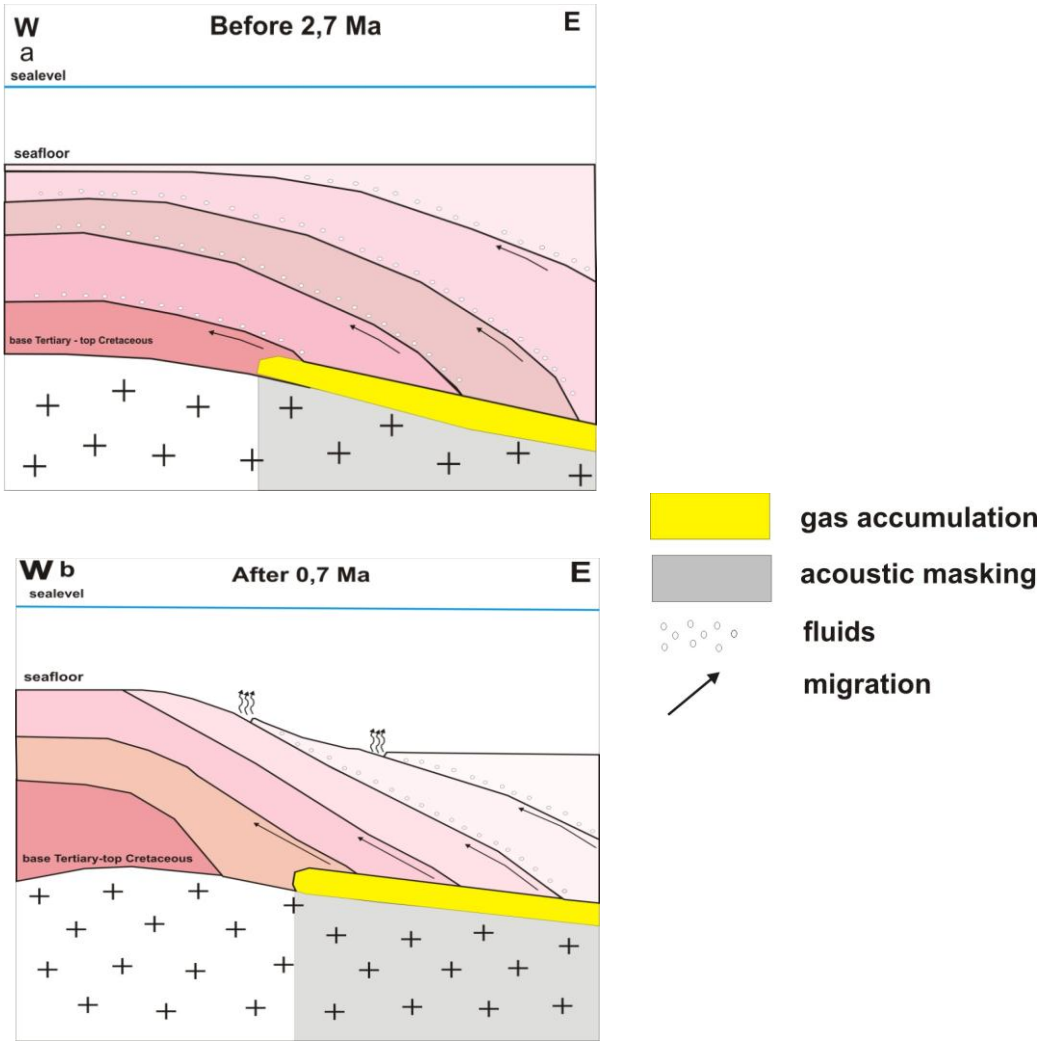

Fig.3-4. Possible stages of depression formations at EL0001 3D survey (URU) based on figure 2-15 a,b. The inferred ages after 0.7 Ma speculative.

Depressions *Ingøydjupet* (ST05M09) at are not supported by the obvious seismic indicators for fluid flow. Despite, the depressions have some other characteristic features which are:

- Clear rim in the 3D surface map (fig. 2-33a);
- Lifted rim from the side of the depression (fig. 2-34)
- V-shaped form in the seismic profile (fig. 2-34h,i)
- High amplitude anomalies in the shallower sediment strata (figs. 2-33, 2-37, 3-6)

The lack of clear fluid leakage pathways could indicate that fluids are situated close to the seafloor or spread laterally inside the shallow layers (fig. 3-6).

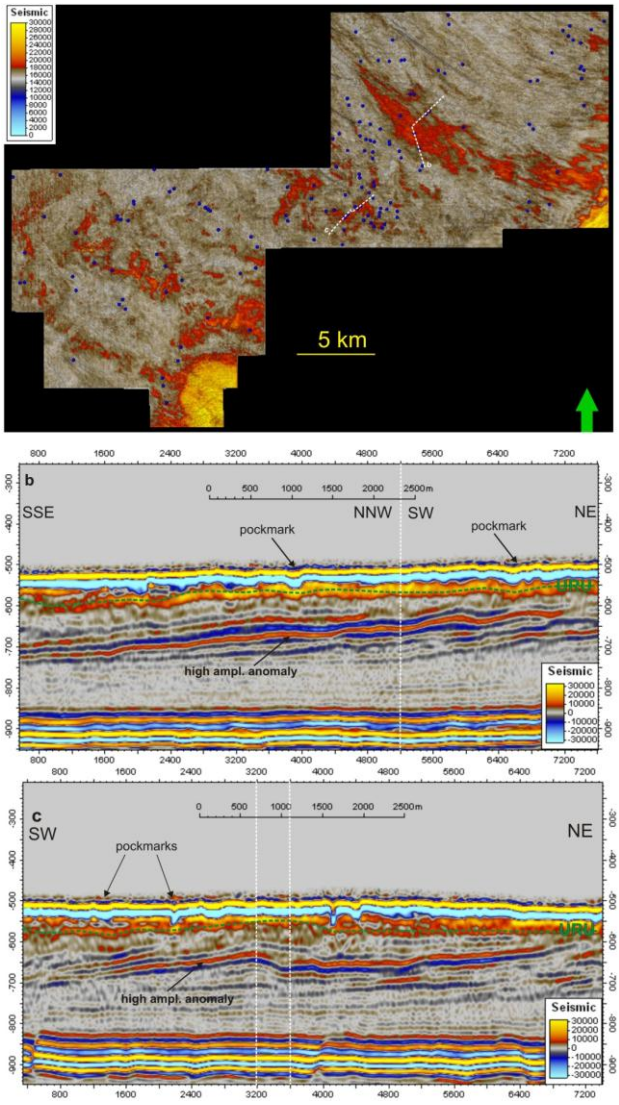

Fig.3-6. High amplitude anomalies; a. RMS volume attribute time slice extracted from the depths at 600-650 ms TWT, blue dots marks the location of the pockmarks,white lines show the position of the seismic profiles; b,c. seismic profiles shows amplitude anomalies beneath pockmarks.

4. CONCLUSIONS

Three 3D seismic data cubes (EL001, ST0309, and ST05M09) from the SW Barents Sea allowed mapping various seabed and subseabed depressions. Different mechanisms for the depression development were inferred from both seismic morphological and seismic anomaly observations. The mechanisms of depression formation vary within the study area. The study of ~ 400 depressions suggests three main formation mechanisms: 1. Iceberg and "dead-ice" creates depressions on site; 2. Subglacial melt water flow across obstacles creates a chain of depressions; 3. Seabed fluid flow release related to faults and/or shallow gas. The timing and the location of the formation of depressions depends on glacier driven processes in time and space.

The Veslemøy High area (EL0001) shows 22 circular and 32 near-circular depressions at the seafloor and bH reflector and 83 depressions at URU. The shallow features suggest gas blow-outs that were probably created during pressure release after the ice sheet retreat. The deeper features at URU are of various shape, depth and orientation that makes them difficult to classify. The depressions were divided into five groups according to distribution and fluid migration evidence within the seismic profiles. The features at the south of the paleo shelf and at the north-east of URU are associated with fluid migration. The source of the fluids is not obvious but fluids probably migrate from the source rocks along the faults in Tertiary sediments upward. The subsurface also shows depressions that concentrate in inside paleo iceberg scours.

The Nordkappbanken area (ST0309) shows also a large number of depressions on the seafloor. The depressions concentrate in a meandering channel and are probably caused by subglacial meltwater erosion. Only one shallow depression outside the channel could be interpreted as active pockmark as it is quite deep and not filled by sediments. Fluids probably migrate from source rocks through faults that come close to the seafloor where high amplitudes exists.

The Ingoydjupet area (ST05M09) shows a variety of depression sizes and possible origins. Some depressions connect to high seismic amplitudes in the shallow subsurface. Other depressions occur at the end of iceberg ploughmarks indicating potential dead ice

formations. In general depressions are more closely related to glacial seabed morphology. The ELoo01 and ST05M09 3D data show the best relationship between large scale glacial morphologies and depression distributions. It shows the complexity due to the fact that fluid migration and expulsion regulated by the type of sediment and thickness may create depressions but that depressions of similar shape and size may also be caused by glacier driven processes, which makes it sometimes difficult to infer their genesis with confidence.

Fluid sources are the sediment formations of Cretaceous age. ELoo01 seismic data show that the fluids could migrate from deeper sources to the Quaternary deposits. ST05M09 seismic data show high amplitude anomalies in the upper part of Tertiary sediment layers, which could be indicators of shallow gas accumulation feeding the seabed gas release system.

5. REFERENCES

Andreassen, K., 2009. Marine Geophysics. Lecture notes for GEO-3123 (compendium).

Andreassen, K., Hogstad, K., and Berteussen, K. A., 1990. Gas hydraters in the southern Barents Sea, indicated by a shallow seismic anomaly: First Break, v. 8, p.235-245.

Andreassen, K., Laberg, J.S. and Vorren, T.O., 2008. Seafloor geomorphology of the SW Barents Sea and its glaci-dynamic implications. Geomorphology, 97(1-2): 157-177.

Andreassen, K., Nilssen, E. and Ødegaard, C., 2007a. Analysis of shallow gas and fluid migration within the Plio-Pleistocene sedimentary succession of the SW Barents Sea continental margin using 3D seismic data. Geo-Marine Letters, 27(2): 155-171.

Andreassen, K., Ødegaard, C.M. and Rafaelsen, B., 2007b. Imprints of former ice streams imaged and interpreted using industry three-dimensional seismic data from the southwestern Barents Sea. Geological Society, London, Special Publications, 277: 151-169.

Aydin, A., 2000. Fractures, faults, and hydrocarbon entrapment, migration and flow. Marine and Petroleum Geology, 17: 797-814.

Bacon, M., Simm, R., Redshaw, T., 2003. 3-D seismic interpretations. Cambridge University press, pp. 17-26.

Bellec, V., Wilson, M., Boe, R., Rise, L., Thorsen, T., Buhl-Mortensen, L., Buhl-Mortensen, P., 2008. Bottom currents interpreted from iceberg ploughmarks revealed by multibeam data at Tromsøflaket, Barents Sea. Marine Geology, 249(3-4): 257-270.

Benn, D.I. and Evans D.J.A., 1998. Glaciers and Glaciation. 734 pp. Arnold.

Bjørlykke, K., 2006. Modelling of fluid flow and overpressure - A discussion. Norwegian Journal of Geology, 86: pp. 439-441.

Bukovics, C. and Ziegler, P.A., 1985. Tectonic development of the Mid-Norway continental margin. Marine and Petroleum Geology, 2(1): 2-22.

Butt, A. F., Drange, H., Elverhoi, A., Ottera, O. H., Solheim, A., 2002. Modeling Late Cenozoic isostatic elevation changes in the Barents Sea and their implications for oceanic and climatic regimes: preliminary results. Quaternary Science reviews 21(2002): 1643-1660.

Bøe, R., Rise, L. and Ottesen, D., 1997. Elongate depressions on the southern slope of the Norwegian Trench (Skagerrak): morphology and evolution Marine Geology, 146(1-4): 191-203.

Cartwright, J., Huuse, M. and Aplin, A., 2007. Seal bypass systems. AAPG Bulletin, 91(8): 1141-1166.

Chand, S., Mienert, J., Andreassen, K, Knies, J., Plassen, L., Fotland, B., 2008. Gas hydrate stability zone modelling in areas of salt tectonics and pockmarks of the Barents Sea suggests an active hydrocarbon venting system. Marine and Petroleum Geology, 25(7): 625-636.

Chand, S., Rise, L., Ottesen, D., Dolan M.F.J. , Bellec, V., Bøe, R., 2009. Pockmark-like depressions near the Goliat hydrocarbon field, Barents Sea: Morphology and genesis. Marine and Petroleum Geology, 26(7): 1035-1042.

Chopra, S. and Marfurt, K.J., 2005. 75 th Anniversary. Seismic attributes – A historical perspectives. Geophysics, 70(5), pp. 3SO-28SO.

Doré, A.G., 1995. Barents Sea Geology, Petroleum Resources and Commercial Potential. Arctic, 48(3): 207–221.

Eividin, T., Jansen, E., Riis, F., 1993. Chronology of Tertiary fan deposits off the Western Barents Sea: Implications for uplift and erosion history of the Barents Sea. Marine Geology, 112(1993): 109-131.

Elverhøi, A., Pfirman, S.L., Solheim, A., Larssen, B.B., 1989. Glaciomarine sedimentation in epicontinental seas exemplified by the northern Barents Sea. Marine Geology, 85 (1989) 225-250.

Faleide, J.I., Gudlaugsson, S.T. and Jacquart, G., 1984. Evolution of the western Barents Sea. Marine and Petroleum Geology, 1(May): 123-150.

Faleide, J.I., Solheim, A., Fiedler, A., Hjelstuen, B.O., Andersen, E.S., Vanneste, K., 1996. Late Cenozoic evolution of the western Barents Sea –Svalbard continental margin. Global and Planetary Change 12(1996): p. 53-74.

Forwick, M., Baetan, N.J., Vorren, T.O., 2009. Pockmarks in Spitsbergen fjords. Norwegian journal of Geology (89): p.65-76.

Judd, A., Hovland, M., 2007. Seabed Fluid Flow. Cambridge University Press.

Harrington, P.K., 1985. Formation of pockmarks by pore-water escape. Geo-Marine Letters (1985)5: 193-197.

Hart, J.K., 1997. The relationship between drumlins and other forms of subglacial glaciotectonic deformation. Quaternary Science Reviews, (16): pp. 93-107.

Heggland, R., 1997. Detection of gas migration from a deeper source by the use of exploration 3D seismic data. Marine Geology 137(1997):41-47.

Hovland, M., 1981. Characteristics of pockmarks in the Norwegian Trench. Marine Geology, 39: 103-117.

Hovland, M. and Judd, A. G., 1988. Seabed Pockmarks and Seepage: Impact on Geology, Biology and the Marine Environment. London, Graham and Trotman Ltd.

Hovland, M., Gardner, J.V. and Judd, A.G., 2002. The significance of pockmarks to understanding fluid flow processes and geohazards. Geofluids, 2(2): 127-136.

Hustoft, S., Buenz, S., Mienert, J., 2009a. Gas hydrate reservoir and active methane venting province in sediments <20 Ma young oceanic crust in the Fram Straight, offshore SW-Svalbard. Earth and Planetary Science Letters 284(2009) 12-24.

Hustoft, S., Dugan, B., Mienert, J., 2009b. Effect of rapid sedimentation on developing the Nyegga pockmark field: Constrains from hydrological modeling and 3-D seismic data, off-shore mid-Norway. Geochemistry Geophysics Geosystems, 2009, vol. 10, N6: 1525-2027.

Hustoft, S., Mienert, J., Bünz, S. and Nouzé, H., 2007. High-resolution 3D-seismic data indicate focussed fluid migration pathways above polygonal fault systems of the mid-Norwegian margin. Marine Geology, 245(1-4): 89-106.

Glassmann, J.R., Clark, R.A., Larter, S., Briedis, N.A., Lundegard, P.D., 1989. Diagenesis and hydrocarbon accumulation, Brent Sandstone (Jurassic), Bergen High Area, North Sea. The American Association of Petroleum Geologist Bulletin 73(11): p. 1341-1360.

Golynchik, P.O., 2008. Geological Structure of Cenozoic Sedimentary Basin in the Northwestern Margin of the Barents Sea Shelf. ISSN 0145_8752, Moscow University Geology Bulletin, 2009, Vol. 64, No. 5, pp. 318–323.

Koyi, H., Talbot, C.J., Tørudbakken, B.O., 1993. Salt diapirs of the southwest Nordkapp Basin: analogue modeling. Tectonophysics, 228(1993) 167-187.

Knutsen, S.-M. and Vorren, T.O., 1991. Early Cenozoic sedimentation in the Hammerfest Basin. Marine Geology, 101(1-4): 31-48.

Laberg, J.S. and Vorren, T.O., 1996. The middle and late Pleistocene evolution of the Bear Island Trough mouth fan. Global and Planetary Change, 12: 309-330.

Lambert, D.N., Kalcic, M.T., Faas, R.W., 2002. Variability in the seismic acoustic response of the shallow marine sediments determined by normal-incident 30-kHz and 50 kHz sound. Marine Geology, vol. 182, issue 1-2, p. 179-208.

Leeder, M., 1999. Sedimentology and Sedimentary Basin. From turbulence to Tectonic. Blackwell Publishing, pp.592.

Løseth, H., Gadin, M., and Wensaan, L., 2009. Hydrocarbone leakage interpreted on seismic data: Marine and Petroleum and Geology, v. 26, p. 1304-1319.

Mazzini, A., Svansen, H., Planke, S., Guliev, I., Akhmanov, G.G., Fallik., T., Banks, D., 2009. When mud volcano sleep: Insight from seep geochemistry at the Dashgil mud volcano, Azerbaijan. Marine and Petroleum Geology 26(2009) 1704-1715.

Mienert, J., Vanneste, M., Buenz, S., Andreassen, K.,Haflidason, H., and Sejrup,H.P., 2005. Ocean warming and gas hydrates stability on the mid-Norwegian margin at the Storrega Slide. Marine and petroleum Geology, v. 22, p. 233-244.

Nøttvedt, A., Berglund, T., Rasmussen, E., and Steel, R. 1988: Some aspects of Tertiary tectonics and sediments along the Western Barents Shelf. In: Early Tertiary Volcanism and the opening of the NE Atlantic in A. C. Morton and L. M. Parson (eds.) *Geological Society Special Publications* 39, 421-425.

Ottesen, D., Dowdeswell, J.A., Rise, L., 2005. Submarine landforms and the reconstruction of fast-flowing ice streams within a large Quaternary ice sheet: The 2500-km-long Norwegian-Svalbard margin (57°-80°N). Geological Society of America Bulletin, v. 117, no. 7/8, p. 1033-1050.

Pless, Gustav, master thesis, 2009. Occurrence of free gas and focused fluid flow system in the Veslemøy High area, Barents Sea. Tromsø, may 2009.

Posamentier, H.W., 2003. Depositional elements associated with a basin floor channel-levee system: case study from the Gulf of Mexico. Marine and Petroleum Geology 20(2003) 677-690.

Polteau, S., Mazzini, A., Galland, O., Planke, S., Malthe-Sørenssen, A., 2008. Saurce-shape intrusion: Occurence, emplacement and implication. Earth and Planetary Science Letters 266(2008): p. 195-204.

Ryseth, A. et al., 2003. Cenozoic stratigraphy and evolution of the Sorvestsnaget Basin, southwestern Barents Sea. Norsk Geologisk Tidsskrift, 83(2): 107-130.

Sharpe, D.R. and Shaw, J., 1989. Erosion of bedrock by subglacial meltwater, Cantley, Quebec. Geological Society of American Bulletin, v. 101, p. 1011-1020.

Schlumberger, 2000. Seismic Interpretations using Charisma. Training and exercise guide. GeoFrame 3.7. Houston.

Schlumberger, 2009. Seismic-to- Simulation Software manual: Interpreter Guide to Seismic Attributes, Houston.

Shepherd, G.R., 1989. Correlation of permeability and grain size. Ground water, vol. 27, N5: p. 633-638.

Suess, E., 2010. Transfer from the geosphere to biosphere. Marine cold seeps. In: K.N. Timmis (ed.), Handbook of hydrocarbon and lipid Microbiology, vol.1, part 3, p. 187-203, Springer Verlag, Berlin Heidelberg.

Svendsen, J.I., Alexanderson, H., Astakhov, V.I., Demidov, I., Dowdeswell, J.A., Funder, S., Gataullin, V., Henriksen, M., Hjort, C., Houmark-Nielsen, M., Hubberten, W., Ingolfsson, O., Jakobsson, M., Kjør, K.H., Larsen, E., Lokrantz, H., Lunkka, J.P., Lysså, A., J., M., Matiouchkov, A., Murray, A., Møller, P., Niessen, F., Nikolskaya, O., Polyak,

L., Saarnisto, M., Siegert, C., Siegert, M.J., Spielhagen, R.F., and Stein, R., 2004, Late Quaternary ice sheet history of northern Eurasia: Quaternary Science Reviews, v. 23, p. 1229-1271.

Vorren, T.O., Laberg, J.S., Blaume, F., Dowdeswell, J.A., Kenyon, N.H., Mienert, J., Rumohr, J., Werner, F., 1998. The Norwegian-Greenland Sea continental margins: morphology and Late Quaternary sedimentary processes and environment. Quaternary Science Reviews, 17(1-3): 273-302.

Winsborrow, M., Andreassen, K., Corner, G. D., Laberg, J.S., 2010. Deglaciation of the marine-based ice sheet: Late Weichselian paleo-ice dynamics and retreat in the southern Barents Sea reconstructed from onshore and offshore glacial geomorphology. Quaternary Science Review 29(2010) 424-442.

Woodworth-Lynas, C.M.T., Simms, A. and Rendell, C.M., 1985. Iceberg grounding and scouring on the Labrador Continental Shelf. Cold Regions Science and Technology, 10(2): 163-186.

Worsley, D., 2009. The post-Caledonian development of Svalbard and the Western Barents Sea. Polar Research 27, 2008: 298-317.

6. **APPENDIX**

Veslemøy High

Depressions at URU

N	x	y	Depth (ms)	Short axis (m)	Long axis (m)	Area (m^2)	orientation	Shape	Evidences of fluid migration
1.	413374,64	8005292,09	8,58	429,5	943,8	1272836,99	SE-NW	Elongated, composite	Bright spot, polarity change, pull-down effect, and faulting
2	415970,39	8004136,53	2,8	485,4	515,3	785397,59	SE-NW	Elliptic, composite	Amplitude increasing, pull-down, faulting
3.	417600,23	8003188,06	7,34	284,1	552,7	493049,30	NEE-SWW	Elongated, composite	faulting
4.	417882,43	8001819,01	11,4	260,09	441,78	360794,04	SE-NW	Elongated, composite	Bright spots, reflector discontinuity, faulting
5.	414166,06	8003593,14	4,0	98,95	136,89	42532,13	NE-SW	elongated	Reflector discontinuity
6.	413508,04	8003950,91	2,27	206,14	365,07	236302,36	SE-NW	elongated	faulting
7.	417047,33	8001135,16	6,0	93,61	238,9	70221,167	SE-NW	elongated	Bright spot
8.	416832,21	8000836,94	6,8	165,9	248,1	129241,74	NE-SW	elongated	Faults, repeats in the upper horizon
9.	412591,55	8002638,62	5,1	152,7	192,8	92443,36	E-W	elongated	Bright spot
10.	412480,54	8001918,15	2,9	109,28	193,6	66431,749	SE-NW	elongated	non
11.	412767,98	8000654,34	5,2	177,094	205,1	114051,01	E-W	circular	Reflector discontinuity, faults, repeats in the higher horizon
12.	412192,45	8001160,49	2,3	127,11	187,48	74828,03	SE-NW	elongated	Reflector discontinuity, faults
13.	411988,06	8001077,39	5,14	110,045	166,308	57466,28	SE-NW	elongated	Reflector discontinuity, faults
14.	417354,65	8001776,57	4,0	154,88	202,045	98259,17	SE-NW	elongated	Reflector discontinuity, polarity changing, acoustic masking, high amplitude anomalies
15.	415324,11	7999206,06	2,9	136,45	149,82	64190,83	E-W	circular	Reflector discontinuity, polarity changing, acoustic masking
16.	415088,01	7997482,75	3,0	121,3	128,012	48757,47	SE-NW	circular	Reflector discontinuity, polarity changing,

									acoustic masking, high amplitude anomalies
17.	415063,04	7997484,00	5,1	102,67	245,75	79225,82	SEE-NWW	Elongated, composite	Reflector discontinuity, acoustic masking, high amplitude anomalies
18.	414885,25	7997934,57	4,0	90,3	142,69	40458,61	NE-SW	circular	Reflector discontinuity, polarity changing, acoustic masking, high amplitude anomalies
19.	414903,43	7998801,37	4,0	97,7	140,35	43056,29	NNE-SSW	Elongated	Reflector discontinuity, acoustic masking, high amplitude anomalies
20.	414555,00	7998339,62	7,3	136,83	199,298	85627,63	SEE-NWW	Elongated	Bright spot, faulting
21.	414204,15	7997829.29	4,8	156,241	219,57	107720,33	NNE-SSW	Elongated	Bright spots
22.	414018,72	7998628,88	4,8	128,9	251,9	101955,52	NNE-SWW	Elongated, composite	Reflector discontinuity, faults
23.	413295,46	7997175,77	4,0	135,76	233,7	99623,13	SE-NW	Elongated	Reflector discontinuity, faults, polarity changing, high amplitude anomalies
24.	413178,01	7997330,38	5,9	79,99	93,2	23408,91	SE-NW	Elongated	Reflector discontinuity, amplitude increasing, high amplitude anomalies
25.	414114,23	7999038,47	1,8	64,58	129,1	26179,05	SE-NW	Elongated	non
26.	414274,96	7999751,97	1,85	147,14	150,5	69533,95	SEE-NWW	circular	Faults, bright spot in deeper layers
27.	413329,58	7999366,54	5,05	267,49	647,35	543721,31	SSE-NNW	Elongated, composite	Acoustic pipe, reflector thinning
28.	414844,33	7995105,03	6,6	104,96	180,52	59494,77	SE-NW	Elongated	High amplitude anomalies, faults
29.	413675,85	7995767,87	8,8	136,16	206,92	88467,07	NNE-SSW	Elongated	Polarity changing, high amplitude anomalies
30.	412525,57	7996293,54	3,2	153,92	242,4	117154,05	N-S	Elongated	High amplitude anomalies
31.	411004,74	7996416,05	3,2	253,9	257,28	205115,45	SE-NW	Circular	Polarity changing, reflector discontinuity, amplitude

									anomalies
32.	410112,95	7999114,28	5,0	108,59	110,46	37663,83	SE-NW	circular	Reflector discontinuity, repeats in the higher horizon
33.	409815,86	7999180,16	7,3	178,67	220,36	123627,20	SE-NW	circular	Reflector discontinuity, acoustic pipe
34.	407590,96	7999740,81	6,4	222,051	379,16	264365,57	SE-NW	elliptical	Reflector thinning, acoustic pipe, continuation towards the higher horizon
35.	406709,40	8000133,57	5,9	211,93	307,62	204708,87	SE-NW	elliptical	Reflector discontinuity, amplitude increasing, bright spots, faults, continuation towards the higher horizons
36.	406848,90	7999417,10	3,28	197,7	242,38	150464,17	N-S	elliptical	Bright spot, reflector thinning, continuation towards the upper horizon
37.	406713,84	7998716,37	2,26	145,06	147,9	67366,73	N-S	circular	Acoustic pipe, faults, bright spots, continuation towards the upper horizon
38.	406302,69	7999004,99	3,19	123,55	135,69	52640,53	SE-NW	circular	Bright spots, continuation towards the upper horizon
39.	405992,5	7992782,5	5,13	337,16	669,15	708417,33	SE-NW	elongated	Reflector discontinuity, continuation towards the upper horizon, acoustic pipe
40.	410809,94	7992508,29	12,03	102,08	137,58	44098,68	SE-NW	elongated	Amplitude rising, reflector discontinuity, acoustic pipe
41.	410408,01	7992981,8	10,31	132,73	169,53	70655,39	NE-SW	elliptic	Amplitude rising, bright spot, reflector discontinuity
42.	407873,05	7995858,9	10,89	247,54	305,78	237675,33	SEE-NWW	elongated	Reflector discontinuity, bright spot, acoustic pipe
43.	405942,05	8000306,74	4,59	59,26	98,98	18417,84	N-W	elliptic	Acoustic pipe towards the upper reflector, bright spots
44.	405013,23	7999751,58	3,99	130,64	148,76	61022,78	NE-SW	circular	Acoustic pipe towards the

									upper reflector, bright spot
45.	404174,59	8000000,93	3,41	140,1	294,21	129427,1	SE-NW	elongated	Acoustic pipe towards the upper reflector, bright spot
46.	407846,33	8003859,53	8,04	222,765	395,95	276959,94	SE-NW	elongated	non
47.	403356,75	8004684,79	6,27	136,44	280,88	120335,06	SE-NW	elongated	Amplitude rising, polarity changing
48.	403038,76	8004833,76	5,69	278,18	324,5	283445,95	SE-NW	elongated	Amplitude rising
49.	404937,13	8006761,28	2,86	91,55	127,7	36709,53	NE-SW	circular	Amplitude rising
50.	402900,82	8008092,32	2,31	148,586	270,77	126330,46	SE-NW	elongated	Amplitude rising, acoustic pipe
51	402121,53	8008528,20	4,58	327,1	366,3	376224,53	SE-NW	elliptic	Acoustic pipe, amplitude rising, bright spot
52.	400255,61	8009259,96	5,17	181,08	290,9	165403,18	NE-SW	elongated	Bright spot, acoustic pipe
53.	400141,74	8009988,51	6,54	128,0	198,56	79805,23	NE-SW	elongated	Amplitude anomaly, acoustic pipe
54.	404948,17	8009493,58	1,14	116,02	130,12	47403,08	NEE-SWW	elliptic	Amplitude rising, polarity changing, acoustic pipe
55.	402366,75	8008425,91	9,72	193,43	222,272	135001,39	SE-NW	Elliptic (mound)	Amplitude rising, polarity changing, acoustic pipe
56.	401864,69	8011410,01	6,86	106,54	177,05	59229,53	N-S	Elliptic (mound)	Acoustic pipe
57.	402143,79	8011485,4	3,41	69,08	109,6	23773,47	NE-SW	Elongated	Bright spot
58.	400797,16	8013093,78	3,4 2	89,07	169,27	47341,4	NEE-SWW	Elongated	Bright spot
59.	403679,9	8010665,25	2,82	90,9	124,73	35601,18	SE-NW	Elongated	Amplitude anomaly, polarity changing, acoustic pipe
60.	403709,21	8010248,99	5,13	121,8	401,35	153497,11	NNE-SSW	Elongated	Polarity changing, bright spot, acoustic pipe
61.	405707,42	8010664,41	6,86	165,98	306,1	159532,34	SE-NW	Elongated	Polarity changing, bright spot, reflector discontinuity, acoustic pipe
62.	406496,31	8011425,47	3,45	329,65	348,97	361219,2	SE-NW	Circular	non
63.	415209,25	8010460,00	2,86	110,997	280,99	97933,61	NE-SW	Elongated	Mounded, clear rim
64.	414898,18	8007232,6	4,0	140,66	224,056	98959,35	SE-NW	Elongated	Amplitude rising, reflector thinning, mounded
65.	415210,31	8007468,28	2,27	124,6	212,7	83217,6	N-S	Elongated	Amplitude rising
66.	413863,63	8010080,00	8,03	107,7	151,9	51369,24	NE-SW	Elongated	Amplitude

									rising, bright spot
67.	413671,42	8010241,32	0,59	138,19	290,73	126152,57	NE-SW	Elongated (merged)	Clear acoustic pipe, bright spot
68.	413757,34	8010458,51	2,86	84,7	135,65	36077,20	NE-SW	Elongated	Acoustic pipe, bright spot
69.	413458,2	8010483,32	4,0	93,36	118,6	34767,64	NE-SW	Elongated	Amplitude anomaly
70.	413153,48	8010396,27	3,45	162,99	220,78	112992,69	NE-SW	Elongated	Amplitude anomaly
71.	412277,581	8010407,58	6,31	196,49	260,95	161000,56	NE-SW	Elongated	Reflector discontinuity, bright spot, amplitude anomaly acoustic pipe
72.	411436,65	8009097,46	10,86	203,89	334,16	213934,11	NE-SW	Elongated	Reflector discontinuity, acoustic pipe, continuation to the upper horizon, bright spots
73.	412569,08	8009720,12	2,27	308,9	320,77	311129,58	NE-SW	Circular	Amplitude anomaly, bright spot, acoustic pipe
74.	410227,53	8009447,11	8,0	192,76	278,24	168409,32	NE-SW	Elongated	Amplitude anomaly, bright spots, acoustic pipe
75.	411868,65	8012239,92	4,58	115,1	216,34	78188,30	NE-SW	Elongated	Amplitude anomaly, acoustic pipe, bright spots
76.	412145,85	8012779,24	5,69	128,97	176,9	71638,45	NE-SW	Elongated	Amplitude anomaly, acoustic pipe, bright spot
77.	412032,87	8012019,21	2,27	61,16	85,4	16400,42	NNE-SWW	Elongated	Amplitude anomaly, acoustic pipe

APPENDIX 2

Depressions at the bH horizon

N	x	y	Depth (ms)	Short axis (m)	Long axis (m)	Area (m^2)	orientation	Shape	Evidences of fluid migration
1.	381539,37	7996855,29	7,7	832,992	872,035		E-W	circular	Acoustic masking, seafloor expression
2.	387256,43	7999563,61	2	611,748	1280,53		E-W	elongated	High amplitude anomalies on bF
3.	309607,96	8007543,46	4,7	802,89	824,351		E-W	circular	High amplitude anomalies on bF
4.	391717,94	8000685,87	2,07	722,639	841,29		E-W	circular	High amplitude on bH and bF
5.	392370,37	8002224,39	2,18	816,047	944,276		E-W	circular	High amplitude anomalies on bF
6.	394890,35	7998544,73	6,6	642,268	692,478		E-W	circular	High amplitude anomalies on R1
7.	396127,32	7999255,79	3,64	313,578	620,197		E-W	elongated	High amplitude anomalies on R1, reflector discontinuity of bF
8.	396891,98	8000603,5	3,0	480,158	540,983		S-N	elongated	High amplitude anomalies on bH
9.	398331,39	8003209,99	0,73	565,248	646,8		E-W	elongated	High amplitude anomalies on bF
10.	383483,96	8004793,73	3,66	615,791	868,42		E-W	elongated	none
11.	386271,04	8005907,79	1,83	856,812	893,385		NE-SW	circular	none
12.	386979,62	8004852,16	2,56	590,326	1021,13		S-N	elongated	High amplitude anomalies on R1, acoustic pipe
13.	387676,18	8005975,33	2,2	651,44	780,737		E-W	elongated	Pull-down
14.	388531,2	8006556,64	2,56	810,937	832,745		E-W	circular	none
15.	390501,63	8005410,52	2,19	628,435	724,781		E-W	elongated	none
16.	396315,73	8007554,76	3,5	1027,87	1184,78		E-W	circular	none
17.	400617,73	8011502,79	1,2	1021,6	1396,66		E-W	circular	High amplitude anomaly on URU
18.	402709,7	8011288,44	3,8	937,36	1270,92		E-W	elongated	High amplitude anomaly on URU
19.	403968,91	8012490,52	2,91	636,151	747,221		E-W	circular	none
20.	410957,29	8012034,95	1,76	771,53	1052,15		E-W	elongated	Reflector discontinuity, high amplitude anomaly on URU
21.	412604,64	8006853,74	2,18	411,15	666,44		S-N	elongated	High amplitude anomaly on URU, pull-down (URU)
22.	410676,01	8007396,64	3,64	711,595	824,36		E-W	elongated	High amplitude anomaly on URU
23.	410552,73	8006430,08	3,5	493,36	590,5		E-W	elongated	High amplitude

									anomaly on URU
24.	405978,37	8004500,32	2,9	632,58	750,25		S-N	elongated	High amplitude anomaly on URU, pull-up (URU)
25.	404587,36	8005268,39	2,21	693,44	962,713		S-N	elongated	High amplitude anomaly on URU
26.	402837,51	8001800,77	4,04	562,327	597,987		S-N	elongated	High amplitude anomaly on URU
27.	403789,04	7999296,78	6,6	645,06	686,73		NE-SW	circular	High amplitude anomaly on bH, acoustic pipe
28.	407841,89	7996238,23	3,66	565,48	722,9		E-W	circular	none
29.	407841,93	7996239,03	3,67	760,4	801,16		E-W	circular	none
30.	409924,65	7997345,49	4,77	530,78	815,87		E-W	elongated	none
31.	411155,38	7996062,85	1,85	324,39	572,23		S-N	elongated	Acoustic pipe

APPENDIX 3

Depressions at the seafloor

N	x	y	Depth (ms)	Short axis (m)	Long axis (m)	orientation	Shape	Evidences of fluid migration
1.	381587,89	7996824,33	15,1	895,6	912,4	E-W	circular	Acoustic masking, corresponds to crater on bH
2.	379690,62	7998433,73	6,8	551,35	913,6	E-W	elongated	none
3.	376720,06	7998598,34	3,1	539,9	639,1	E-W	elongated	none
4.	384380,32	8009154,99	11,4	295,45	415,95	SE-NW	elongated	none
5.	385279,68	8010123,58	3,64	584,5	957,16	E-W	elongated	none
6.	388462,28	8005454,07	6,4	417,9	551,6	SE-NW	elongated	none
7.	390220,59	8000274,83	3,69	600,13	914,39	SE-NW	elongated	Crater on bH
8.	393204,23	8002990,00	4,11	687,5	1216,12	NE-SW	elongated	Crater on bH
9.	392426,53	8002346,85	3,2	534,54	998,51	NE-SW	elongated	Crater on bH
10.	392250,71	8000326,22	1,82	366,6	664	NE-SW	elongated	none
11.	388755,53	7998503,08	3,2	287,6	399,07	E-W	elongated	none
12.	384587,31	7998242,94	6,44	290,9	637,19	E-W	elongated	none
13.	414874,83	8006262,06	7,6	333,23	492,06	S-N	elongated	Crater on bH
14.	414083,52	8006476,7	5,2	343,47	543,67	E-W	elongated	Crater on bH
15.	412638,26	8006588,54	4,04	479,9	522,34	NE-SW	elongated	Crater on bH
16.	414085,05	8006487,26	7,02	294,6	384,02	S-N	circular	none
17.	411909,75	8008545,14	7,33	254,9	438,29	E-W	elongated	High ampl. anomaly
18.	411743,27	8008720,42	6,5	265,28	437,58	E-W	elongated	High ampl. anomaly
19.	411010,84	8008568,95	5,87	259,59	560,224	NE-SW	elongated	High ampl. anomaly
20.	409291,77	8008752,52	5,87	391,17	520,16	E-W	circular	High ampl. anomaly URU
21.	408285,93	8008158,71	3,6	489,3	987,6	NE-SW	elongated	High ampl. anomaly URU
22.	400898,32	8012688,92	7,68	442,14	800,29	E-W	circular	Crater on bH